



Decadal variability of
El Niño / Southern Oscillation
in the GFDL-ESM2M
pre-industrial control simulation

Master Thesis written by
Goratz Beobide Arsuaga

Supervised and examined by
Prof. Dr. Mojib Latif
Dr. Tobias Bayr

MATHEMATISCH - NATURWISSENSCHAFTLICHE FAKULTÄT DER
CHRISTIAN-ALBRECHTS-UNIVERSITÄT ZU KIEL
GEOMAR HELMHOLTZ - ZENTRUM FÜR OZEANFORSCHUNG KIEL
- MARITIME METEOROLOGIE -

Kiel, October 2019

Contents

Abstract	III
Zusammenfassung	IV
Abbreviations	VI
1 Introduction	1
1.1 Overview and motivation	1
1.2 Tropical Pacific mean state	3
1.3 El Niño / Southern Oscillation (ENSO)	4
1.3.1 ENSO domains	6
1.3.2 ENSO metrics	7
1.3.3 Atmospheric feedbacks	8
2 Data and Methodology	10
2.1 Data	10
2.1.1 GFDL-ESM2M	10
2.1.2 ERA-20C	12
2.2 Methodology	13
2.2.1 Model mean state bias	13
2.2.2 ENSO definition	13
2.2.3 ENSO metrics	14
2.2.4 Atmospheric feedbacks	15
2.2.5 Decadal ENSO amplitude modulation	16
3 Results	18
3.1 ENSO simulation skills	18
3.1.1 Model bias in the mean state	18
3.1.2 ENSO metrics	20
3.1.3 Atmospheric feedbacks	24
3.2 Decadal ENSO amplitude	27
3.3 High / Low ENSO amplitude periods	33
3.3.1 Tropical Pacific mean state	33
3.3.2 Tropical Pacific variability	36
3.3.3 ENSO metrics	38
3.3.4 Atmospheric feedbacks	42
3.4 Decadal ENSO amplitude modulation	44

4 Summary, Discussion and Conclusion	51
4.1 Summary	51
4.2 Discussion	53
4.3 Conclusion	56
List of figures	58
Bibliography	63
Acknowledgement	70
Declaration of candidate	71

Abstract

The decadal variability of El Niño / Southern Oscillation (ENSO) is investigated in the pre-industrial control run of the GFDL-ESM2M fully coupled climate model. Overall, the climate model has quite a realistic representation of relevant ENSO properties: the probability distribution of Niño3.4 sea surface temperature (SST) anomalies is positively skewed, the highest equatorial Pacific SST variability is observed in boreal winter with the corresponding decrease in variability during spring, and the decadal climate variability shows a shift of the ENSO spatial pattern. Nevertheless, compared to the ERA-20C reanalysis product, the model shows problems most climate models have: the anomalous cold equatorial Pacific SST with the largest bias located on the eastern side, strong easterly winds over the western equatorial region, the rising branch of the Walker Circulation located too far west and the too strong subsidence regime east of the date line.

Two main periods of about 60 years with high and low ENSO amplitudes are observed, ranging between 1.5°C and 0.7°C . Here it is shown, that the High and Low epochs have remarkably different mean states, which can explain the differences in simulated ENSO amplitudes. The High epoch is characterized by a weaker zonal equatorial SST gradient and a warmer Niño3 SST. The less intense Walker Circulation reduces the subsidence branch, and the negative shortwave (SW) feedback during El Niño events is extended over the Niño3 domain. The stronger convective response over the eastern equatorial Pacific enhances the SST variability, increasing considerably during boreal winter, and the strong non-linearities in atmospheric feedbacks are kicked forming strong East Pacific-like (EP) El Niño events. Hence, the ENSO asymmetry is remarkably incremented.

During the Low epoch, the zonal equatorial SST gradient is increased with cooler Niño3 SST. The Walker Circulation is intensified and the subsidence branch over the Niño3 region is strengthened. The Niño3 domain also coincides with the reduction of the negative SW feedback during El Niño events, as well as the incapability of the atmospheric regime to turn into a convective state, when SST anomalies are turned positive. In addition, the Niño3.4 SST variability and the wind feedback are considerably decreased during boreal winter. There are indications that the reduced SST variability of the Low epoch is caused by the too strong subsidence branch over the Niño3 region, which restricts the seasonal southward migration of the Intertropical Convergence Zone (ITCZ), and hampers the evolution of strong EP El Niño events. However, the convective response is maintained over the western equatorial Pacific, outside of the strongest mean subsidence region, as shown by the highest negative SW feedback. Therefore, during this time period the frequency of Central Pacific-like (CP) El Niño events is increased, shifting the ENSO spatial pattern, and reducing SST variability in lack of strong EP El Niños. Correspondingly, the non-linearities between the positive and negative phases of ENSO are reduced, diminishing the ENSO asymmetry. In summary, these results show how important the mean state is for the ENSO amplitude and asymmetry.

Zusammenfassung

In dieser Arbeit wurde die dekadische Variabilität von „El Niño / Southern Oscillation“ (ENSO) mithilfe eines vorindustriellen Kontrolllaufs des gekoppelten GFDL-ESM2M Klimamodells untersucht. Insgesamt simuliert das Klimamodell die relevanten ENSO-Eigenschaften realistisch: die Meeresoberflächentemperatur (SST) in der Niño3.4-Region hat eine positive Skewness, die maximale SST-Variabilität des äquatorialen Pazifiks ist während des borealen Winters, das Minimums im Frühling, und in der dekadischen Klimavariabilität zeigt es eine Verlagerung des räumlichen ENSO-Musters zwischen östlichem und zentralem äquatorialen Pazifik. Nichtsdestotrotz weist das Modell im Vergleich zur ERA-20C Reanalyse Probleme auf, die viele Klimamodelle haben: ungewöhnlich kalte SSTs im östlichen äquatorialen Pazifik, zu starke Ostwinde über der westlichen Äquatorregion, ein zu weit im Westen liegender aufsteigender Ast der Walker Zirkulation, und ein zu starker, absinkender Ast im östlichen Pazifik.

Es wurden zwei Zeiträume von jeweils 60 Jahren mit hoher und niedriger ENSO-Amplituden identifiziert, die ungefähr bei 1.5C und 0.7C liegen. Die Epochen hoher und niedriger ENSO-Amplitud weisen bemerkenswerte Unterschiede im mittleren Zustand auf, die erklären können, warum die ENSO-Amplitud so unterschiedlich simuliert wird. Die Epoche hoher ENSO-Amplitude ist durch einen verringerten zonalen SST-Gradienten entlang des Äquators und wärmere SSTs in der Niño3-Region charakterisiert. Die Walker-Zirkulation ist schwächer, wodurch vor allem der absinkende Ast schwächer ist und das Feedback der kurzwelligen Einstrahlung sich auf die Niño3-Region ausweitet. Die stärkere Konvektion über dem äquatorialen Pazifik im Osten verstärkt die SST Variabilität, insbesondere während des borealen Winters, und die atmosphärischen Feedbacks weisen stark Nichtlinearitäten auf, sodass sich starke „East Pacific“ (EP) El Niño-Ereignisse ausbilden. Entsprechend ist die Asymmetrie zwischen den ENSO Phasen deutlich verstärkt.

Während der Epoche niedriger ENSO-Amplitude dagegen ist der zonale SST-Gradient entlang des Äquators verstärkt und weist eine kältere SST in der Niño3-Region auf. Die Atmosphäre reagiert darauf mit einer Intensivierung der Walker-Zirkulation, insbesondere des absinkenden Astes über der Niño3-Region. In dieser Region ist während El Niño-Ereignissen das negativ kurzwellige Strahlungsfeedback schwächer, und die vertikalen Wind in 500 hPa Höhe reagieren schwächer auf SST-Anomalien, Dies hat zur Folge, dass die Atmosphäre keinen konvektiven Zustand erreichen kann, wenn SST-Anomalien positiv werden. Hinzu kommt, dass die Variabilität der SSTs in der Niño3.4-Region sowie das Windfeedback während des borealen Winters deutlich verringert sind. Es gibt Anhaltspunkte, dass die reduzierte Variabilität der SST während der Epoche niedriger ENSO-Amplitude durch einen übermäßig starken sinkenden Zweig der Walker-Zirkulation über der Niño3-Region verursacht wird, wodurch die saisonale südwärtige Migration der Innertropischen Konvergenzzone eingeschränkt wird, was wiederum die Ausbildung starker EP El Niño-Ereignisse behindert. Nichtsdestotrotz wird ein konvektiver Zustand der Atmosphäre über dem äquatorialen Pazifik im Westen außerhalb der Region mit der

stärksten Luftmassenabsenkung erreicht, erkennbar am stärksten kurzwelligen Strahlungsfeedback. Aus diesem Grund kommen während der Epoche niedriger ENSO-Amplitude „Central-Pacific“ (CP) EL Niño-Ereignisse wesentlich häufiger vor, was das ENSO-Muster in den zentralen Pazifik verschiebt und die höchste Variabilität der SST aus Mangel an starken EP El Niño-Ereignissen verringert. Damit zusammenhängend sind die Nichtlinearität zwischen der positiven und der negativen ENSO-Phase reduziert, sodass die Asymmetrie von ENSO gering ist. Zusammenfassend zeigen diese Ergebnisse, wie wichtig der mittlere Zustand für ENSO-Amplitude und ENSO-Asymmetrie ist.

Abbreviations

SST(A)	Sea Surface Temperature (Anomaly)
T	Ocean Subsurface Temperature
U10(A)	Surface Zonal Wind (Anomaly)
W500(A)	Vertical Winds at 500 hPa height (Anomaly)
NHFS(A)	Net Heat Flux (Anomaly)
LHFS(A)	Latent Heat Flux (Anomaly)
SW(A)	Shortwave (Anomaly)
CLT	Total Cloud Cover
PR	Precipitation

ENSO	El Niño / Southern Oscillation
EP	East Pacific
CP	Central Pacific
TNI	Trans-Niño Index
PDF	Probability Density Function
ITCZ	Intertropical Convergence Zone
CMIP5	Coupled Model Intercomparison Project Phase 5
GCM	General Circulation Model
ESM	Earth System Model

Chapter 1

Introduction

1.1 Overview and motivation

It is an obvious fact that our human civilization depends on the climate conditions. Although the societal, technological and economical systems have strongly developed in some countries, insulating against the impacts of climate variability, many other developing and underdeveloped countries face serious vulnerabilities related to a changing climate (*Handmer et al.*, 1999). In fact, while temperate countries have converged towards high levels of income assisted by their climate, tropical countries income per capita is scaled in much lower values (*Masters and McMillan*, 2001). The incapability of underdeveloped countries to mitigate climate hazards could result in large scale migrations and consequent violent conflicts, affecting the apparently safe developed countries (*Reuveny*, 2007). Hence, the study of climate variability should be highly demanded by both the apparently insulated and vulnerable societies.

In order to understand and predict global climate variations, the tropical Pacific region plays a key role (*Wittenberg et al.*, 2006). Because of its large geographical extension and heavy precipitation, the variability of the tropical Pacific climate directly and indirectly affects the weather, ecosystems, agriculture and human population worldwide (*Diaz and Markgraf*, 2000; *Hsu and Moura*, 2001; *Wittenberg et al.*, 2006). As a solid example, the El Niño / Southern Oscillation (ENSO) is considered to be the most dominant interannual climate fluctuation.

ENSO can generally be addressed by cold (La Niña) and warm (El Niño) events, which affect the eastern-central equatorial Pacific sea surface temperatures (SST) with negative and positive anomalies respectively (*Philander*, 1985). The ENSO phenomenon contains an irregular periodicity ranging from 2 to 7 years, restricting the highest SST variability to the boreal winter (*Rasmusson and Carpenter*, 1982; *Bellenger et al.*, 2014). Its effects are felt globally via atmospheric teleconnections (*Trenberth et al.*, 1998; *Alexander et al.*, 2002). The 1997-98 El Niño event in particular caused billions of dollars in damages and thousand of lives to be lost (*Kerr*, 1999; *McPhaden*, 1999).

ENSO has suffered interdecadal modulations in the past, varying its behavior including the frequency, amplitude and spatial pattern (*Fedorov and Philander*, 2000; *Yeh and Kirtman*, 2005; *Sun and Yu*, 2009; *McPhaden et al.*, 2011). In fact, captured by the paleorecords we know that the positive and negative phases of ENSO have been excited for at least the last 10^5 years

and its variability is believed to have changed considerably during the Holocene (*Cole, 2001; Tudhope et al., 2001; Koutavas et al., 2006; Cobb et al., 2013; McGregor et al., 2013*). Similarly, in the recent past we have been able to observe a decadal shift of the ENSO characteristics. For instance, a interdecadal shift of the late 1970s lengthened the ENSO period from 2-4 years to 4-6 years when comparing the time periods 1962-1975 and 1980-1993 (*An and Wang, 2000*).

Nevertheless, due to the short observational records of tropical Pacific climate variability, long unforced simulations of coupled General Circulation Models (GCM) are necessary in order to investigate the natural variability of ENSO on decadal and longer timescales (*Wittenberg, 2009; Russon et al., 2014*). For instance, the GFDL CM2.1 pre-industrial control run has gained the attention of many authors, showing large unforced multi-decadal ENSO variability changes (*Wittenberg, 2009; Kug et al., 2010; Wittenberg, 2015*). The main downside of the dependence on coupled GCMs is that ENSO representation suffers from biases in the mean state as well as in the ENSO dynamics.

Although coupled GCMs have improved some of the ENSO characteristics from the CMIP3 to the CMIP5 multi-model ensemble reducing by a factor of two the diversity of the ENSO amplitude, the wind (U10) feedback and shortwave (SW) feedback are generally underestimated (*Bellenger et al., 2014*). Hence, the apparent improvements of the ENSO amplitude result from the error compensation of ENSO atmospheric feedbacks (*Bayr et al., 2018*). In addition, the main source of unrealistic atmospheric feedbacks and hence the ENSO representation has been attributed to the tropical Pacific mean state biases (*Dommenget et al., 2014*), which we must take into consideration.

The background tropical Pacific mean state and ENSO characteristic are in fact closely linked, also in decadal timescales. Whether the changes in the background climatology affect the decadal variability of ENSO or the changes in ENSO characteristics affect the mean state continues to be controversial. Studies using model experiments have proved that the ENSO amplitude is sensitive to the mean thermocline depth (*Zebiak and Cane, 1987; Latif et al., 1993*), to the thermocline tilt (*Hu et al., 2013*), and to the mean zonal SST gradient (*Knutson et al., 1997*). On the other hand, the interdecadal shift of the ENSO asymmetry and spatial pattern can lead to the modification of the climatological state of the tropical Pacific as a residual of the ENSO cycle (*Ogata et al., 2013*). Furthermore, the non-linearities of atmospheric feedbacks are believed to play a central role in mean state changes and the decadal ENSO amplitude modulation (*Atwood et al., 2017; Chen et al., 2017*).

The present study investigates the natural decadal variability of the main ENSO characteristics using a 500 year pre-industrial control run from the fully coupled GFDL-ESM2M climate model. After exploring the mean state and ENSO biases, the focus is set on the relation between the decadal shift of the ENSO statistics and the background climatology. In addition, special attention has been given to the non-linear behavior of the atmospheric feedbacks during epochs of high and low ENSO amplitudes.

Throughout this work we would like to address the following questions: How well does the model simulate ENSO events? Is there any decadal ENSO variability in the unforced control run? And if so, what is its relationship to the background mean state?

In the subsequent sections one can read the description of the tropical Pacific mean state and ENSO. Chapter 2 contains the data and methodology used to obtain the results shown in Chapter 3. Finally, the summary, discussion and main findings are concluded in Chapter 4.

1.2 Tropical Pacific mean state

The atmospheric circulation is generally forced by the incoming solar radiation and reshaped by the Earth's rotation. The difference in latitude of the incoming solar radiation is compensated by a set of different circulation cells. In the tropics, the zonally averaged meridional circulation between 30°N - 30°S is called the Hadley Cell (*Quan et al.*, 2004). The Hadley Cell has a pair of cellular patterns ascending near the equator and descending over the subtropical area, which produces a poleward mass transport in the upper troposphere and equatorward in the lower troposphere (*Bjerknes*, 1966). Due to the Earth's rotation, and hence the coriolis effect, the equatorward flow is redirected west forming the easterlies, or more commonly named, the trade winds (*National Oceanic and Atmospheric Administration*, 2018).

Since the tropical currents respond to the wind system (*Wyrski*, 1974), the equatorial easterly winds advect the tropical Pacific Ocean's surface westward, piling up the waters on the western equatorial section and causing a thermocline tilt and a zonal SST gradient (*Philander*, 1981). The result leads to a characterization of the western Pacific equatorial region by a warm pool (i.e. the Western Pacific Warm Pool), whose eastward advection is restricted by the trade winds, and a deep thermocline. On the other hand, the eastern side, enhanced by a shallow thermocline and an upwelling systems forced by the Ekman upwelling, contains relatively cold waters forming a cold tongue (*Jin*, 1996). Therefore, although the equatorial incoming solar radiation is zonally uniform, the ocean-atmospheric processes lead to a product which is zonally asymmetric (Figure 1.1).

The zonal asymmetry of the equatorial Pacific is directly related to the second cell, generally known as the Walker Circulation (Figure 1.1). Similarly to the Hadley Cell it is a thermally direct circulation, constituted by rising motion over the warm western Pacific and sinking over the cold waters of the eastern Pacific. Its zonal flow is described by the westerly winds in the upper troposphere and the low level winds blowing from the east as part of the trade winds (*Bjerknes*, 1969). The prevailing subsidence over the eastern equatorial Pacific limits the formation of deep clouds and precipitation. Therefore, the mentioned area is observed as a highly stable, high pressure zone. In contrast, unstable atmospheric conditions with deep convective clouds and heavy precipitation are the main characteristics of the western low pressure region (*Lau K.; Yang S.*, 2002).

The collision of the trade winds produces the Intertropical Convergence Zone (ITCZ), a narrow band of rising air and intense precipitation. The source of precipitation is the moisture convergence brought on by the northern and southern hemisphere trade winds towards the equator (*Byrne et al.*, 2018). As a first-order approximation, its annual mean positioning follows the warm SST and we could highlight three main regions: a few degrees north of the equator and hence north of the equatorial cold tongue at the central-eastern Pacific, over the western Pacific warm pool, and over the south western Pacific region, mainly known as South Pacific Convergence Zone (*Yu and Zhang*, 2018).

Nevertheless, the positioning of the ITCZ is not constant during the year. It follows the seasonal solar cycle, displacing its position south during boreal winter and north during boreal summer (*Byrne et al.*, 2018). Related to the southward displacement of the ITCZ, the equatorial easterly winds are relaxed and the eastern equatorial Pacific SST are incremented during boreal winter (*Kessler et al.*, 1998).

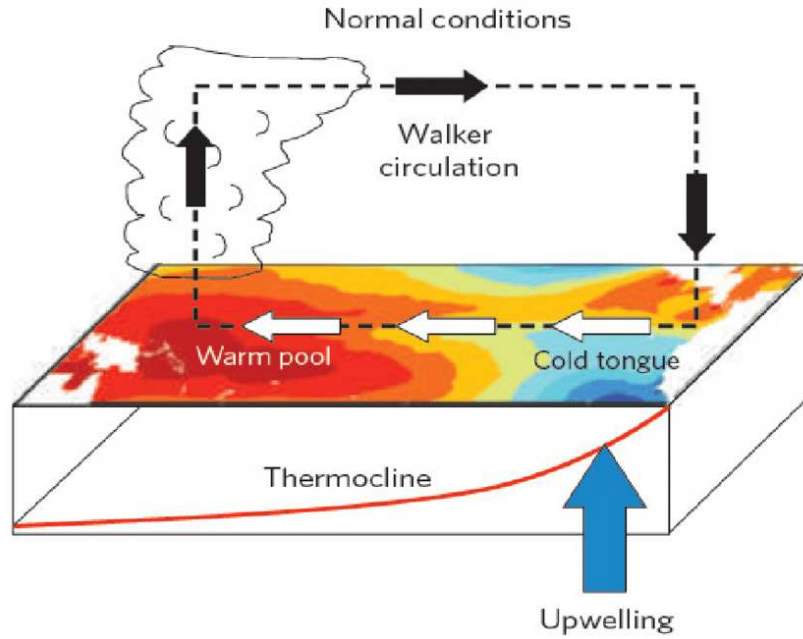


Figure 1.1: Schematic representation of the tropical Pacific's oceanic and atmospheric mean states. Red and blue shading correspond to warm and cold SSTs, respectively. The Walker Circulation is represented by the black dashed line, the direction pointed out by the black arrows. The white arrows show the equatorial easterly winds, the blue arrow the upwelling system and the solid red line the depth of the thermocline. Source: Collins *et al.* (2010)

1.3 El Niño / Southern Oscillation (ENSO)

The El Niño Southern Oscillation is a naturally occurring climate variability in the tropical Pacific that warms (cools) the central-east equatorial region during El Niño (La Niña) events with a frequency of 2 to 7 years (Bellenger *et al.*, 2014; Capotondi *et al.*, 2015). The atmospheric manifestation of the anomalous SST warming and cooling conditions is the large-scale east-west sea level pressure seesaw named the Southern Oscillation (McPhaden *et al.*, 2006).

A traditional view of an El Niño event starts with the tropical weather noise in boreal spring, that is, with a set of westerly wind events. It triggers a downwelling oceanic Kelvin wave, deepens the thermocline, reduces the upwelling of the cold subsurface waters in the eastern equatorial Pacific and hence, warms the central-eastern Pacific region (Timmermann *et al.*, 2018). In autumn, the anomalous warm SST displaces the upward branch of the Walker Circulation eastward from the Western Pacific Warm Pool, leading to the growth of ENSO (Philander, 1983). The result is a weakening of the trade winds along the equator as the pressure falls in the eastern Pacific and rises in the west. The consecutive eastward transport of the west Pacific warm waters ensues further positive SST anomalies (McPhaden *et al.*, 2006). The peak of the ENSO event occurs during boreal winter, coinciding with the seasonal southward displacement of the ITCZ (Philander, 1981). The warm waters associated with an El Niño event can be discharged by ocean dynamics into off-equatorial regions or by air-sea heat fluxes,

terminating the positive phase of ENSO and sometimes leading to the transition to a La Niña state (*Bellenger et al.*, 2014; *Timmermann et al.*, 2018).

In general, La Niña events could be described as the opposite phase of El Niño, in which the central-eastern Pacific obtains negative SST anomalies and the trade winds and the thermocline tilt are further increased. The result is an intensification of the Walker Circulation, with an increase of convection (subsidence) over the western (eastern-central) Pacific (*Philander*, 1985). The schematic representation of El Niño and La Niña events is shown in Figure 1.2.

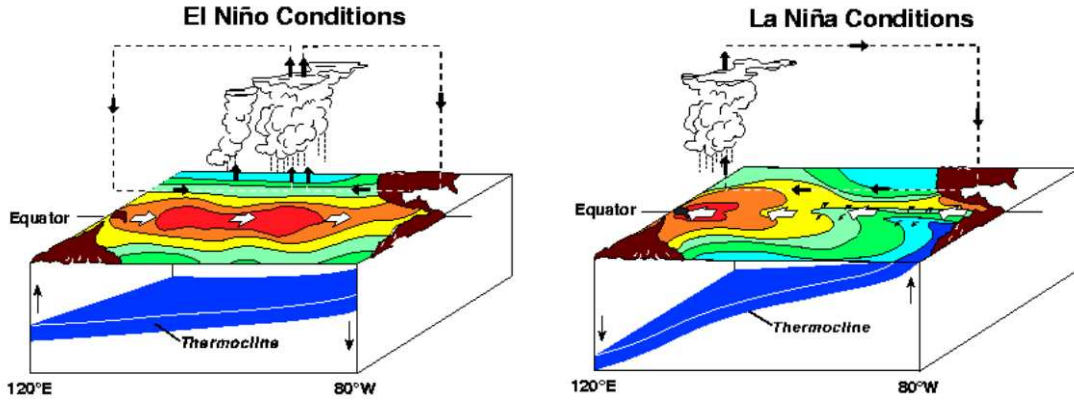


Figure 1.2: *El Niño and La Niña conditions: during an El Niño (La Niña) event the thermocline is flattened (tilted), deepening (shoaling) in the east equatorial Pacific, warming (cooling) the central-eastern regions, displacing the upper branch of the Walker Circulation eastward (westward) and weakening (strengthening) the trade winds. Source: National Oceanic and Atmospheric Administration (2019)*

Although we have already explained the evolution and characteristics of the ENSO phases in broad terms, we must realize that each event is singular and no two events are alike (*Timmermann et al.*, 2018). ENSO events can differ in amplitude, temporal evolution and spatial pattern, resulting in a high diversity of episodes with different dynamics (*Capotondi et al.*, 2015). In order to define a classification and cluster the large diversity of ENSO events, a differentiation between the East Pacific (EP) or canonical and Central Pacific (CP) or Modoki events has been made (*Trenberth and Stepaniak*, 2001; *Larkin and Harrison*, 2005; *Ashok et al.*, 2007; *Li et al.*, 2010; *Kim and Yu*, 2012). EP El Niño events, having their positive SST anomalies located next to the American continent, tend to be of higher intensity than the CP events with their anomalous SST visible over the central equatorial Pacific. In contrast, CP La Niña events are usually of larger amplitude than EP La Niña events (*Capotondi et al.*, 2015). In Figure 1.3 the SST pattern for both types of El Niño and La Niña events is visible.

Multiple indices have been defined with the objective to capture spatially varying ENSO events. In the next subsections we will introduce the different ENSO domains that have been used, and explain some of the metrics that are generally applied for ENSO research. Finally, we will explain the fundamental feedbacks that exist within the interaction between the ocean and the atmosphere, crucial for the large SST anomaly oscillations.

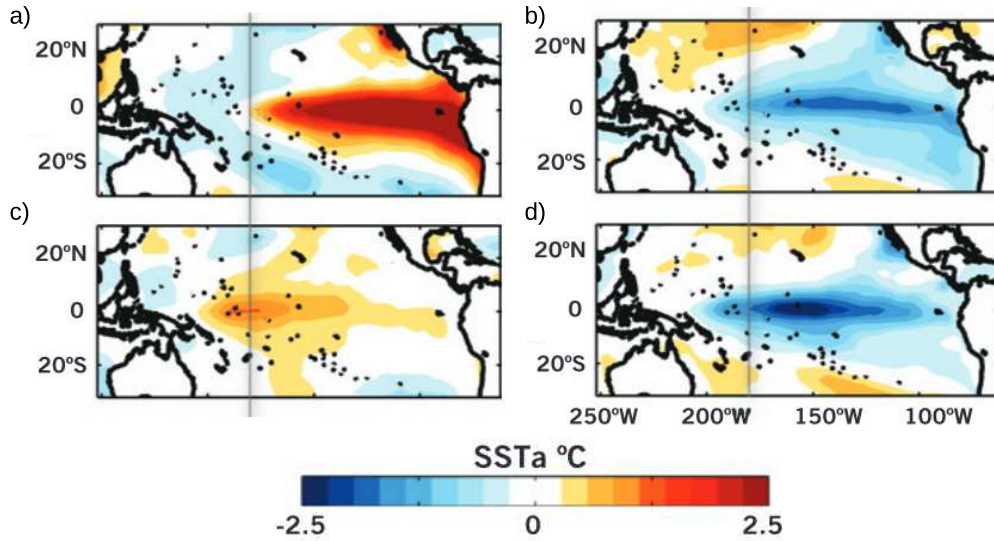


Figure 1.3: Spatial pattern of the sea surface temperature anomalies (SSTA) for specific warm and cold events: a) East Pacific (EP) El Niño event during 1997-1998, b) East Pacific (EP) La Niña event during 2007-2008, c) Central Pacific (CP) El Niño event during 2004-2005 and d) Central Pacific (CP) La Niña event during 1988-1989. Source: Capotondi et al. (2015)

1.3.1 ENSO domains

Several indices based on SST anomalies averaged over specific domains have been employed to describe and monitor the SST anomalies as part of the ENSO phenomenon. Those domains were initially located over four "Niño" regions by the Climate Analysis Center in the early 1980s (Bamston et al., 1997): Niño1 (90°W eastward, 5°S- 10°S), Niño2 (90°W eastward, 0°- 5°S), Niño3 (150°W - 90°W, 5°N - 5°S) and Niño4 (160°E - 150°W, 5°N - 5°S). However, since the Niño3 region is not capable to detect the signal of the CP El Niño events very well (Hanley et al., 2003; Li et al., 2010), a new domain was needed: the Niño3.4 region (170°W - 120°W and 5°N - 5°S).

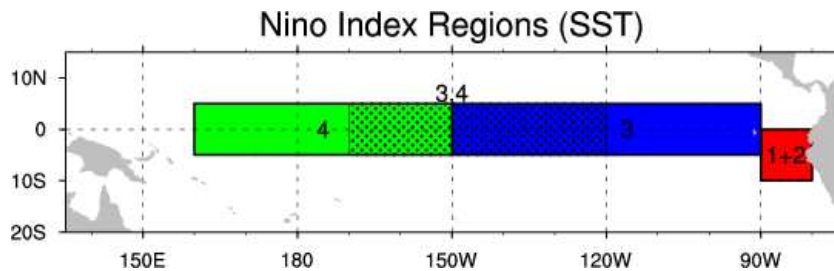


Figure 1.4: Niño index regions: Niño1+2 in red (90°W - 80°W, 0° - 10°S), Niño3 in blue (150°W - 90°W, 5°N - 5°S), Niño3.4 (170°W - 120°W, 5°N - 5°S) dotted and Niño4 (160°E - 150°W, 5°N - 5°S) in green. Source: Trenberth (2019)

The updated Niño domains (*Trenberth, 2019*), as shown in Figure 1.4, are listed in the following:

- Niño1+2: The smallest and easternmost of all Niño regions is a combination of initially differentiated Niño1 and Niño2 domains. It corresponds to the South American coastline, a region in which ENSO was recognized for the first time. It extends from 90°W - 80°W and 0° - 10°S.
- Niño3: The most frequently used geographical location for ENSO monitoring and re-searching in the past. However, when the complexity of ENSO came to light, it was discovered that CP ENSO events are not well captured by the Niño3 region. It extends from 150°W - 90°W and 5°N - 5°S.
- Niño3.4: The most sensitive and representative domain to different ENSO event flavors. It is capable of capturing the signal of both EP and CP ENSO events. It extends from 170°W - 120°W and 5°N - 5°S.
- Niño4: The westernmost Niño domain. It captures the SST anomalies in the central equatorial Pacific, and extends from 160°E - 150°W and 5°N - 5°S.

1.3.2 ENSO metrics

Although ENSO is characterized by interannual tropical Pacific SST anomaly fluctuations, with warm El Niño and cold La Niña events, the diversity of the intensity, SST anomaly pattern and temporal evolution of individual episodes leave the product of a high complexity phenomenon (*Timmermann et al., 2018*). Furthermore, ENSO characteristics suffer great modifications on decadal timescales, altering the ENSO regime (*An and Wang, 2000; Trenberth and Stepaniak, 2001; McPhaden et al., 2011; Hu et al., 2013, 2017*). In the present subsection we will introduce some of the commonly used ENSO metrics to understand the time evolution of the mentioned diversity.

In the recent years we have been able to observe a shift in the ENSO regime: compared with the time period of 2000-2011, tropical Pacific interannual variability was considerably higher during 1979-1999 (*Hu et al., 2013*). The increase in variability is observed as larger fluctuations from the mean state, that is, pronounced oscillations with a larger amplitude, which can be calculated with the standard deviation of a specific variable over a time period (*Bellenger et al., 2014; Kim et al., 2014; Wengel et al., 2017*). Similarly, because the ENSO events are referred to as SST anomalies, the ENSO amplitude must be understood as the intensity of SST variations during a specific time frame.

Nevertheless, due to the non-linear behavior of ENSO, its positive and negative phases are not symmetric: the amplitude of El Niño events are larger in comparison to La Niña (*Timmermann et al., 2018*). Hence, the ENSO asymmetry, commonly computed as the skewness, expresses the difference between El Niño and La Niña event amplitude (*Timmermann et al., 2018*).

Temporal change of the ENSO asymmetry is closely linked to the SST anomaly pattern: EP El Niño events tend to be stronger than CP El Niño episodes, while EP La Niña events are mostly weaker than CP ones (*Capotondi et al., 2015*). The SST anomaly pattern gives us the

information about the geographical location of the most anomalous SST, and hence, about the occurrence of EP or CP events.

The last metric is related to the close relation between the seasonal cycle and ENSO events. As described at the beginning of this chapter, the strongest seasonal equatorial Pacific SST variability is restricted to the boreal winter months, being the season during which the ENSO events tend to peak. The consequence is that the El Niño events will grow during the boreal summer and autumn due to the increase in ocean-atmospheric coupling (*Zebiak and Cane, 1987; Wengel et al., 2017*) and the SST anomalies will be damped during boreal spring, accompanied by the shoaling of the eastern equatorial thermocline (*Harrison and Vecchi, 1999*). The specific favorable season for the ENSO event occurrence is what we call the ENSO phase locking.

1.3.3 Atmospheric feedbacks

As we have seen, ocean-atmosphere coupling and consequent processes lead to ENSO events. In addition, the ENSO diversity partly arises from positive and negative coupled atmosphere-ocean feedbacks (*Jin et al., 2006*). Thus, the present subsection will be dedicated to the introduction of the most fundamental interactions between the ocean and the atmosphere.

A positive (negative) feedback involves a set of different processes that enhance (damp) an initial perturbation. Present theories use two feedbacks to describe the atmospheric processes that are involved in ENSO: the wind (U10) feedback and the net heat flux (NHFS) feedback (*Zebiak and Cane, 1987; Jin et al., 2006*).

The Bjerknes feedback is the most dominant positive feedback: the zonal SST gradient generated by the easterly winds is in fact increased by stronger trade winds, which in return will intensify the Walker Circulation, producing a chain reaction. The U10 feedback, the atmospheric component of the Bjerknes feedback, relates the remote zonal wind sensitivity to a given central-eastern equatorial Pacific anomalous SST and it is responsible for the generation of ENSO events (*Bjerknes, 1969; Lin, 2007; Lloyd et al., 2012*). As an example, if the zonal winds are reduced as a response of a weaker equatorial SST gradient, the equatorial Kelvin wave generated by the wind perturbation will deepen the thermocline, enhancing further heating of the central-east SST and strengthening the initial reduction of the zonal winds.

On the other hand, a negative NHFS feedback acts as a damping on the incremented SST anomalies and therefore terminates ENSO events (*Zebiak and Cane, 1987; Jin et al., 2006*). In addition, the negative NHFS feedback can be decomposed into four individual components (shortwave radiation, longwave radiation, sensible and latent heat fluxes), of which the latent heat flux (LHFS) and the shortwave (SW) feedback dominate (*Lloyd et al., 2009*). Following the previous example, an increment of the SST over the central-eastern equatorial Pacific will be followed by a thermal damping, that is, by an increment of the NHFS towards the atmosphere. Furthermore, if strong positive SST anomalies switch the convective response of the atmosphere, the increment of the total cloud cover will reduce the incoming SW radiation, reinforcing the damping of the perturbed SST and ending the ENSO event.

Nevertheless, the SW radiation can also act as a positive feedback when the SST anomalies obtain negative values, that is, during La Niña events. In a subsidence state, when the SSTs are incremented, the destabilization of the atmospheric boundary layer prevents the formation of stratiform boundary layer clouds. The result is an increment of the incoming SW radiation and

an enhancement of the initial perturbed SST (*Philander et al.*, 1996; *Xie*, 2004). Hence, the study of the SW feedback is not only relevant for the ENSO phase locking or the ENSO event termination, but also gives relevant information about the capability of the model to simulate the atmospheric switch from subsidence (positive SW feedback) to convective (negative SW feedback) state (*Bellenger et al.*, 2014).

Chapter 2

Data and Methodology

In this chapter we will introduce the data and the methodology used in the present thesis.

2.1 Data

2.1.1 GFDL-ESM2M

The core of the present thesis will study a 500 year-long pre-industrial control run simulated by the coupled carbon-climate Earth System Model from the Geophysical Fluid Dynamics Laboratory GFDL-ESM2M. The monthly data used is available on the Coupled Model Inter-comparison Project Phase 5 (CMIP5) panel and the complete model description can be read in *Dunne et al. (2012)* and *Dunne et al. (2013)*.

Within the CMIP5 model ensemble the pre-industrial control run, often abbreviated as piControl, is referred to as the initial stage of the long model simulations, a continuation of the spin-up process, in which the forcing of greenhouse gases (CO_2) is maintained to pre-industrial times. Therefore, the unforced simulation will provide us with information about the natural variability of the system (*European Network for Earth System Modelling, 2019*).

The Earth System Models (ESMs) incorporate the interactions between the atmosphere, ocean, land, ice and biosphere, including processes, impacts and complete feedback cycles (*Heavens and Mahowald, 2013*). The GFDL-ESM2M model has been developed from the previous Climate Model version 2.1 (GFDL-CM2.1), incorporating carbon dynamics. The new GFDL generation consists of two new global coupled carbon-climate ESMs, the present ESM2M and the ESM2G, differing exclusively in the ocean component. Although neither model has better generic simulation skills, the ESM2M model is advised to be used for the tropical Pacific circulation and variability research (*Dunne et al., 2013*).

A set of variables is used along the research. Besides the sea surface temperature (SST), necessary for the ENSO analysis, the subsurface temperatures (T), surface zonal winds (U10), vertical winds at 500 hPa height (W500), precipitation (PR), total cloud cover (CLT) and net surface heat fluxes (NHFS) are incorporated in our study in order to analyze the atmospheric state and response. The NHFS's dominant components are also applied: the latent heat flux (LHFS) and the shortwave (SW) radiation.

A brief description of the different GFDL-ESM2M components and their coupling is provided next:

a. Atmosphere

The atmospheric component is identical to its predecessor CM2.1, the Atmospheric Model version 2 (AM2). It has a 2° latitudinal x 2.5° longitudinal horizontal resolution with 24 vertical layers. The grid scheme used is the D grid, with 3 hours radiation and 0.5 hour dynamical time steps.

b. Ocean

The ocean model applied is the Modular Ocean Model version 4p1 (MOM4p1) set to vertical pressure layers. The horizontal grid resolution of 1° in latitude and longitude is progressively finer reaching $1/3^\circ$ at the equator. Above 65°N , a tripolar grid is used with poles over Eurasia, North America and Antarctica. In this case, the model consists of 50 vertical levels, with 10 m thickness in the first 220 m.

c. Land

Integrating the land water, energy, and carbon cycles, the Land Model version 3 (LM3.0) is applied. The land water accounts for a multilayer snowpack, continuous vertical soil water with saturated and unsaturated zones, frozen soil water, groundwater discharge, river runoff, lakes as well as lake ice and lake snowpack. Vegetation canopy and leaves are considered for the radiation, the water cycle and carbon dynamics.

d. Sea Ice

The sea ice model, Sea Ice Simulator (SIS), considers full ice dynamics, two ice layer and one snow layer thermodynamics, and five ice thickness division. The ice albedo differentiates, when the snow on ice is considered (0.80) and without snow (0.65), and the melting temperature is set to 1°C .

d. Icebergs

The origin of icebergs is accounted for, when the snow depth of LM3.0 exceeds a critical value. Then, the excessive snow pack is transported to the ocean-sea ice compartments by rivers as a Lagrangian particles dragged by the ocean, sea ice and atmosphere.

e. Coupling

For the coupling of the Earth System Model's components the Flexible Modeling System (FMS) has been employed. The fluxes are passed across the component's interfaces by the exchanging grid system. The coupling between the atmosphere, land and sea ice radiation is set to occur

every 0.5 hour, while the tracer-coupling between the ocean and the atmosphere occurs every 2 hours.

2.1.2 ERA-20C

The European Centre for Medium-Range Weather Forecast (ECMWF) twentieth century re-analysis product (ERA-20C) contains global atmospheric data between the period of 1900-2010. It is the first ECMWF reanalysis precisely constructed for long term climate analysis. Hence, it will be our reference tool to keep track of the GFDL-ESM2M model realism.

The Integrated Forecast System version Cy38r1 (IFS-cy38r1), which incorporates an atmospheric general circulation model (AGCM) and a variational scheme, allows a medium range forecast. IFS could be defined as the environment, where the data assimilation and forecasting activities performed at ECMWF meet. The forecast assimilation is set to 24 hour cycles, from which the analysis is obtained for each cycle by combining observations with the model forecast estimates, initialized from the previous cycle analysis.

The model integrations are based on a spectral T159 horizontal resolution, the equivalent of about 125 km, and 91 vertical levels from 10 m above the surface up to 1 Pa, that is, 80 km approximately. The prescribed model forcing, sea surface temperature and sea ice concentration, are obtained from HadISST version 2.1.0.0. The solar radiation, tropospheric and stratospheric aerosols, ozone and greenhouse gases forcing sources on the other hand are as specified for CMIP5 experiment. The observations encompasses the atmospheric surface pressure data from the International Surface Pressure Databank version 3.2.6 (ISPD-3.2.6) and the International Comprehensive Ocean-Atmosphere Data Set version 2.5.1 (ICOADS-2.5.1). A second observational input are the marine wind reports from ICOADS.

An exhaustive quality control has been applied to the observations, rejecting the data in the next cases: the data at exactly 0°latitude and 0°longitude except for a PIRATA mooring array buoy located at that location; observations of wind in specific locations such as near the coastlines or seas surrounded by mountains, because of the coarse model resolution; ICOADS ocean-profiling instrument data; station and ship observations are not rejected, but avoided if there are at least three observations with a constant 5-day window; data that exceeds more than 7 times the expected value extracted from the model ensemble. The accepted observational surface pressure data goes from 30000 to 3.6 million between 1900 - 2010.

Different techniques and indices have been used to demonstrate the reliability of the reanalysis product. For instance, the variability of the Niño3.4 index shows similar behavior when comparing the ERA-20C to other reanalysis products: Japanese 55-year Reanalysis (JRA-55), 20th Century Reanalysis version 2 (20CRv2) and ERA-Interim. Although all the reanalysis products contain prescribed SSTs, the input source is different for each of the mentioned reanalysis outputs. Nevertheless, some of the early 20th century ENSO events are exaggerated in magnitude. In fact in comparison to 20CRv2, the ERA-20C differs greater before 1940 than after. For more detailed information related to the reanalysis product one should look into *Hersbach et al.* (2013) and *Poli et al.* (2016).

Due to the fairly realistic ENSO amplitude and relatively long time-period, which allows us to study the climate variability, the ERA-20C has been chosen to be our reference and comparison to the results obtained with the GFDL-ESM2M climate model. The monthly

sea surface temperatures (SST), surface zonal winds (U10), vertical winds at 500 hPa height (W500), precipitation (PR), total cloud cover (CLT), net surface heat flux (NHFS), latent heat flux (LHFS) and shortwave radiation (SW) are extracted from the ECMWF website.

2.2 Methodology

2.2.1 Model mean state bias

Before starting with any ENSO analysis, the mean model biases are analyzed for the tropical Pacific region relative to ERA-20C reanalysis product. The tropical Pacific region has been confined to 20°N - 20°S and east of 120°E reaching the central-south American continent. The main relevant mean state biases shown by multiple climate models are known to be expressed in the SST and U10, representing an anomalous Walker Circulation intensity and location (*Davey et al.*, 2002; *Dommenget et al.*, 2014; *Bayr et al.*, 2018).

First of all, the mean state of the defined tropical Pacific region was calculated and compared for the SST and U10 variables. For the mean SST comparison, instead of using absolute values, we have obtained the relative values after subtracting the tropical Pacific area mean value. The reasons to use the relative SST, as explained in *Bayr et al.* (2018), are mainly two: first, the comparison is more easily accomplished between two climates with different mean temperatures, and second, the dependence of tropical atmospheric circulation is higher on relative values than on absolute ones. Nevertheless, in order to relate our findings of model bias to previous studies, the absolute mean SST biases are computed as well.

In addition, we have put our attention on the equatorial Pacific mean state (5°N - 5°S) biases, extending the analysis to W500, NHFS, CLT and PR variables in order to obtain further information about the location and intensity of the Walker Circulation.

2.2.2 ENSO definition

For the ENSO characteristic analysis we have selected the Niño3.4 region as the main study area. Although the Niño3 has been applied by several authors (*Rodgers et al.*, 2004; *Wittenberg*, 2009; *Lloyd et al.*, 2012; *Bellenger et al.*, 2014; *Atwood et al.*, 2017), the Niño3.4 box (170°W - 120°W and 5°N - 5°S) has been defined as the most appropriate and generic one in order to capture the spatially varying ENSO (*Bamston et al.*, 1997). According to *Hanley et al.* (2003), the Niño3.4 index is more sensitive to different flavors of El Niño events than the Niño3 region. In fact, the Niño3 index doesn't capture the signal of CP El Niño events well (*Li et al.* (2010)). Hence, similarly as in *Santoso et al.* (2017), El Niño or La Niña events will be computed, when the Niño3.4 SSTAs exceed half a SST standard deviation for at least 5 consecutive months, and in our case the strong events are considered by setting a threshold of a doubled standard deviation.

Due to the large extent of our time series and the variability of the background mean state, the mean values (seasonal cycle) that we use to obtain the monthly anomalies are computed relative to a 30 year running window. The main reason to choose a 30 year window length is that the World Meteorological Organization (WMO) defines a classical period of 30 years to study the climate. Furthermore, since our interest is focused on decadal timescales and the ENSO

events tend to have a varying periodicity of occurrence between 2 and 7 years (*Bellenger et al.*, 2014), we need at least 30 years to account for decadal periods of different ENSO behavior. Similarly, for the rest of variable anomalies we have subtracted the seasonal mean of the 30 year running window as well. The only exception is made for the sections in which we study specific time periods of the 500 year control run. In those cases, since the time period is already restricted, the seasonal cycle of the whole defined period has been computed.

Although the Niño3.4 index is not capable of distinguishing between the two types of ENSO events, this will be achieved by combining it with the Trans-Niño Index (TNI) (*Trenberth and Stepaniak*, 2001). TNI aims to capture the spatially varying SSTA, separating the eastern basin SSTA or EP events from the central-western SSTA or CP events. The original index computes normalized Niño1.2 SSTA and subtracts the normalized Niño4 SSTA. Then, if the largest anomalies are found on the east (west), TNI will obtain positive (negative) values and the ENSO event will be defined as EP (CP). Due to the GFDL-ESM2M model bias, which represents the strongest SST variability anomalously away from the south American continent and therefore out of the Niño1.2 region, the mentioned index has to be modified (Equation 2.1). For our particular study the eastern box have been shifted to 130°W - 90°W and 5°N - 5°S, while the western box has been transferred to 170°E - 140°W.

$$TNI = SSTA_{E_N} - SSTA_{W_N} \quad (2.1)$$

$SSTA_{E_N}$ and $SSTA_{W_N}$ represent the eastern and western normalized SST variability, respectively. The standardization is achieved by subtracting the monthly SST mean of the 30 year running window and dividing it by the standard deviation of the same window length.

2.2.3 ENSO metrics

For the ENSO representability, different metrics have been applied and compared to ERA-20C. The ENSO asymmetry, that is, the difference in amplitude between El Niño and La Niña events, is computed as the skewness of interannual variability of SST (*Burgers and Stephenson*, 1999). After computing the Niño3.4 SSTA, the skewness of the probability density function will provide us with information about the ENSO asymmetry. In addition, to find the regions of strongest ENSO asymmetry, the mentioned skewness has been calculated for each tropical Pacific spatial grid point using the SSTAs and U10 anomalies (U10A) (*Atwood et al.*, 2017).

The seasonal dependence on the SST variability, also called the ENSO phase locking, is the second metric. The SST variability is increased during the months of boreal autumn, peaks in winter and is considerably decreased during spring (*Rasmusson and Carpenter*, 1982). To prove the reliability of the GFDL-ESM2M's ENSO phase locking, we have computed the standard deviation of Niño3.4 SST for each month. Nevertheless, in order to relate the seasonal SST variability to other Niño regions, the study of the seasonality is also extended to the whole equatorial (5°N - 5°S) Pacific by using the Hovmöller diagram.

The third metric corresponds to the spatial pattern of SST variability during the ENSO events. For this purpose we have computed the El Niño and La Niña composites and show their tropical Pacific SSTA patterns. Independently analyzing them, we can investigate if there is any anomaly, when representing ENSO event location. Furthermore, combining both composites

and taking into account the ENSO asymmetry, we can investigate the plausible effects onto the mean tropical Pacific state that the residual of El Niño and La Niña events could have.

The ENSO amplitude was detected as in *Bellenger et al.* (2014), calculated as the standard deviation of SST, but in our case over the Niño3.4 region. Because our main interest is focused on the decadal variability of the ENSO amplitude, a 30 year running standard deviation has been used to expose the long term variability. In order to compare the decadal ENSO amplitude with ENSO event frequency and EP - CP ENSO flavors, the 500 year time series has been split into 30 year bins, detecting the ENSO events with the above explained technique and distinguishing the EP-CP events by the modified TNI index for each binned period of time. Finally, the sequence of El Niño - La Niña events is analyzed by applying the Niño and Niña composite in the Hovmöller diagrams, extending the time evolution of SSTA over the equatorial Pacific 20 months before and after the month of December.

2.2.4 Atmospheric feedbacks

The mean state and variability of the tropical Pacific climate is strongly determined by coupled ocean-atmosphere feedbacks (*Lin*, 2007). A generic classification of those feedbacks in the tropical climate divides them, depending on their positive or negative sign. The two most common feedbacks that consider atmospheric processes are the U10 feedback and the NHFS feedback (*Zebiak and Cane*, 1987; *Jin et al.*, 2006). With a positive sign, the U10 feedback, or the atmospheric component of the Bjerknes feedback (*Bjerknes*, 1969), is measured as the distant zonal wind response to an anomalous SST over the central-eastern equatorial Pacific (*Lloyd et al.*, 2012). The anomalous westerly (easterly) wind anomalies cause a decrease (increase) of the zonal SST gradient by flattening (tilting) the thermocline slope. In return, the weakening (strengthening) of the SST gradient further damps (excites) the easterly winds, forming a positive feedback. Similarly, a positive SSTA over the central-eastern tropical Pacific switches an anomalous local convection state instead of a commonly observed subsidence. The convection causes higher precipitation, which increases the heat by latent energy, and cloud cover and water vapor which act as radiative heating. Hence, a positive feedback is formed. Following *Lloyd et al.* (2009) the U10 feedback is computed as a linear relation shown in Equation 2.2, where τ'_x represents the U10A, being a product of the SSTA (SST') and the U10 feedback (μ).

$$\tau'_x = \mu \times SST' \quad (2.2)$$

The main negative feedback, the process which damps the anomalous SSTs, is the NHFS feedback. The SST anomalies are responded to by thermodynamic changes: positive SSTA will cause an increase of heat loss, mostly by latent fluxes and the reduction of incoming SW radiation by the increase of CLT. To a lesser extent, sensible flux and long-wave radiation also affect the excited SSTs (*Lloyd et al.*, 2009). The NHFS feedback computation is visible in the Equation 2.3. Similarly as in Equation 2.2, the negative feedback (α) is obtained by the relation between the NHFS anomalies (NHFSA) (Q') and SSTA. Following the same procedure, we have applied the same equation to the two most dominant NHFS components: the LHFS and the SW radiation (*Lloyd et al.*, 2009, 2012).

$$Q' = \alpha \times SST' \quad (2.3)$$

First of all, the linear relation between the mentioned variable anomalies and the Niño3.4 SSTA are computed for each tropical Pacific grid point. Once we have detected the region with U10 and NHFS sensitivities, it will be used to calculate the temporal evolution of the feedback. For instance, the U10 feedback maximum values are located over the Niño4 area, while for the NHFS feedback we will combine the Niño3 and Niño4 boxes.

2.2.5 Decadal ENSO amplitude modulation

In order to understand the possible causes and consequences of the decadal ENSO amplitude variability, we have detected and differentiated between two time periods of high and low ENSO amplitudes: the High and Low epochs. After setting both periods to the same temporal length of 60 years, we have studied the mean state and variabilities of the tropical Pacific natural system for the SST, T, U10, W500, NHFS, PR and CLT. The interannual variability has been computed as the standard deviation, obtaining the anomalies relative to the 60 year seasonal cycle. *Ogata et al.* (2013) separated the studies relating the mean state and the ENSO amplitude into two groups: the ones that look into the ENSO amplitude response when different stochastic forcing are applied to multiple mean states, and the second ones examining the interaction between the mean state and the ENSO amplitude.

Our research would fit into the second study-type: besides the mean state and interannual variability, we have calculated the whole ENSO characteristics and linear atmospheric feedbacks for both epochs. This will help us understand the possible effects of the ENSO metrics differences, like its amplitude, asymmetry and spatial pattern onto the mean state.

Furthermore, the possible causes for the ENSO decadal variability are investigated. A linear Pearson correlation has been used to study the relation between the ENSO amplitude, atmospheric feedbacks and the mean state.

Following *Bellenger et al.* (2014), our last but not the least important focus is set on the non-linear expressions of the GFDL-ESM2M coupled climate model feedbacks. Our intention is to obtain further information about the possible causes for the decadal ENSO amplitude modulation. We have split the months between positive and negative Niño3.4 SSTA, for both the High and Low epochs, and then obtain separate linear relationships with U10A to understand the wind sensitivity to surface temperature anomalies.

Similarly, we have applied the SW anomalies (SWA) into our non-linear analysis, which is known to be the main source of ENSO error within climate models (*Kim and Jin*, 2011). In observations, the SW feedback is captured as a positive feedback, when SSTAs obtain negative values. In a subsidence regime, a SST increase will cause a destabilization of the atmospheric boundary layer, restricting the stratiform cloud formation, increasing the SW radiation and in turn increase the SST. On the contrary, when the SSTAs are positive, that is, in a convective regime, the SW feedback is turned negative. In this case an increase of SST will produce an increment of CLT, a decrease of the incoming SW radiation and a reduction of the perturbed SST (*Philander et al.*, 1996; *Xie*, 2004). From this analysis we will retain information about the ability of the model to demonstrate the system's shift between convective/subsidence regimes.

The next non-linear variability shown in our research is related to W500 anomalies, which in fact will provide further information about the ability of the system to shift from subsidence to convective state. The strongest subsidence region during the Low epoch is situated over

the Niño3 box, a domain in which the vertical wind variability differs the most and strong EP events occur during the High epoch. Hence, the non-linear analysis in this case will involve the Niño3 area.

The last possible non-linear relation with the decadal ENSO amplitude has been attributed to the mean thermocline slope. The thermocline depth is computed as the strongest vertical temperature gradient instead of the commonly used 20°C isotherm. The second mentioned approach of the thermocline is not recommended under long-term mean state changes (*Yang and Wang, 2009*). Similarly as in *Hu et al. (2013)*, who demonstrated that a too large or too weak thermocline tilt decreases the ENSO amplitude forming a concave function, the thermocline tilt is calculated by the difference of the mean thermocline depth between the eastern and western equatorial Pacific. The western box is set to 160°E - 170°W, 5°N - 5°S and the eastern area to 120°W - 90°W, 5°N - 5°S. In order to represent the decadal relationship, we have applied a 30 year running mean to the monthly thermocline tilt data.

Chapter 3

Results

3.1 ENSO simulation skills

The GFDL-ESM2M model is known to reproduce relatively realistic ENSO dynamics and it has been chosen as one of the best coupled climate model option within the CMIP5 group (*Kim and Jin, 2011; Bellenger et al., 2014; Kim et al., 2014; Capotondi et al., 2015*). Furthermore, its strong atmospheric feedbacks have been found to be relatively close to the observations (*Bayr et al., 2019*). In the first chapter we will analyze some of the characteristics of the present climate model, comparing it to the ERA-20C reanalysis product, starting from the mean state model bias and continuing with the relevant ENSO statistics and feedbacks. Both the mean state and feedbacks are important factors to obtain good ENSO dynamics, as it has been proven in many previous studies (*Kim and Jin, 2011; Lloyd et al., 2012; Ham et al., 2013; Dommenget et al., 2014*). Therefore, this section will be of great importance in order to understand the behavior of the simulation obtained with the GFDL-ESM2M climate model.

3.1.1 Model bias in the mean state

Many climate models have relevant issues when simulating the realistic representation of the tropical Pacific mean state. One example is the cold SST bias over the equatorial region. The cold tongue bias, as the negative bias in the mean state is called, simulates a continuous La Niña-like state: the cold SST over the equatorial Pacific leads to an intensification of the easterlies west of the Niño4 region, pushing the western Pacific convective region westward, and hence displacing the rising branch of the Walker Circulation. If the rising branch is located too far west, the convective response is greatly decreased and therefore the strength of the U10 and NHFS feedbacks is reduced, causing different ENSO dynamics (*Davey et al., 2002; Bayr et al., 2018*).

The chosen model for this research is not an exception. Figure 3.1 demonstrates the differences in the representation of the mean tropical Pacific SST. In order to make the comparison easier, instead of the absolute temperatures, we show the mean SST relative to the area mean of the tropical Pacific (120°E-80°W, 20°N-20°S). In addition, the distribution of the relative SST has a larger impact on the tropical atmospheric circulation than the absolute values (*Bayr and Dommenget, 2013*).

Although the general pattern of the relative SST is similar to ERA-20C reanalysis product with warm temperatures on the west and cold on the east, the gradient or the transition from positive to negative relative SST is shifted 60° to the west, confining the Pacific Warm Pool to the very western equatorial region, and displacing the minimum SST values away from the South American coast. Furthermore, the SST difference between the GFDL-ESM2M and ERA-20C (Figure 3.2a) demonstrate a negative equatorial SST bias above 1°C , and a positive bias above 3°C along the South American coastline. Due to the cold bias the atmospheric circulation shows an anomalous pattern: stronger easterlies over the Niño4 region and west of Central America are found, while off the coast of Peru weaker mean zonal winds are visible (Figure 3.2b).

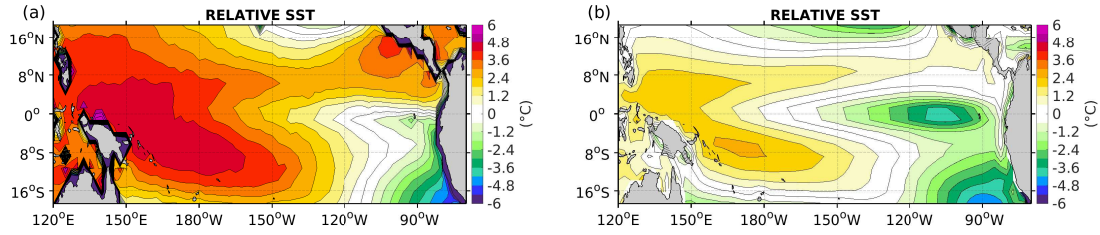


Figure 3.1: The mean sea surface temperature (SST) relative to the area mean tropical Pacific SST for: a) ERA-20C, and b) GFDL-ESM2M.

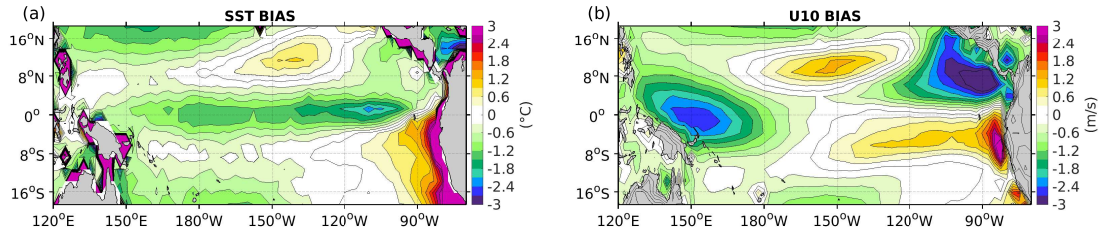


Figure 3.2: Mean state model bias for a) the sea surface temperature (SST), and b) the surface zonal winds (U10), obtained by the difference between the GFDL-ESM2M model and the ERA-20C reanalysis product.

Figure 3.3 represents the zonal equatorial structure (5°N - 5°S) of the relative SST, U10, W500, NHFS, CLT, and PR. The mentioned cold bias strengthens the easterly winds west of 150°W , pushing the rising branch of the Walker Circulation 15° to the west. In addition, the rising branch of the Walker Circulation causes too high CLT and PR and too weak NHFS, while on the eastern side the too strong subsidence state shown by the downward winds leads to less CLT and PR with a stronger NHFS when comparing to ERA-20C.

Hence, due to the equatorial cold bias and a constant La Niña-like state, the rising branch of the Walker Circulation is located far too west and the subsidence state is anomalously strong, extending slightly west of the date line.

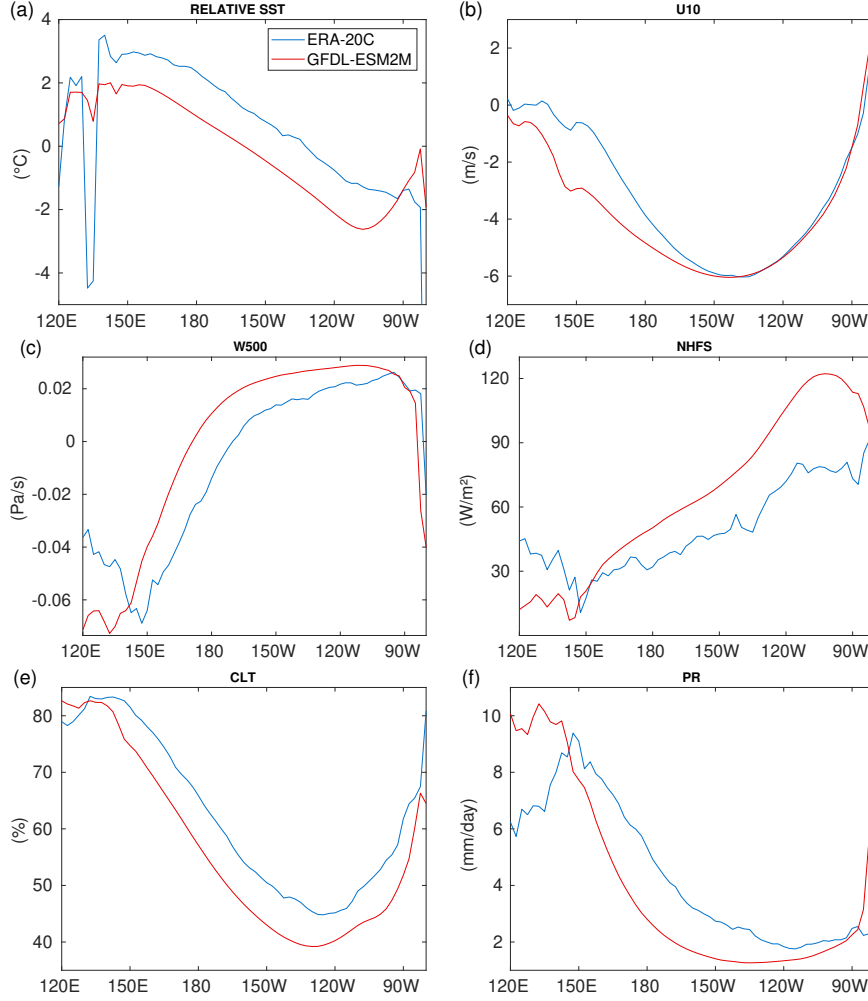


Figure 3.3: Equatorial Pacific mean state (5°N - 5°S) of a) sea surface temperature (SST), b) surface zonal winds (U_{10}), c) vertical wind at 500 hPa height (W_{500}), d) net heat flux ($NHFS$), e) total cloud cover (CLT) and f) precipitation (PR). GFDL-ESM2M in red and ERA-20C in blue.

3.1.2 ENSO metrics

In the present subsection we will pay attention to the ability of the GFDL-ESM2M climate model to reproduce multiple ENSO characteristics.

First of all we must highlight its strong non-linear behavior when simulating the ENSO events, as presented by the probability density function (PDF) of Niño3.4 sea surface temperature anomalies (SSTA) (Figure 3.4). In both cases, ERA-20C and GFDL-ESM2M, the distribution has a positive skewness: the tail of the PDF is elongated towards positive values, representing stronger positive SSTA than negative ones. However, the climate model's skewness is about three times larger than that of ERA-20C, 0.42 and 0.16 respectively, revealing that the GFDL-ESM2M model has relatively stronger El Niño than La Niña events.

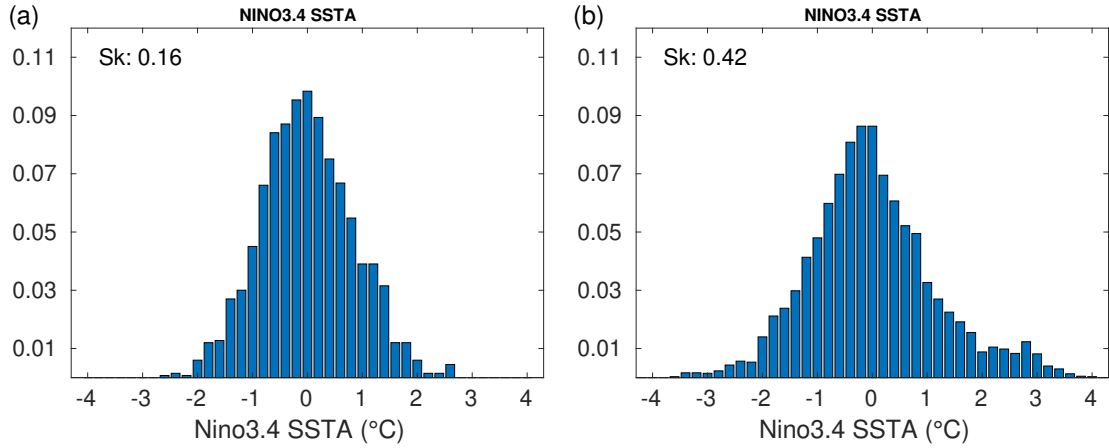


Figure 3.4: Probability density function of Niño3.4 sea surface temperature anomalies (SSTA). The skewness value, representing the ENSO asymmetry, is displayed in the upper left corner of the plots: a) ERA-20C, and b) GFDL-ESM2M.

The geographical distribution of the tropical Pacific SSTA skewness (Figure 3.5) also displays relevant differences. Both the map for ERA-20C and GFDL-ESM2M show a dipole pattern: positive skewness on the east equatorial Pacific resembles stronger positive SSTAs than negative, that is, stronger El Niño than La Niña events. However, when El Niño is developing, the oceanic heat content is displaced from the western equatorial Pacific towards the east, and hence, negative SSTAs are located over the edge of the Pacific Warm Pool: positive skewness in the east is related to negative skewness in the west. It must be said that both representations agree on the location of the highest skewness: the strongest asymmetries are situated on the eastern Pacific, the location of the so called EP El Niño events.

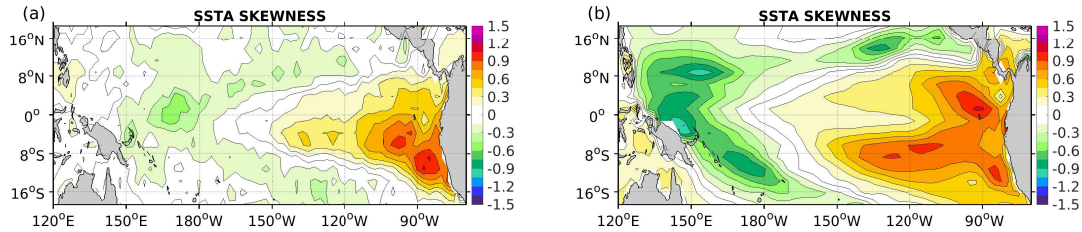


Figure 3.5: Skewness map of tropical Pacific sea surface temperature anomalies (SSTA) for a) ERA-20C, and b) GFDL-ESM2M.

Nevertheless, the extension of the mentioned positive skewness is exaggerated into two main regions (south and northeast equatorial regions) and the negative skewness is displaced far too the west, agreeing with the location of the Pacific Warm Pool being too far west. Because of the cold equatorial bias and strong western equatorial U10, the edge of the Pacific Warm Pool is limited to the west, allowing the strong positive SSTA to spread further west and limiting the eastward extension of the negative skewness in the climate model. In addition, both the positive and negative skewness are anomalously large in the model.

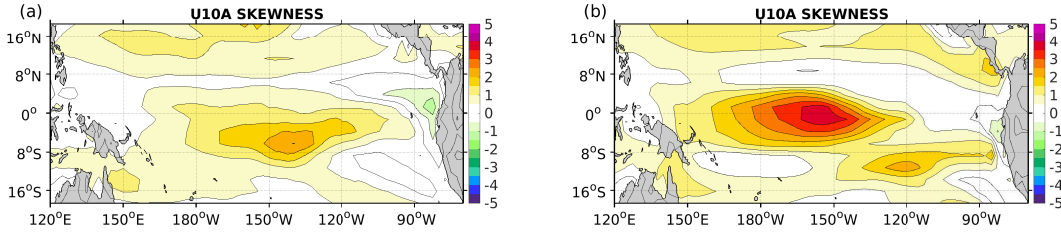


Figure 3.6: Skewness map of tropical Pacific surface zonal wind anomalies (U_{10A}) for a) ERA-20C, and b) GFDL-ESM2M.

Similarly, the skewness of U_{10A} (Figure 3.6) is positioned far too the west compared to ERA-20C and the stronger values illustrate the highly non-linear behavior of the GFDL-ESM2M coupled model once more.

Another important ENSO characteristic is its phase locking. The highest Niño3.4 SST standard deviation is two months delayed for the the climate model (Figures 3.7a,b,c). Nevertheless, the model is capable of reproducing the highest Niño3.4 SST standard deviation during boreal winter months along with the damping of its variability during spring. This is a relatively close approximation to realistic ENSO dynamics, in which ENSO grows during autumn, peaks in the winter months and is damped during spring (*Rasmusson and Carpenter, 1982*). A second smaller peak of the standard deviation is visible during the month of July. The anomalous double peak of SST variability is due to the double (semiannual) ITCZ and the seasonal reversal of the meridional SST gradient and winds in the east (*Wittenberg et al., 2006*). The Hovmöller diagram of latitudinally averaged (5°N - 5°S) SST variability represents the mentioned behavior: both peaks are equally strong, but during boreal summer months the variability is extended further west, capturing it by the Niño3.4 region with higher magnitude (Figure 3.7c).

The geographical position of the SSTA using El Niño and La Niña composites is visible in Figure 3.8. As shown before, both the positive and negative SSTA extend too far west in the present climate model and its intensity is greatly enhanced when comparing to ERA-20C. The largest positive SSTA is located at 120°W and the negative SSTA is slightly shifted westward. The reanalysis product, on the other hand, has both a positive and negative SSTA maximum centered in the equatorial Pacific section. The difference between the effects of El Niño and La Niña events, that is, their residual, is demonstrated by adding both composites. El Niño events tend to warm the very eastern section, while La Niñas affect more strongly the western region. The result is a dipole pattern for both the climate model and the reanalysis product. The differences are visible in the magnitude and the location: the climate model has a stronger dipole pattern with the negative values located too far west.

Although the GFDL-ESM2M is known for its relatively realistic ENSO dynamics, it seems that it has difficulties to reproduce proper ENSO characteristics: the ENSO asymmetry is anomalously large, the phase locking is delayed, it shows a double SSTA standard deviation peak, and La Niña and El Niño events tend to extend too far west along the equatorial Pacific. In addition, the present climate model doesn't seem to reproduce realistic EP El Niño events, which they are located off the South American coast.

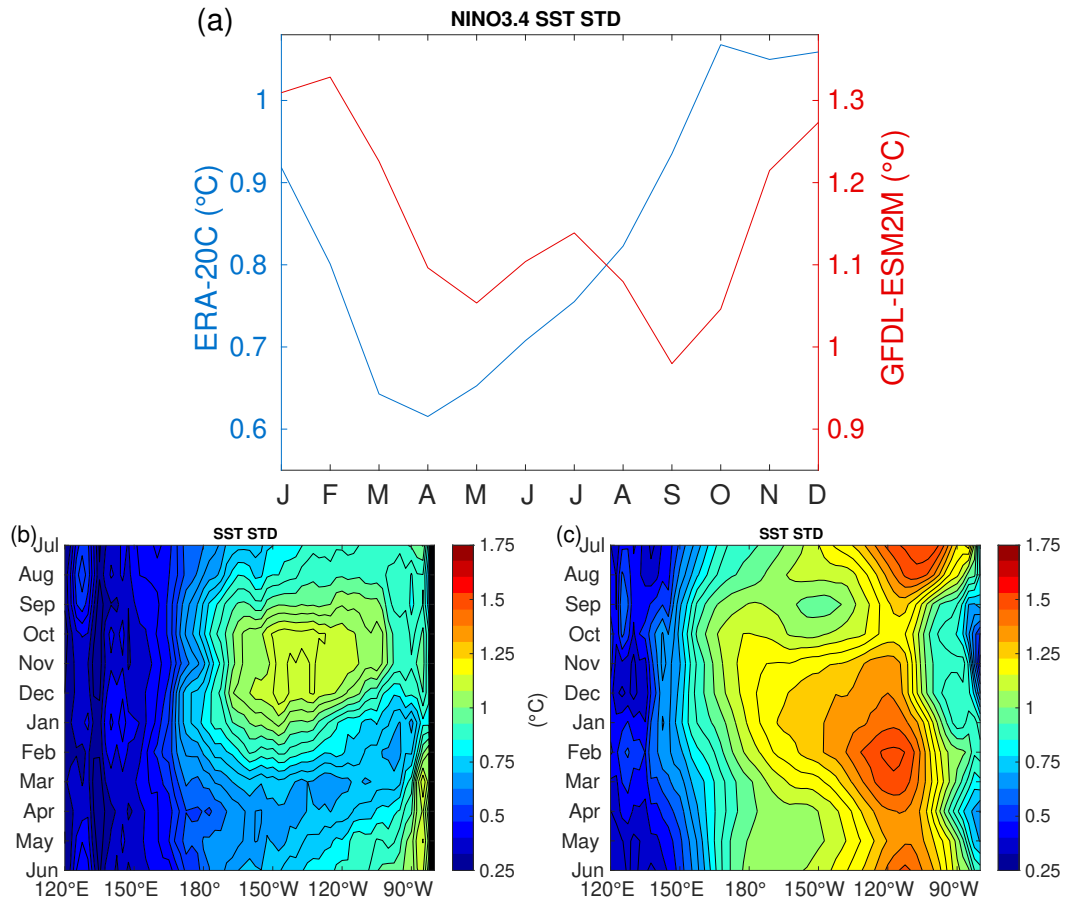


Figure 3.7: Monthly standard deviation of the sea surface temperatures (SST) over: a) the Niño3.4 region, ERA-20C in blue and GFDL-ESM2M model in red, b) the Pacific equatorial (5°N-5°S) region for ERA-20C, and c) the same as b) but for GFDL-ESM2M.

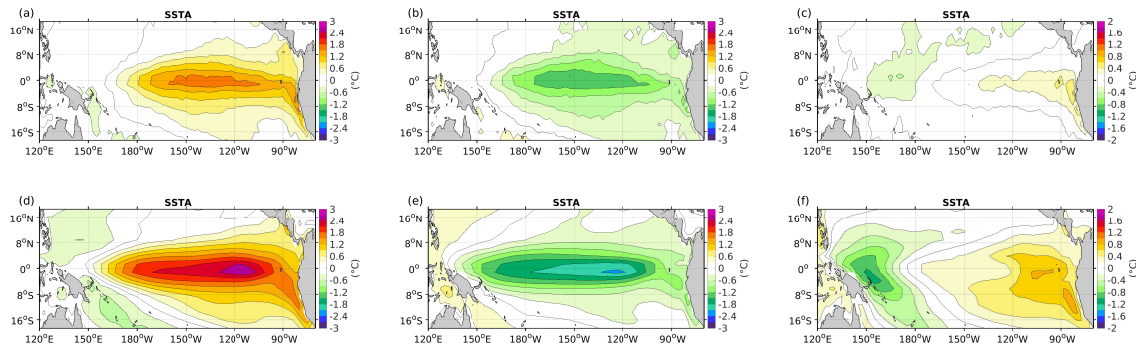


Figure 3.8: Geographical location of ERA-20C reanalysis product tropical Pacific sea surface temperature anomalies (SSTA) from a) El Niño composite, b) La Niña composite, and c) their residual obtained by adding both composites. Similarly, d) e) and f) correspond to the GFDL-ESM2M model.

3.1.3 Atmospheric feedbacks

The atmospheric positive and negative feedbacks are of great importance for inducing ENSO growth and damping, respectively. Hence, their correct simulation will cause a substantial improvement on the ENSO properties such as El Niño/La Niña asymmetry or phase locking (Bayr *et al.*, 2018). Bayr *et al.* (2018) state the dependence of the SST mean state on simulating the ENSO atmospheric feedbacks. They concluded that the U10 and NHFS feedbacks act linearly depending on the equatorial SST mean state, compensating each other's biases, but leading to erroneous ENSO properties.

The wind is known to act as a positive feedback: the positive SSTA over the Niño3.4 region decreases the zonal SST gradient over the equatorial Pacific, and hence the zonal winds on the eastern equatorial region and the thermocline tilt are reduced, inducing a further heating: the Bjerknes feedback (Bjerknes, 1969). In contrast, the NHFS acts to reduce the oceanic heat content when SSTA increases. LHFS and SW radiation are the dominant variables affecting the NHFS (Lloyd *et al.*, 2009). For instance, when positive SSTA are located over the Niño3.4 region, higher evaporation releases a larger amount of heat energy, increasing the LHFS. Increasing the cloud cover over the anomalous SST region reduces the incoming SW radiation towards the surface of the ocean by reflecting it back: the albedo effect. Therefore it is considered to be a negative feedback, which plays a major role in damping ENSO events during the months of spring (Dommenget and Yu, 2016; Wengel *et al.*, 2017).

Applying a simple polynomial fit of the first order, we get a linear regression that relates U10 and NHFS anomalies to Niño3.4 SSTA. The slope of the polynomial fit will be the strength of the feedback.

The first step for the feedback analysis is to detect the regions in which the U10 and NHFS are affected the most by the Niño3.4 SSTA. Therefore, we will compute the feedbacks for each spatial grid point along the tropical Pacific, relating U10A and NHFSA to Niño3.4 SSTA.

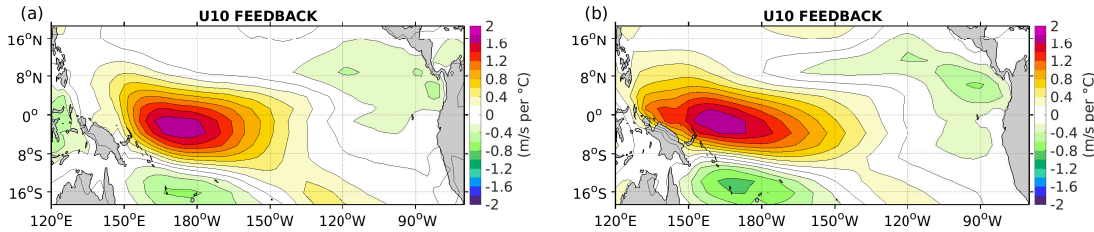


Figure 3.9: Linear wind (U10) feedback: anomalous surface zonal wind (U10A) sensitivity to Niño3.4 sea surface temperature anomalies (SSTA) for each tropical Pacific grid point for a) ERA-20C, and b) GFDL-ESM2M.

Figure 3.9 shows the linear relationship between the Niño3.4 SSTA and U10A. In this case, we must say that the U10 feedback simulation is very similar to the reanalysis product, both in strength and location. For the GFDL-ESM2M model however, the positive feedback still shows strong values west of 150°W, probably due to the effects of the mean SST bias. Yet,

both cases agree that the strongest U10 feedback is located close to the Niño4 region.

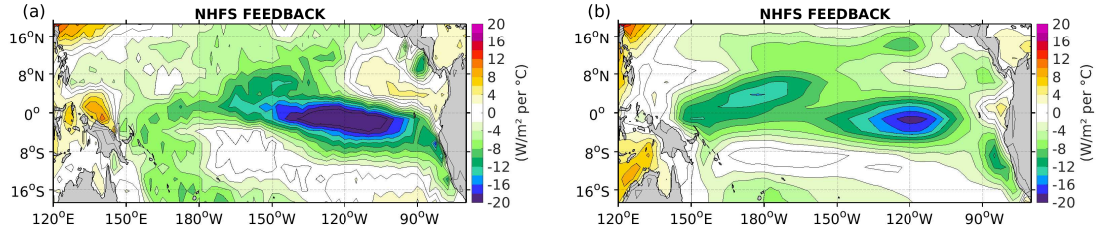


Figure 3.10: Linear net heat flux (NHFS) feedback: anomalous net heat flux (NHFSa) sensitivity to Niño3.4 sea surface temperature anomalies (SSTA) for each tropical Pacific grid point for a) ERA-20C, and b) GFDL-ESM2M

The main negative feedback, the NHFS feedback, is spread over a larger equatorial region (Figure 3.10). The climate model shows substantial differences when comparing it to ERA-20C: it is weaker in magnitude and its maximum is separated in two main domains, one centered at 120°W and the other one at 180°. The combination of Niño3 and Niño4 regions will be considered as the location of the strongest relationship between the NHFSa and the Niño3.4 SSTA.

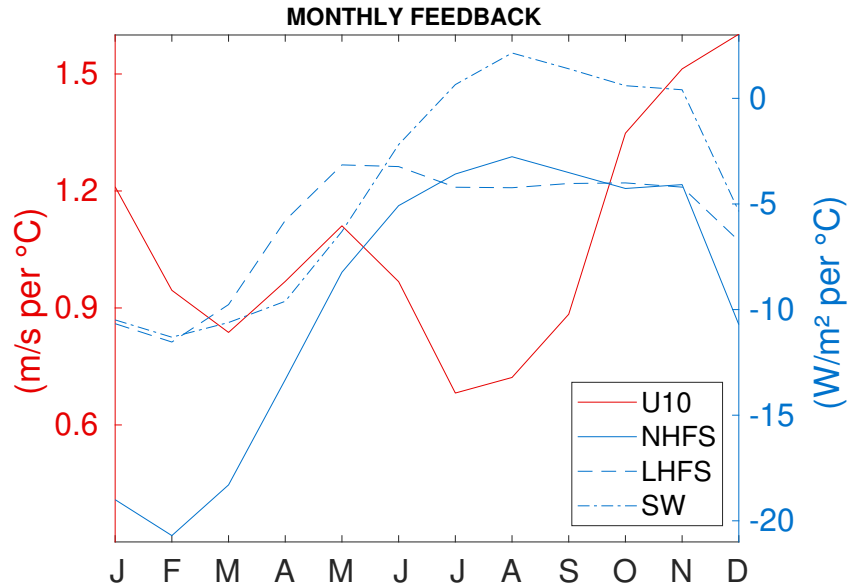


Figure 3.11: Monthly wind (U10) feedback in red and net heat flux (NHFS) feedback in solid blue. The net heat flux feedback has been divided into latent heat flux (LHFS) shown as dashed blue and shortwave radiation (SW) as dash-dot blue. Niño3.4 sea surface temperature anomalies (SSTA) have been linearly related to Niño4 surface zonal wind anomalies, and with the combination of Niño3 and Niño4 for the net heat flux anomalies, as well as for its components.

The seasonality of the feedbacks can be observed in Figure 3.11. The U10 feedback has strongest values from October to December, the season in which the SST varies the most and the ENSO events grow. However, a second peak is visible during May, which could be related to the double ITCZ and relaxation of the easterlies, hence forming a second peak on the ENSO phase locking (Figure 3.7a). The NHFS, as demonstrated by *Lloyd et al.* (2009), is mostly governed by LHFS and SW feedbacks. It peaks from January to April, reducing the variability of the Niño3.4 SST and leading to relatively realistic ENSO phase locking.

From our feedback analysis we could argue that the GFDL-ESM2M climate model has a quite realistic representation of the U10 feedback, although it extends too far into the western equatorial Pacific. However, the model shows larger deficiencies when simulating the negative NHFS feedback: its maximum values are split into two equatorial domains and the absolute values are overall weaker than in ERA-20C. Hence, since the SST variability is over-excited by the positive feedback, mostly in the western equatorial Pacific, but it is too weakly damped by the NHFS feedback, excessively active ENSO events are to be expected.

3.2 Decadal ENSO amplitude

Now that we have looked into the climate model biases and some ENSO characteristics, we would like to examine a relevant ENSO property: the decadal ENSO amplitude change along a 500 year historical run. Since El Niño events are anomalies of sea surface temperatures (SSTA) over the equatorial Pacific, ENSO amplitude is here considered to be the spread of SSTA and computed as the Niño3.4 running standard deviation with a 30 year window.

Considering the length of the run, which is 500 years, the next question that arises is regarding the anomalies: will it be appropriate to subtract the climatological mean of the whole time series, or would it be preferable to compute the seasonal cycle of each 30 year running window? The key for the answer will depend on the time evolution of the climatology: if the mean state of each 30 year window is maintained relatively uniform, then subtracting the climatology of the whole time series would be enough. On the other hand, if the mean state varies considerably, then the anomalies will have to be calculated relative to each 30 year window.

In order to find an answer, the monthly climatology was computed with a 30 year running window over the Niño3.4 region. Next, we obtained the error bars with a 95% of confidence interval, given by the 97.5th percentile for each month, representing the variability of the climatology (Figure 3.12).

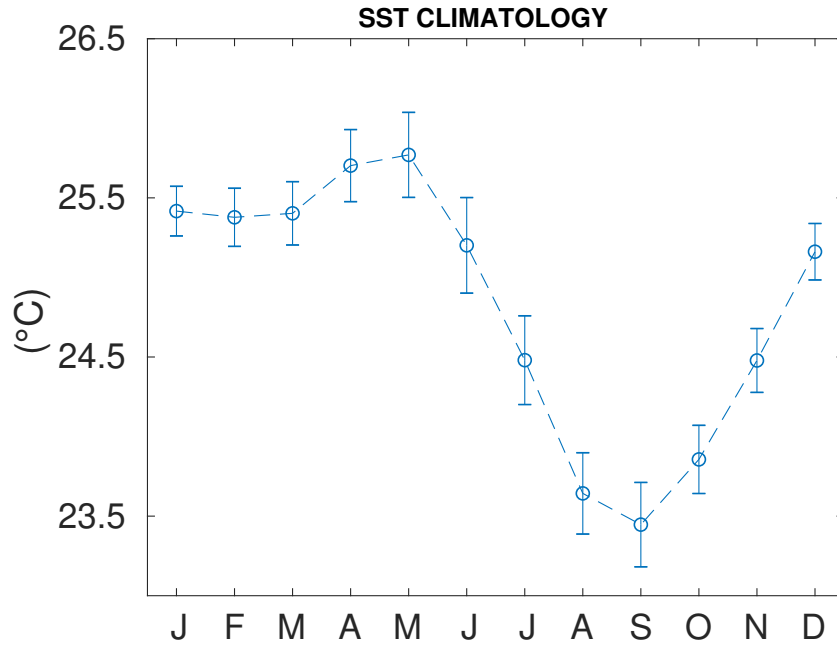


Figure 3.12: Monthly climatology of Niño3.4 sea surface temperature (SST) in GFDL-ESM2M. The error bars show the 95% confidence interval of the 30 year running mean windows.

Although initially, the error bars seem to show relatively small values, in ENSO analysis a difference in the climatology of 0.5°C could lead to notorious differences. Computing the

anomalies relative to a constant climatology, time periods with higher mean temperatures would contain stronger ENSO events, because the variation from a constant mean will be larger. The influence of the mean state variability on the Niño indices with a constant climatology is clearly visible in Figure 3.13.

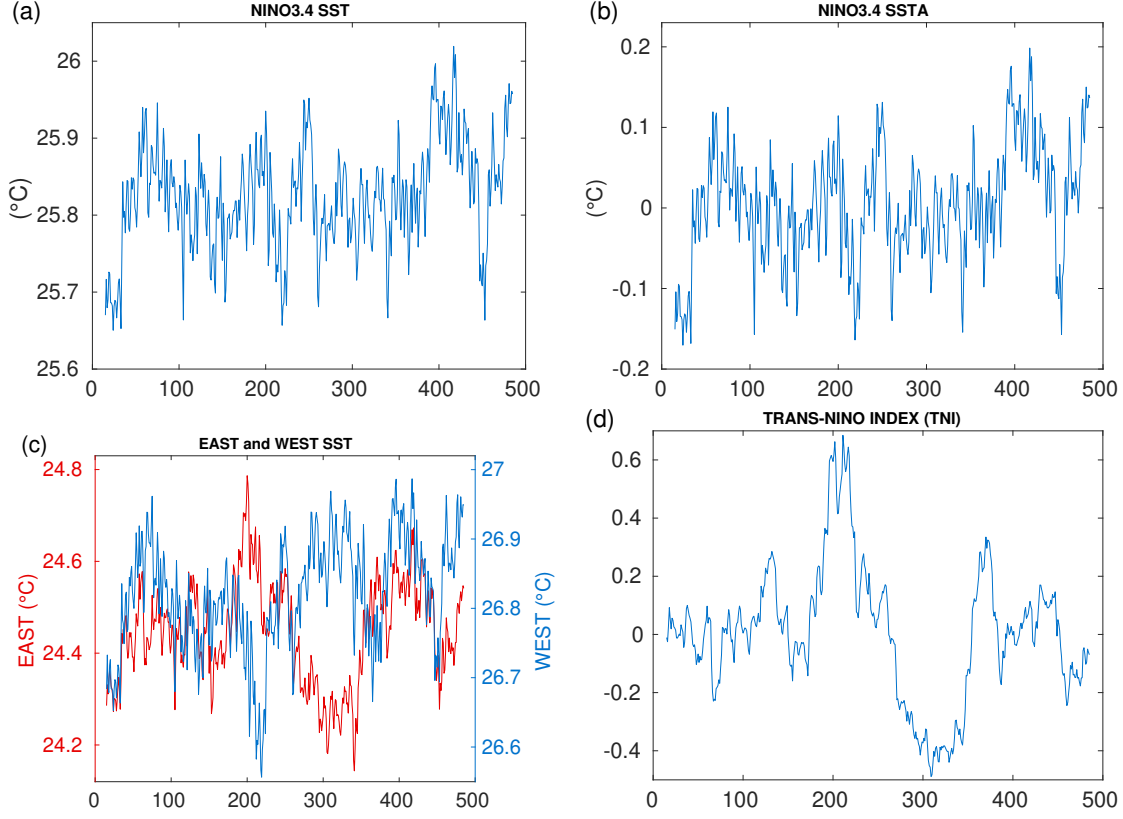


Figure 3.13: Comparison between a) 30 year running window of Niño3.4 sea surface temperatures (SST) and b) 30 year low-passed Niño3.4 sea surface temperature anomalies (SSTA) relative to a constant climatology. c) and d) are similar to a) and b), but in this case we compare the mean values of the eastern (130° W - 90° W, 5° N - 5° S) and western box (170° E - 140° W, 5° N - 5° S) to the modified and low-passed Trans-Niño Index (TNI) relative to a constant climatology.

For instance, starting approximately at year 400, the increase of climatological temperatures leads to a positive peak of Niño3.4 SSTA and to about 60 years of a dominant El Niño mode (Figure 3.13b). However, this doesn't mean that during this period of time ENSO events are stronger, because the general pattern of the index is very similar to the one of the climatological changes (Figure 3.13a). For the TNI, in which we compare the difference of normalized SSTA over the western and eastern equatorial Pacific sections, even stronger differences are visible. East and west equatorial Pacific mean SST have a temporary opposite pattern: between the years 100 and 400, when the mean temperatures are increasing on one side of the equatorial Pacific, they are decreasing on the other side (Figure 3.13c). Using a constant seasonal cycle to compute the SSTA for the TNI, the effect of the climatology on the anomalies is doubled

(Figure 3.13d). In this case the anomalies incorporate the influence of large climatological changes and hence, a strong pattern of high and low peaks is visible. With this method we could not compare, how the system's variability behaves in different mean states, since in the variability the changes in the mean state would be included as well.

From this analysis we can conclude two things. Firstly, in order to compare different periods of ENSO events we must use the climatology of each epoch to analyze the real variations from the mean SST. And secondly, the model shows periods at the very beginning and at the very end of the run in which west and east equatorial Pacific have the same pattern of increasing and decreasing SST means, while from year 100 to 400 we see the opposite behavior.

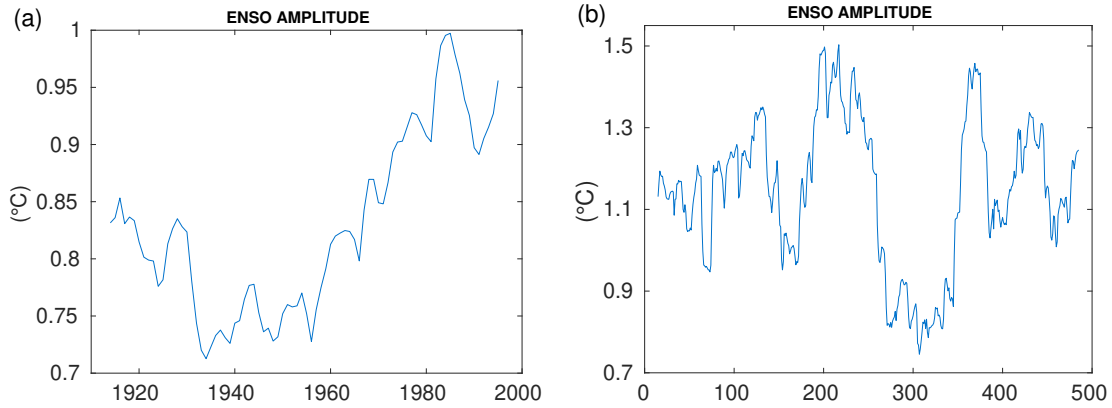


Figure 3.14: The ENSO amplitude computed with a 30 year running standard deviation of Niño3.4 sea surface temperatures (SST) for a) ERA-20c, and b) GFLD-ESM2M.

It is clearly visible that along the 500 year run, ENSO has a decadal oscillation between small and large amplitude periods (Figure 3.14b). Approximately around the year 200 there is a relatively long period of time with high ENSO variability, while the next period of time starting at about year 275 contains roughly 70 more years of very low amplitude. Thus, we can define two main epochs of very different ENSO amplitudes: the high ENSO amplitude period (High epoch) from year 175 to 235 and the low ENSO amplitude period (Low epoch) from year 260 to 320, each time section consisting of 60 years.

Comparing to the ERA-20C reanalysis product, the present climate model has an excessive amplitude variability: the reanalysis values correspond only to the Low epoch (Figure 3.14a).

It appears like there is a relationship between the excessive ENSO amplitude variability and the mean equatorial SST gradient variability (Figure 3.13c). While the mean SST gradient doesn't change, that is, if the east and west equatorial Pacific mean states keep the same pattern of warming or cooling, then the ENSO amplitude has the smallest variability. But if the SST gradient increases (decreases), then we obtain periods of relatively low (high) ENSO amplitudes.

At this point it is important to think about the nature of the ENSO amplitude: either it could be that the high amplitude is due to a few but very strong ENSO events or due to moderate ENSO events with higher frequency of occurrence. Thus, concerning to the previously

arisen question, we have binned the whole time period in 30 year windows with the objective to analyze the ENSO events of different epochs independently .

For the detection of ENSO events we have used the traditional Niño3.4 index explained in the methodology section: calculating the SSTA over the mean Niño3.4 region by subtracting the monthly climatology, and detecting the event when the index exceeds the threshold of half of the standard deviation for at least five consecutive months. In addition, a threshold of a double standard deviation has been used to detect strong ENSO events. Since the threshold is calculated for each bin, it is expected that during the High epoch the threshold will be of larger magnitude and the ENSO events considered will be relatively stronger than in the Low epoch. Furthermore, we have applied a modified TNI suggested by *Trenberth and Stepaniak* (2001) to analyze, if those events are CP or EP type. Using the procedure explained in the methodology section, we have applied modified eastern and western boxes adapted to the anomalous geographical SSTA pattern of the GFDL-ESM2M model: as seen in in the previous subsection the strongest SSTA known as EP type El Niño events are located off the coast of South America and hence its signal won't be detected by the original Niño1+2 region.

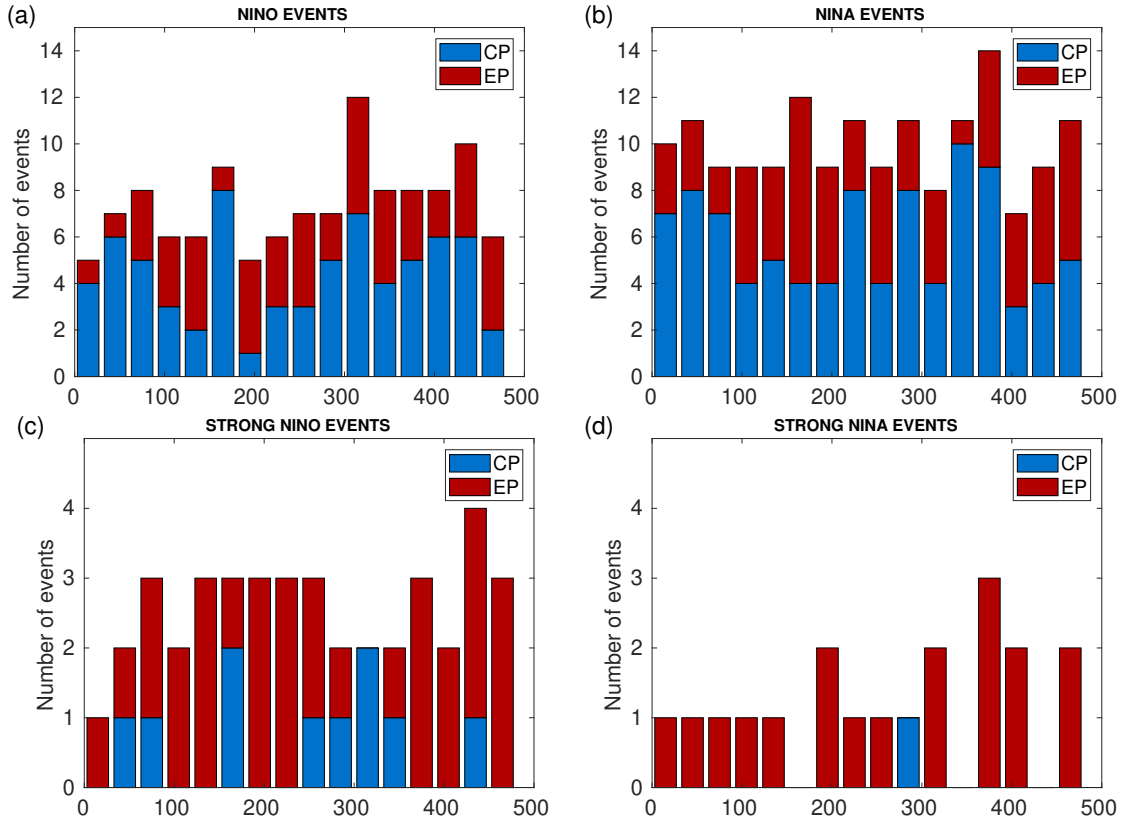


Figure 3.15: Classification of the ENSO events into Central Pacific (CP) and East Pacific (EP) types within 30 year bins. a) El Niño events with a threshold of half a sea surface temperature anomaly (SSTA) standard deviation over the Niño3.4 region, b) La Niña events with a threshold of half a sea surface temperature anomaly (SSTA) standard deviation over the Niño3.4 region. c) and d) are similar to a) and b), but they only consider strong ENSO events exceeding a double standard deviation.

In the Figures 3.15a,b we see the common ENSO events classification divided in 30 year bins, with a threshold of half a standard deviation. Overall, along 500 years we have a higher frequency of La Niña events than El Niño. In addition, El Niño events show a systematic classification related to the decadal ENSO amplitude evolution: during the High epoch we have less common events than during the Low epoch. However, during the first period, more EP Niños occurred, while during the second period the frequency of the CP El Niño events is considerably increased. La Niña events on the other hand have a relatively constant frequency of occurrence with intermittent relevance of CP-EP events.

Instead of considering the ENSO events exceeding half of the SST standard deviation, if we apply a threshold of a double standard deviation to compute the strong El Niño (Figure 3.15c) and La Niña events (Figure 3.15d), in all but one bin La Niña events are detected as EP like. Moreover, La Niña events are fewer than El Niño due to the non-linear effects of the model (as shown by the positive skewness of the SSTA PDF, Figure 3.4b). The High epoch contains more strong El Niño events (being EP type) than the Low epoch with CP events.

In order to gain insight into the higher frequency of common La Niña events, we have analyzed how the system behaves after the El Niño and La Niña events. Figure 3.16 is a Hovmöller diagram of El Niño and La Niña composites. The zero value represents the month of December, with the corresponding next and previous months shown as positive and negative values. It can be seen that in the GFDL-ESM2M model El Niño events are usually followed by La Niña events. However, after La Niña events there are no El Niño events visible, but weaker negative SSTA are shifted eastward, causing a second negative peak with 15 months lag on the eastern equatorial Pacific. Therefore, the higher amount of La Niña events seen in Figure 3.15 is due to the consecutive La Niña events, which might initially be triggered by previous El Niños.

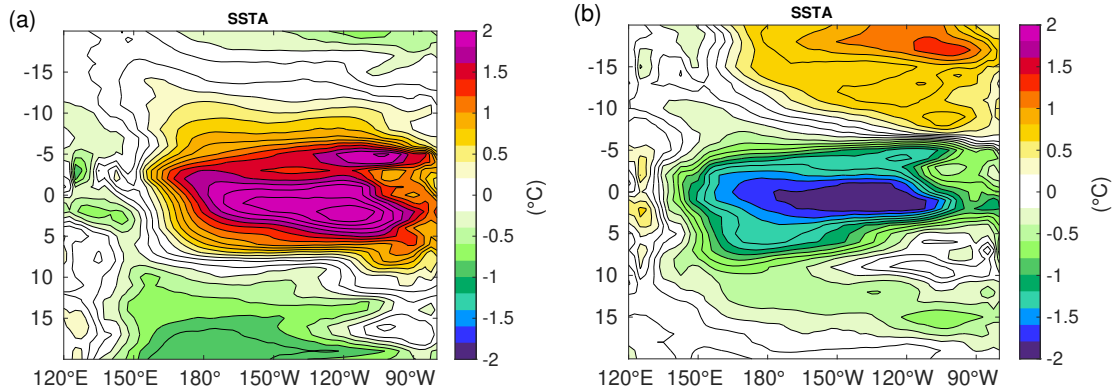


Figure 3.16: Hovmöller diagram of equatorial (5°N - 5°S) sea surface temperature anomaly (SSTA) composites, setting the zero value to December and negative and positive values to the previous or consequent months, respectively, for a) El Niño composite and b) La Niña composite.

To sum up the evolution of the decadal ENSO amplitude variability, we have defined two main epochs of constant high and low ENSO amplitudes. We could say that during the High epoch we have less common El Niño events, but more strong ones with an EP like character,

while during the Low epoch we have more common events, but less strong ones, with more of a CP flavor. At this point we must keep in mind that the GFDL-ESM2M model has difficulties to reproduce realistic EP events, because the SSTA variability is displaced off the American coast. Nevertheless, the modified TNI index is able to give an insight to ENSO type changes. Additionally, we should keep in mind that the threshold applied to each bin is computed relative to its standard deviation, considering the corresponding 30 year window. Hence, during the High epoch, due to a higher SST variability, this threshold will be larger and the detected events will be of relatively larger magnitude.

3.3 High / Low ENSO amplitude periods

So far we have detected large decadal ENSO amplitude oscillations in the GFDL-ESM2M climate model, with two main periods of high and low amplitudes, which are defined as the High and the Low epochs. They differ in ENSO intensity, frequency of occurrence, as well as in the type of events. The High epoch contains more strong ENSO events of mostly EP-like type. On the other hand, the Low epoch shows a higher frequency of weak ENSO events with mostly CP-like character.

The following chapter of this research will be focused on studying the differences of the tropical Pacific mean state, variability, ENSO characteristics and atmospheric feedbacks between the High and Low epochs. The time frames that we will analyze are the next: the high ENSO amplitude period (High epoch) from 175 to 235 year and the low ENSO amplitude period (Low epoch) from 260 to 320, each time window consisting of 60 years.

3.3.1 Tropical Pacific mean state

The first step to differentiate both periods is to analyze their mean state. We would like to address the question of whether there is some relationship between the ENSO characteristics and the Tropical Pacific mean state of the system. We will work with the sea surface temperature (SST), the vertical structure of the subsurface temperatures averaged over 5°N - 5°S (T), the surface zonal winds (U10), the vertical winds at 500 hPa height (W500), the net heat flux (NHFS), the precipitation (PR) and the total cloud cover (CLT). With the output of our analysis we would like to find out, how the Walker Circulation behaves and changes between the different epochs. Thus, along this section the already introduced variables will be averaged over the corresponding 60 years.

During the High epoch the equatorial Pacific SST gradient is reduced by cooling (warming) the west (east) equatorial mean SST (Figures 3.17a,b,c). Since the U10 intensity is dominated by the SST differences between the east-west equatorial Pacific and the corresponding atmospheric pressure differences, zonal winds are reduced at the central equatorial basin (Figures 3.17g,h,i). The mentioned winds are part of the Walker Circulation, which also seems to be overall weakened during the High epoch. Vertical winds are reduced in both directions along the equatorial region, including both the rising branch of the Walker Circulation in the western Pacific and the subsidence region in the central Pacific. In fact, the maximum downward wind velocities shown by the High epoch are restricted to around 100°W , while in the Low epoch the maximum is expanded from 150°W to 90°W , that is, over the Niño3 region (Figures 3.17j,k,l). Related to the Walker Circulation, in the region where the subsidence state is weaker during the High epoch, the cloud cover is larger (Figures 3.17s,t,u), similar to the amount of PR (Figures 3.17p,q,r), and the NHFS is reduced (Figures 3.17m,n,o). Therefore, while the ENSO amplitude is high, the mean state of the Walker Circulation is reduced in intensity. Observing the Low ENSO amplitude epoch, the situation is reversed and the Walker Circulation is strengthened.

An interesting point is that the Low epoch coincides with the a stronger thermocline tilt caused by the strong mean U10 (Figures 3.17d,e,f). During this epoch the heat content is increased over the western equatorial subsurface layers, while the eastern section is cooled leading to a stronger thermocline depth difference.

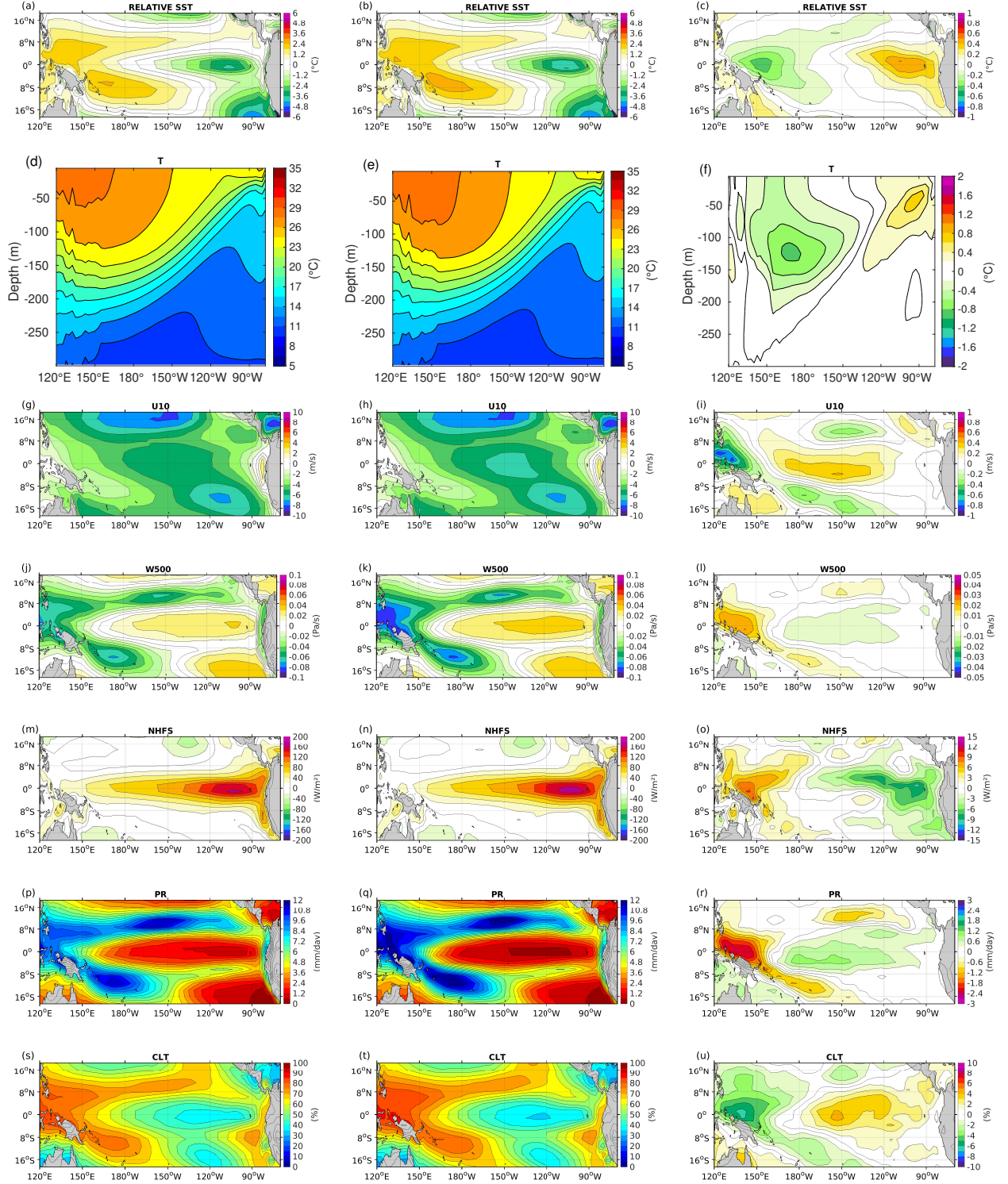


Figure 3.17: Representation of the tropical Pacific mean state during the High and Low epochs as well as their difference: a) High epoch sea surface temperature (SST) relative to the tropical Pacific SST, b) same as a) but for the Low epoch, c) the difference of relative sea surface temperature (SST) between the High and the Low epoch. Following the same structure, d), e), f) correspond to subsurface temperatures (T), g), h), i) to surface zonal winds (U10), j), k), l) to vertical winds at 500 hPa (W500), m), n), o) to the net heat flux (NHFS), p), q), r) to the precipitation (PR) and s), t), u) to the total cloud cover (CLT).

When the thermocline tilt is increased, the ocean-atmospheric coupling is expected to increase as well, hence inducing a higher variability of the SSTA via the U10 feedback (*Atwood et al.*, 2017). If that is so, from our analysis we could say that the mean state of the tropical Pacific's High epoch seems to damp the variability of the SST.

A similar analysis has been done to compare both periods of time, but in this case we have averaged the variables latitudinally around the equator (5°S - 5°N) and plotted them longitudinally (Figure 3.18). We can observe that the main patterns don't shift in longitude: the maximum and minimum values of each variable are maintained at the same longitudinal location. The difference between both periods then is the intensity or the magnitude of the measured variable and not the longitudinal shift. Therefore, between the two periods of the largest decadal ENSO amplitude differences, there is no mean zonal shift of the Walker Circulation.

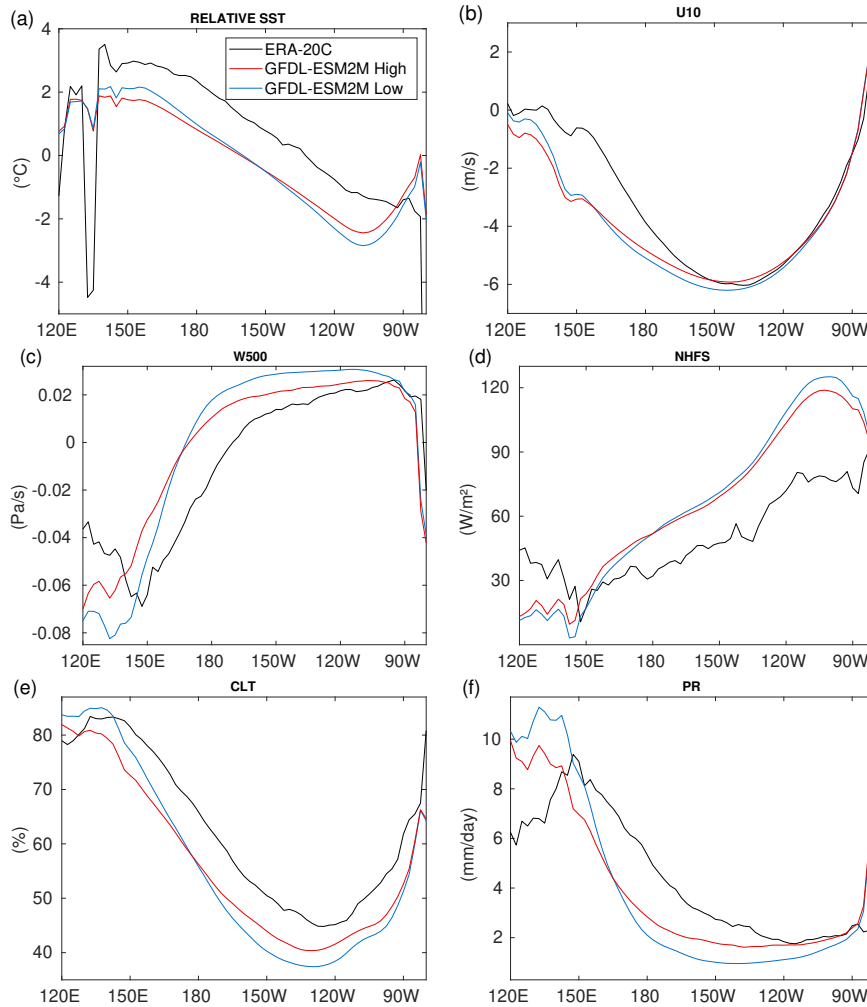


Figure 3.18: Equatorial Pacific mean state (5°N - 5°S) for: a) sea surface temperatures (SST), b) surface zonal winds (U10), c) vertical wind at 500 hPa height (W500), d) net heat flux (NHFS), e) total cloud cover (CLT) and f) precipitation (PR). GFDL-ESM2M's High epoch in red and the Low epoch in blue. The black line represents ERA-20C output.

Comparing with the ERA-20C reanalysis product, we observe the differences already explained in the model bias section: the restricted Pacific Warm Pool over the western equatorial Pacific as well as the westward extension of the east equatorial Pacific cold tongue that reaches approximately 160°W (Figure 3.18a), too strong easterly winds west of 150°W (Figure 3.18b), a westward displaced rising branch of the Walker Circulation and too strong subsidence in the central-east equatorial Pacific (Figure 3.18c), along with too weak CLT (Figure 3.18e) and PR (Figure 3.18f), which leads to an anomalously high NHFS (Figure 3.18d).

Although the overall mean model biases are still large for both periods when comparing them to ERA-20C, the convective and subsidence branches of the Walker Circulation are closer to realistic values during the High epoch. In fact, the zonal gradient of atmospheric variables is increased during the Low epoch. For instance, the absence of any zonal shift of the Walker Circulation combined with a stronger change from an enhanced convective state over the western region to the anomalously higher subsidence domain results in an anomalous zonal gradient. A similar description can be applied to CLT, PR and NHFS.

From the High and Low epoch mean state comparison we have learned that the increase (decrease) of the decadal ENSO amplitude is accompanied by the decrease (increase) of the Walker Circulation intensity without any zonal shift of the convective or subsidence regimes. In addition, although both epochs show a westward displacement of the convective branch of the Walker Circulation and westward extension of the subsidence regime, the zonal gradient as well as the upward and downward winds of the High epoch are closer to our reference values. In fact, the largest subsidence intensity shown by the Low epoch is maintained over the Niño3 region.

3.3.2 Tropical Pacific variability

In the next section we will proceed as for the mean state, but focusing our attention on the variability of the two epochs (Figure 3.19). The variability here will be defined as the standard deviation, subtracting the climatology of the whole period of 60 years. The differences between the epochs are obtained by dividing the High epoch variability by the Low epoch variability.

Looking into the SST, we observe that the highest and the lowest variability is positioned similarly for both periods: in the very east and west equatorial Pacific respectively. However, the major difference between the epochs is located at the central equatorial region centered at 150°W , showing a reduced variability from 180° to 120°W (Figures 3.19a,b,c), similarly as for the U10 (Figures 3.19g,h,i).

Regarding the subsurface temperatures, the largest variability differences are located at 100 m depth, below the largest SST variability differences. In addition, a second region of larger variability differences between the two epochs is observed in the upwelling area in the eastern equatorial Pacific. The greatest thermocline variability differences are observed in the mentioned two domains, as shown by the solid lines in Figures 3.19d,e,f.

The rest of the atmospheric variables have larger variability differences in the central equatorial region too, the largest variability always corresponding to the High epoch. The variability of the W500 and the PR show very large differences, exceeding two times the standard deviation over the Niño3 region (Figures 3.19l,r). In contrast, the CLT and the NHFS variability differences are not that large between the two defined epochs (Figures 3.19o,u).

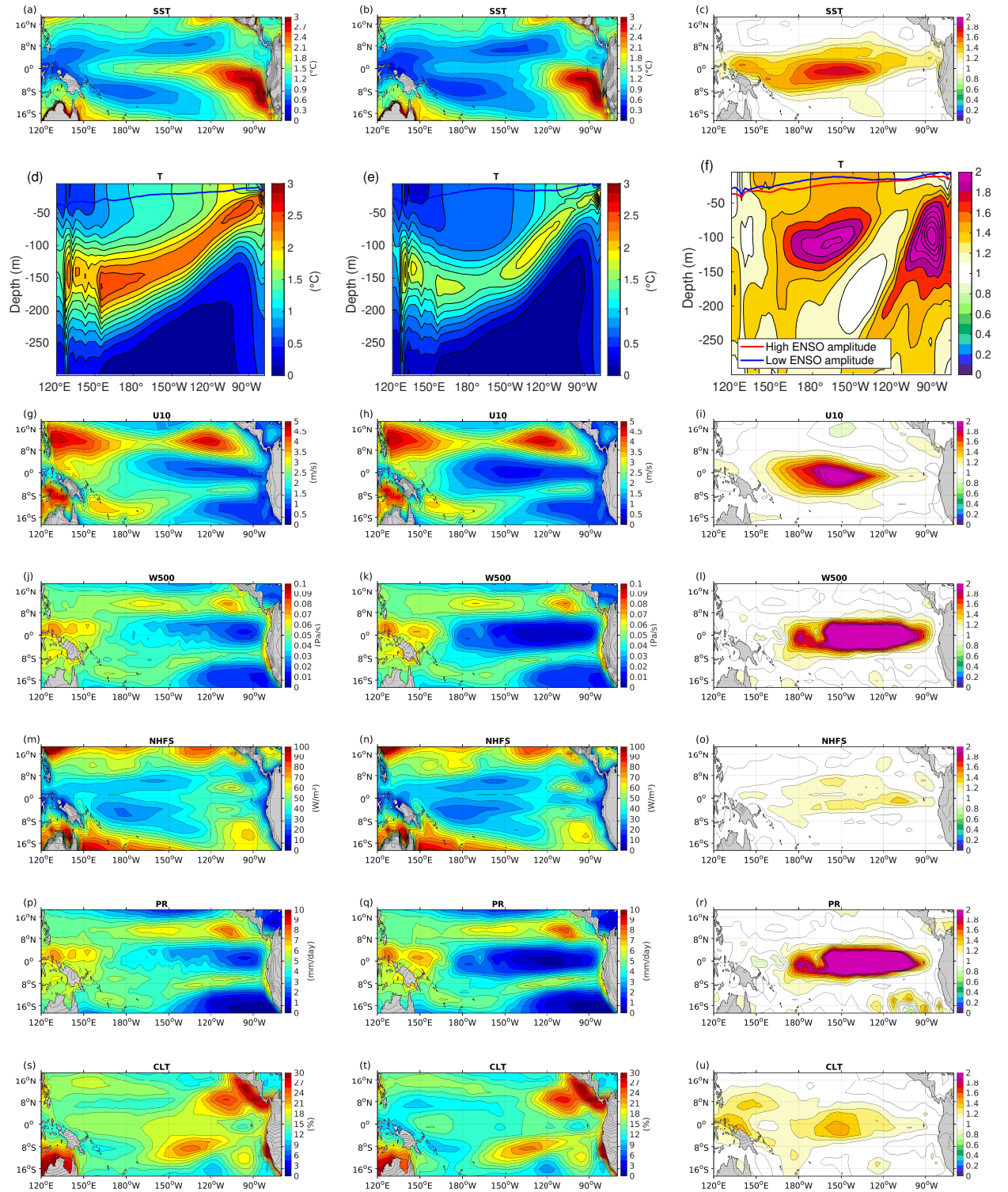


Figure 3.19: Representation of the tropical Pacific variability computed with the standard deviation during the High and Low ENSO amplitude periods as well as their difference: a) High epoch sea surface temperature (SST), b) same as a) but for the Low epoch, c) the variability ratio between the High and the Low epoch. Following the same structure, d), e), f) correspond to the subsurface temperatures (T) with the solid lines representing the thermocline depth variability in meters, g), h), i) to surface zonal winds (U10), j), k), l) to vertical winds at 500 hPa height (W500), m), n), o) to the net heat flux (NHFS), p), q), r) to the precipitation (PR) and s), t), u) to the total cloud cover (CLT).

Hence, we find that during the Low epoch the reduced vertical wind variability over the Niño3 region coincides with the strongest mean subsidence domain. Furthermore, the SST variability, thermocline depth variability and U10 variability are considerably reduced too over the central equatorial Pacific area.

3.3.3 ENSO metrics

In the previous sections we have seen that the High epoch is dominated by strong system variability forming EP like El Niño events, while during the Low epoch the system has less variability, obtaining weaker CP like events. In this section we will try to find more hints related to ENSO statistic dissimilarities between the two main periods of time.

Looking into the probability distributions (PDF) of Niño3.4 SSTA, the skewness of the High epoch is greatly increased, from 0.28 to 0.48 (Figure 3.20). This corresponds to the previously mentioned increase of SST variability and higher frequency of strong El Niño events, showing a higher level of asymmetry. The tails of the PDF are considerably decreased for the Low epoch, fitting our variability description of the SST, showing smaller anomalies. The reason why we have more El Niño events during the Low epoch can be explained with the decrease of SST variability: since the threshold for ENSO events is computed as half of the standard deviation of each 30 year bin, when the SST variability is reduced, the threshold is reduced as well and the probability of obtaining a common El Niño event is increased. Hence, we have been computing relatively weak El Niño events, which are closer to the mode of the PDF during the Low epoch.

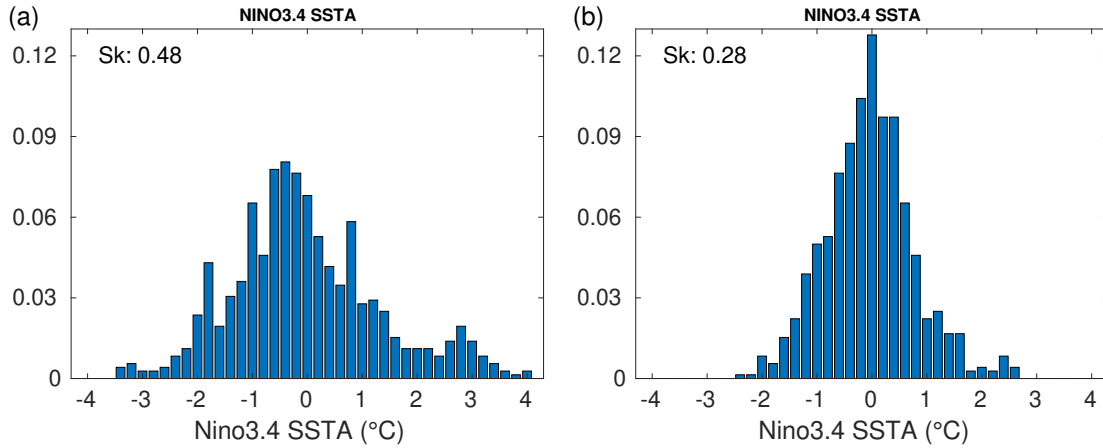


Figure 3.20: Probability density function of Niño3.4 sea surface temperature anomalies. The skewness value, representing the ENSO asymmetry is displayed on the upper left corner of the plots for a) the High epoch, and b) the Low epoch

The spatial distribution of the SSTA skewness (Figure 3.21) also shows stronger values in the eastern equatorial basin for the High epoch, a signal of EP-like El Niño events. On the other hand, during the Low epoch the strongest positive skewness is located in the south-central equatorial Pacific, a signal of CP-like El Niño events. In relative terms, the positive skewness values for the Low epoch are greatly reduced compared to the High epoch.

The skewness of the U10A doesn't show large differences regarding the maximum values (Figure 3.22). However, during the Low epoch the maximum values are confined to the western side of 150°W, while during the High epoch relatively strong positive skewness values reach 120°W. Therefore, during the High epoch the anomalous westerly winds that are related to the El Niño events are felt further west, which they seem to be reduced between 150°W and 120°W during the Low epoch.

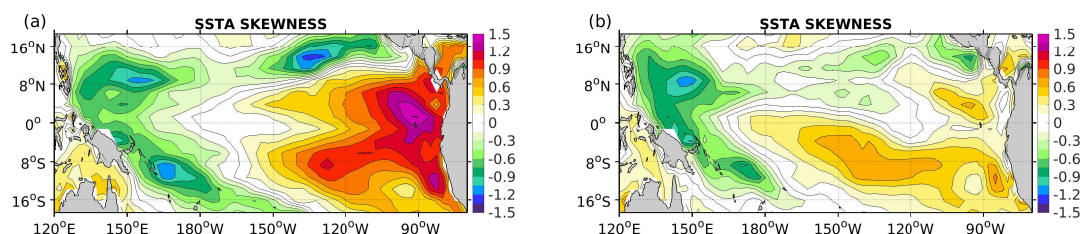


Figure 3.21: Skewness map of tropical Pacific sea surface temperature anomalies (SSTA) for a) the High epoch, and b) the Low epoch.

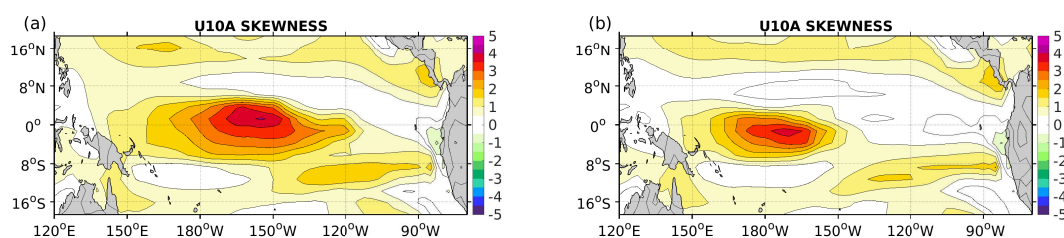


Figure 3.22: Skewness map of tropical Pacific surface zonal wind anomalies (U10A) for a) the High epoch, and b) the Low epoch.

According to Figure 3.23a), the phase locking of the ENSO events is deteriorated during the Low epoch. Although the variability of the monthly standard deviation of Niño3.4 SST is within the bounds of realistic values in reference to the ERA-20C reanalysis product (Figure 3.7), the dominant peak of SST variability is unrealistically during July. This could mean that the realistic seasonal southward displacement of the ITCZ captured by observations is not fully represented during the Low epoch, leading to the wrong ENSO event representation, simulating anomalous ENSO events peaking during the boreal summer. On the other hand, for the High epoch the ENSO phase locking seems to be realistically simulated, showing a maximum SST variability during boreal winter months. Nevertheless its general variability is unrealistically high. Furthermore, the summer peak shown by the Low epoch is still present during the High epoch, as demonstrated in Figure 3.23b: the mentioned unrealistic summer month SST variability is hidden by the large year-round SST variability east of 140°W.

Similarly as in Figure 3.16, in Figure 3.24 the composites of El Niño and La Niña events are analyzed for both selected periods. The Hovmöller diagrams are centered at time 0, correspon-

ding to the month of December, and the previous and consecutive months are shown by negative and positive numbers. 12 months after an El Niño event the system fluctuates into a La Niña state during the High epoch, as shown by the composite analysis (Figure 3.24a). For the Low epoch on the other hand, one year after an El Niño event a weaker positive SSTA follows in the eastern equatorial Pacific region (Figure 3.24b). La Niña events are generally formed following relatively strong positive SSTA in the eastern equatorial Pacific during the High epoch (Figure 3.24c), while in the Low epoch weaker La Niña events are simulated without any previous El Niño event (Figure 3.24d).

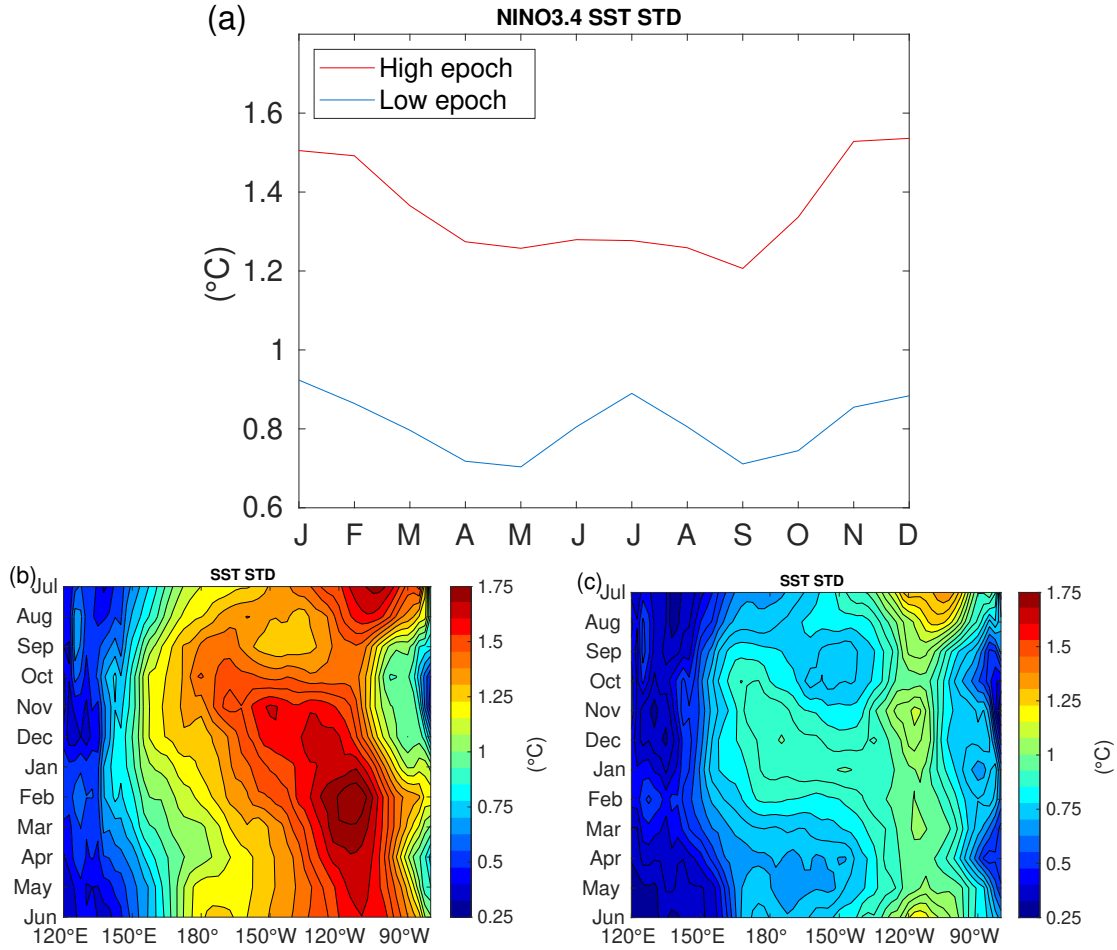


Figure 3.23: Monthly standard deviation of the sea surface temperatures (SST) over: a) the Niño3.4 region, the High epoch in red and the Low epoch in blue, b) the Pacific equatorial (5°N-5°S) region for the High epoch, and c) the same as b) but for the Low epoch.

The geographical pattern and strength of El Niño and La Niña SSTA composites also show differences between the two analyzed epochs (Figure 3.25). For the El Niño composites the SSTA signal is stronger in the east equatorial side for the High epoch (Figure 3.25a), while during the Low epoch the variability is increased in the western side (Figures 3.25d,g). Although the GFDL-ESM2M model is not capable of reproducing realistic EP El Niño events,

the geographical change from east to west of SSTA is still captured by the modified TNI index as we have already seen in Figure 3.15. The La Niña composite shows large SSTAs in the central equatorial Pacific during the High epoch (Figure 3.25b), while during the Low epoch the maximum SSTAs are shifted to 120°E (Figure 3.25e). The difference between the El Niño and La Niña SSTA composites have negative values over the very western equatorial Pacific region during both periods. Nevertheless, the stronger eastern positive SSTA shown by the High epoch leads to a relatively strong positive residual in the east tropical Pacific (Figure 3.25c). Due to the more central-western positive SSTA values of the Low epoch, the positive residual is shifted towards the central-western equatorial region, reaching the date line (Figure 3.25f).

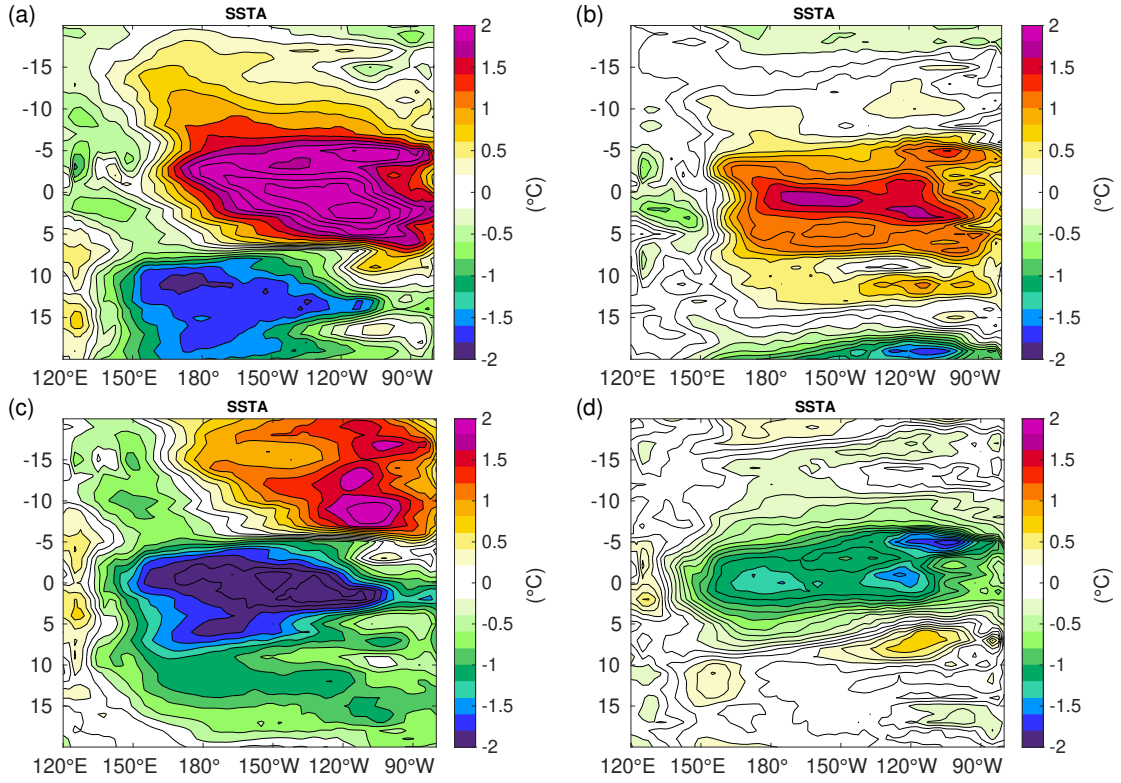


Figure 3.24: Hovmöller diagram of equatorial (5°N-5°S) sea surface temperature anomaly (SSTA) composites setting the zero value to December and negative and positive values to the previous or consequent months, respectively, for a) the El Niño composite during the High epoch, b) the El Niño composite during the Low epoch, c) the La Niña composite during the High epoch, d) the La Niña composite during the Low epoch.

Summarizing the main ENSO characteristics, the High epoch simulates stronger ENSO asymmetry with larger positive SSTA skewness in the eastern equatorial region and the effects of the anomalous westerly winds are felt up to 120°W. The Niño3.4 SST variability peaks during boreal winter and the geographical pattern of El Niño events shows the strongest SSTA centered at 120°W, causing EP-like ENSO events. La Niña events' SSTA is observed in the

central-western equatorial Pacific, leading to a residual of positive east, and negative west equatorial SSTA.

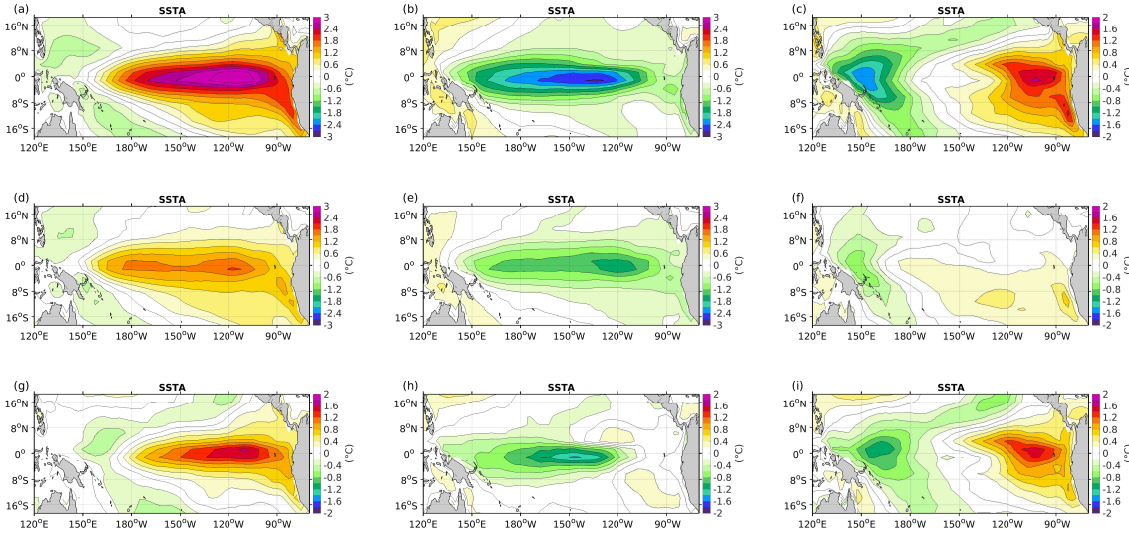


Figure 3.25: Geographical location of the tropical Pacific sea surface temperature anomalies (SSTA) for the High epoch, the Low epoch, as well as their difference: a) the El Niño composite during the High epoch, b) the La Niña composite during the High epoch, and c) their residual obtained by adding both composites. Similarly, d), e), and f) correspond to the Low epoch and g), h), and i) to the difference between the two epochs.

The Low epoch ENSO events could unrealistically occur during boreal summer due to the peak of Niño3.4 SST variability of July. The anomalous weak easterly winds are suppressed between 150°W and 120°W, in the region of the strongest mean subsidence. The El Niño SSTAs are extended further west, while La Niña SSTA are displaced east to 120°W and their positive SSTA residual are observed up to 180°. The difference of El Niño and La Niña residuals between both epochs, together with the differences in ENSO asymmetry could have diverse effects on the mean state.

3.3.4 Atmospheric feedbacks

The last comparison between the two epochs will be for the seasonal changes of the main positive and negative feedbacks: the U10 and the NHFS feedbacks. In addition, the NHFS will be divided into the two most relevant components: the LHFS and SW feedbacks (*Lloyd et al.*, 2009, 2012).

We can see that overall both positive and negative feedback are greatly increased during the High epoch (Figure 3.26). This shouldn't be a surprise, since larger positive U10 feedbacks are expected to act on the increase of SST variability. The large increase of the U10 feedback during the boreal winter months (Figure 3.26d) and the LHFS feedback during the boreal spring (Figure 3.26b) keeps the ENSO phase locking fairly correct during the High epoch.

On the other hand, when the ENSO amplitude is small, the boreal winter U10 feedback peak is close in magnitude to the second peak occurring in May (Figure 3.26d). In addition, the SW feedback, instead of acting damping on the Niño3.4 SST variability, is switched to a positive feedback from July until November (Figure 3.26c). The positive peak, which is during July and August, leaves the NHFS feedback without any SSTA damping effect during July, leading to an unrealistic ENSO phase locking (Figure 3.26a).

Hence, we could suggest that during boreal winter of the High epoch, the U10 anomalies of the Niño4 domain are more sensitive to Niño3.4 SSTA than in the Low epoch, forming a stronger positive feedback and leading to an increment of SST variability, as well as to a realistic ENSO phase locking. The unrealistic ENSO phase locking of the Low epoch is related to the weakening of the boreal winter U10 feedback and the SW radiation switch into a positive feedback from July until November.

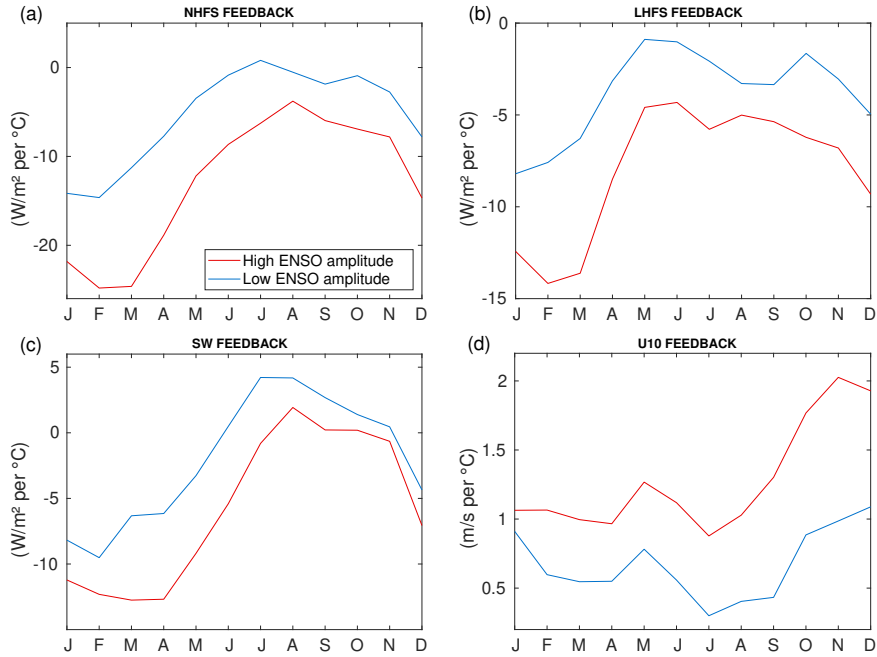


Figure 3.26: Monthly atmospheric feedbacks for the High epoch in red and the Low epoch in blue. The Niño 3.4 sea surface temperature anomalies (SSTA) have been linearly related to a) the net heat flux anomalies (NHFS) over the Niño3 and Niño4 regions, b) latent heat flux anomalies (LHFS) over the Niño3 and Niño4 regions, c) shortwave radiation anomalies (SWA) over the Niño3 and Niño4 regions, and d) surface zonal wind anomalies (U10A) over the Niño4 region.

3.4 Decadal ENSO amplitude modulation

In this last section we will try to find out plausible causes for the ENSO amplitude evolution. So far, we have seen that the U10 feedback strength is increased during the High epoch, while during the Low epoch the wind anomaly sensitivity to the SSTA is decreased. In fact, the relation between the time evolution of the U10 feedback and the ENSO amplitude is highly correlated with a coefficient of 0.95 (Figure 3.27b). It is expected that in order to obtain large amplitudes of ENSO, that is, strong Niño3.4 SSTAs, the U10 feedback must be strong as well, as shown also by the ERA-20C reanalysis product (Figure 3.27a).

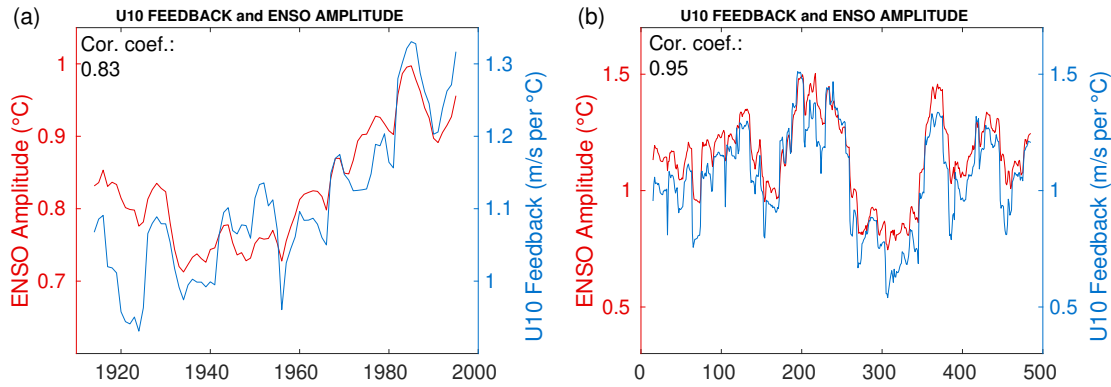


Figure 3.27: Linear correlation between the low-passed wind (U10) feedback and the ENSO amplitude for a) ERA-20C, and b) GFDL-ESM2M. The correlation coefficients are displayed on the upper left corner of the figures.

One of the hypotheses for the U10 feedback intensification relies on the Niño4 SST mean state (*Bayr and Dommenges, 2013*): when the mean Niño4 SST is increased and the cold equatorial bias is reduced, the convective response is increased and hence the U10 feedback and the ENSO amplitude will increase. Nevertheless, the relation between the U10 feedback and the mean Niño4 SST is inversely correlated in the GFDL-ESM2M model with a coefficient of -0.62 (Figure 3.28b). Meanwhile, the mean Niño3 SST and the U10 feedback are highly correlated with a positive coefficient of 0.9 (Figure 3.28a). Thus, the wind sensitivity to Niño3.4 SSTA changes is increased, when the mean SST is increased over the Niño3 domain instead of initially hypothesized Niño4 area.

During our feedback analysis we have been assuming a linear relationship between the Niño3.4 SSTA and the U10A. Since the present climate model is known for its strong non-linearities as demonstrated by the ENSO asymmetry analysis (Figures 3.4 and 3.20), next we will focus on the non-linear behavior of the wind anomalies, when the SSTAs are positive or negative (Figure 3.29). Applying a simple linear regression for positive and negative Niño3.4 SSTAs independently, the solid lines represent the relationship between temperature anomalies and U10A, avoiding the offset of the linear regression for a better comparison of the slope.

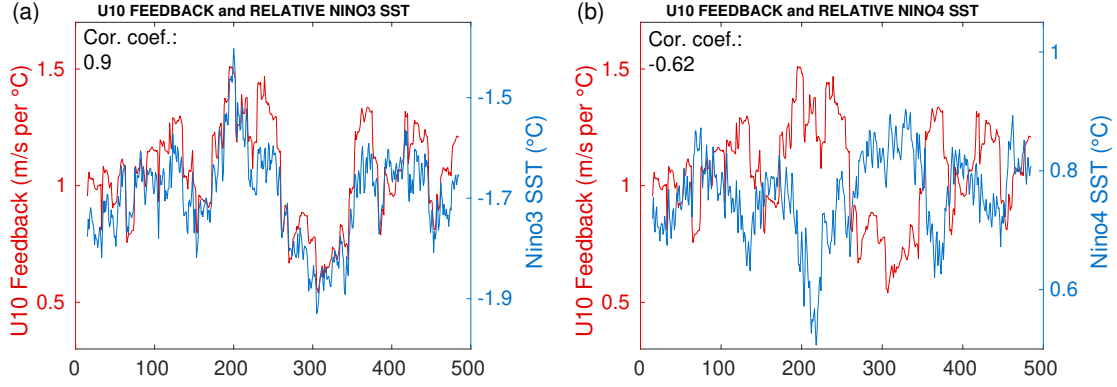


Figure 3.28: Linear correlation between the wind ($U10$) feedback and a) the low-passed mean Niño3 sea surface temperature (SST) relative to the tropical Pacific, and b) the low-passed mean Niño4 sea surface temperature (SST) relative to the tropical Pacific. The correlation coefficients are displayed on the upper left corner of the figures.

The reanalysis product shows a relatively linear positive relation (Figure 3.29a). Although the $U10$ response to Niño3.4 SSTAs is slightly increased when accounting for positive anomalies, the negative anomalies' influence on the $U10$ is still maintained, obtaining a close approximation to a linear feedback. In contrast, the non-linearities are greatly increased for the coupled climate model (Figure 3.29b). While the positive SSTAs show a great wind response, during La Niña events the wind anomalies remain insensitive.

After splitting the anomaly relationship into the two main epochs, the High epoch shows a much stronger slope when accounting for the positive SSTAs (Figure 3.29c). In fact, the $U10$ feedback is closer to being linear during the Low epoch. Looking into the outliers, four months of the Low epoch clearly seem to be the most sensitive to positive SSTAs. Nevertheless, those four months lack of representability during the 60 years of the Low epoch. For the negative SSTAs, during the both epochs the $U10$ feedback remains similarly inoperative.

From Figure 3.29c one could argue that the more linear behavior of the $U10$ feedback during the Low epoch is due to a smaller SST variability, that is, that the Niño4 wind anomalies remain less sensitive, because of the absence of strong positive SSTAs. In the presence of a large amount of very weak positive SSTAs that have a small wind response during the Low epoch, the slope is considerably flattened.

Therefore, our attention will be redirected to the convective response of the system instead of the zonal winds. In order to gain understanding on the ENSO amplitude evolution, we will focus on one of the main components of the negative NHFS feedback following *Lloyd et al.* (2009): the SW feedback. In the paper of *Bellenger et al.* (2014), using observational data they demonstrate the highly non-linear behavior of the SW feedback.

The negative SSTA over the Niño3 region locally enhances the subsidence regime, preventing the formation of stratiform boundary layer clouds, which leads to more incoming radiation, forming a positive feedback, while the switch into a convective regime linked to the positive SSTA increases the cloud cover and the reflection of the radiation: the SW feedback is reversed to a negative feedback (*Philander et al.*, 1996; *Xie*, 2004). Accordingly, the sign of the SW feedback will provide us the information related to the ability of the model to switch from the

subsidence to convective states (*Bellenger et al.*, 2014).

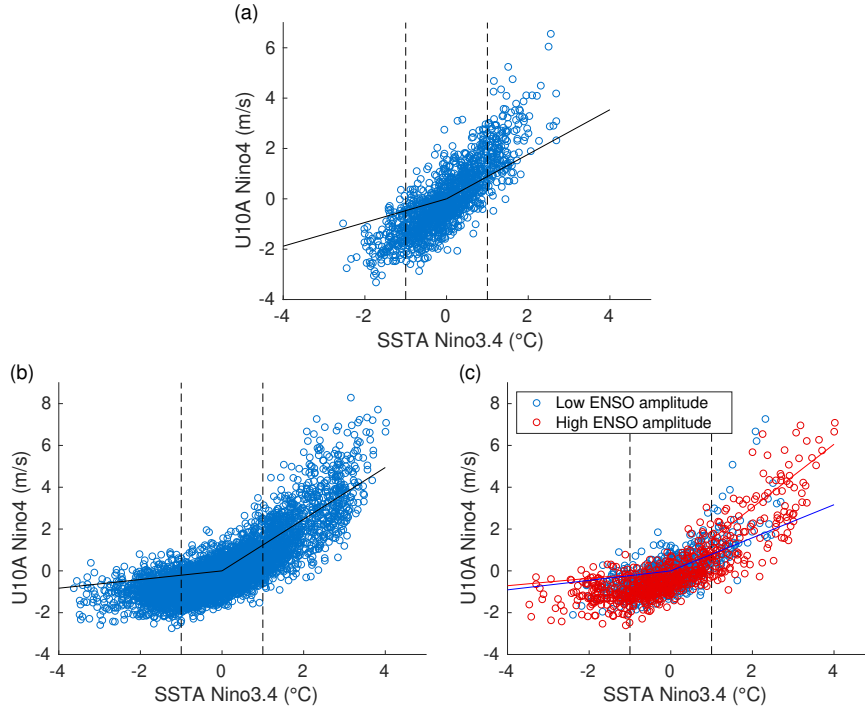


Figure 3.29: Non-linear relationship between the Niño3.4 sea surface temperature anomalies (SSTA) and the surface zonal wind anomalies (U10A) over Niño4. The solid lines represent the slope of the linear relation when positive and negative SSTA are divided without their corresponding offsets. Each dot represents individual months. a) ERA-20C reanalysis product, b) same as a) but for the GFDL-ESM2M model, and c) same as b) but dividing the High and Low epochs in red and blue, respectively.

Our results prove that the GFDL-ESM2M climate model has a realistic SW feedback non-linearity, capturing both the positive and negative signs for La Niña and El Niño composites respectively (Figure 3.30). If the negative SW feedback is a representation of the convective response of the system during El Niño events, we can observe that the mentioned shift to upwards winds extends from 180° to 120°W during the High epoch (Figure 3.30c), while during the Low epoch the convective response is reduced between 160°W and 120°W (Figure 3.30e). Still, the negative feedback values are strong over the Niño4 region, explaining why the U10 feedback could still be relatively sensitive to Niño3.4 SSTAs during the Low epoch.

In order to observe the regions, in which El Niño and La Niña events affect the SW radiation anomaly the most, for the non-linear analysis we will set a domain between 180° - 120°W and 5°N - 5°S. On the other hand, following the SW non-linear analysis applied to the reanalysis products in *Bellenger et al.* (2014), ERA-20C SWA are defined into the Niño3 domain (Figure 3.31). Surprisingly the ERA-20C reanalysis product simulates an unrealistic SW feedback (Figure 3.31a): the sign of the feedback is negative for both the positive and the negative SSTAs. The GFDL-ESM2M model, however, reproduces realistic positive and negative slopes

(Figure 3.31b). Moreover, the strength of the feedback is increased during the High epoch, having the greatest differences between the epochs when the SSTAs are positive (Figure 3.31c).

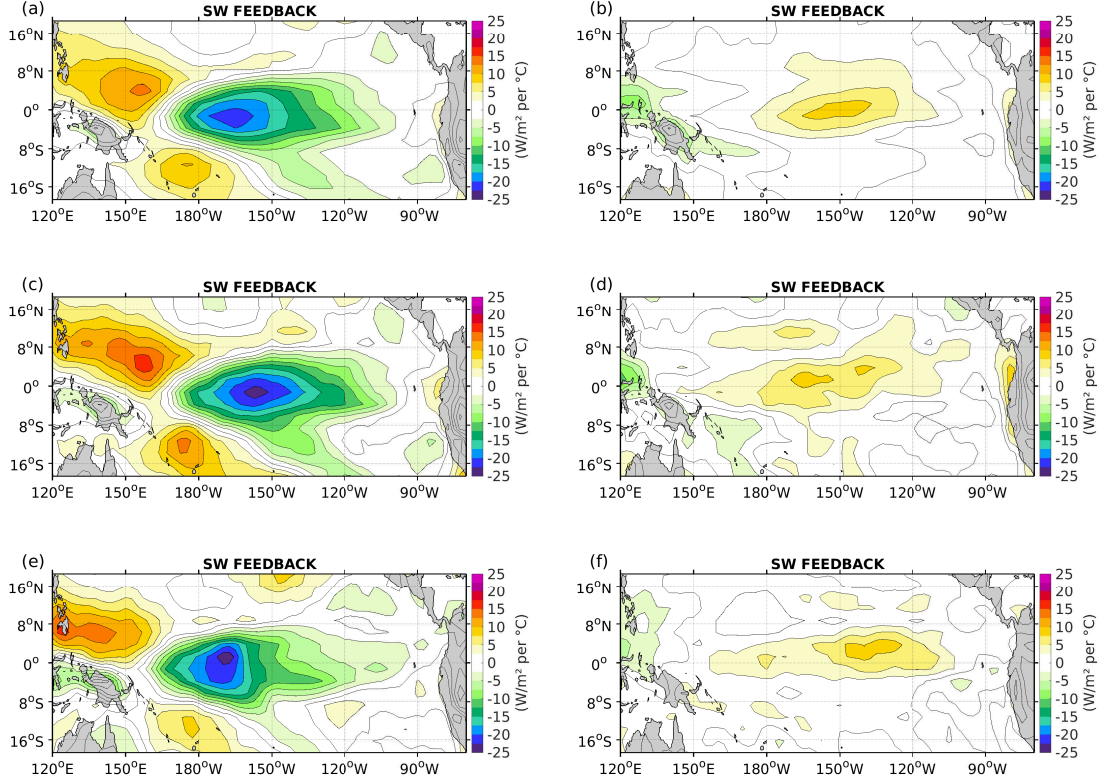


Figure 3.30: Tropical Pacific representation of the shortwave radiation (SW) feedback computed as the linear regression between the Niño3.4 sea surface temperature anomalies (SSTA) and the shortwave radiation anomalies (SWA) for each spatial grid point for a) the El Niño composite for the whole time series, b) the La Niña composite for the whole time series, c) same as a) but for the High epoch, d) same as b) but for the High epoch, e) same as a) but for the Low epoch, and f) same as b) but for the Low epoch.

In the previously presented variability analysis of the High and Low epochs we have detected that the SST variability difference is strongest in the central equatorial Pacific, very close to the area in which the mean state of the W500 differ the most. If the maximum mean subsidence values of the Low epoch, located in the Niño3 region, are too strong to allow a convective switch, shown by Figure 3.30e, we could speculate that the incapability of the system to switch into a convective regime restricts the Niño3.4 SST variability. Although the SW feedback sign has been used as a reference of the convective-subsidence atmospheric shift, in reality the weakening of the SW feedback over the Niño3 region could have multiple sources: the large-scale circulation changes representing the mentioned convective shift, the cloud response to dynamics and the effectiveness of the clouds to reflect back the SW radiation (Lloyd *et al.*, 2012).

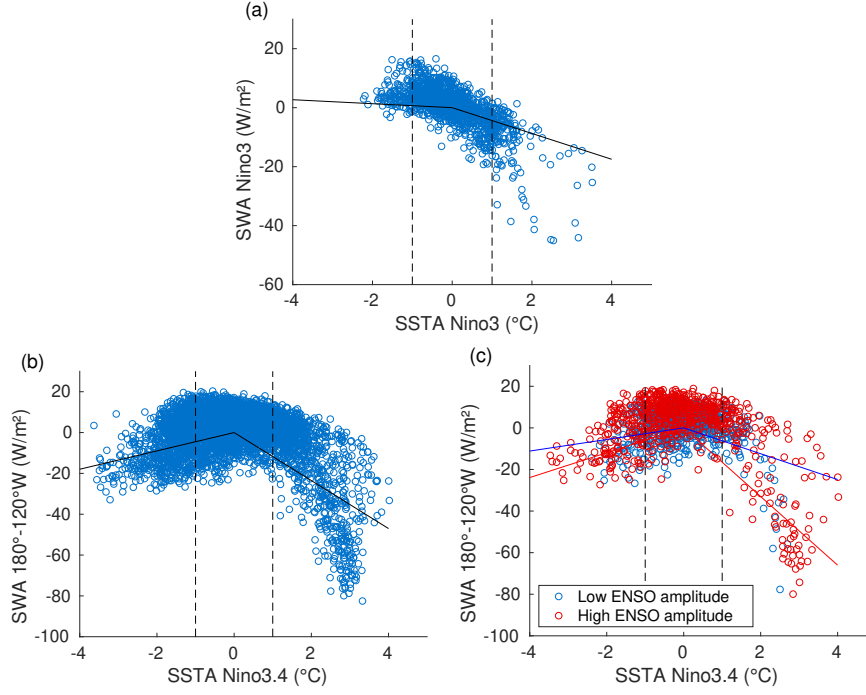


Figure 3.31: Non-linear relationship between the Niño3.4 sea surface temperature anomalies (SSTA) and the shortwave radiation anomalies (SWA). The solid lines represent the slope of the linear relation, when positive and negative SSTA are divided without their corresponding offsets. Each dot represents individual months. a) ERA-20C reanalysis product using the Niño3 box for SWA, b) same as a) but for the GFDL-ESM2M model using the box set to 180°- 120°W, 5°N - 5°S for SWA, and c) same as b) but dividing the High and Low epochs in red and blue, respectively.

For this reason we have proceeded to evaluate, whether the weakening of the SW feedback over the Niño3 area is in fact altered by the large-scale circulation changes during the Low epoch. As presented in Figure 3.32, the vertical wind response is greatly increased for the positive SSTA compared to the negative anomalies in ERA-20C and the GFDL-ESM2M model (Figure 3.32a,b). Yet, the convective response to positive SSTAs is completely damped during the Low epoch, while the High epoch is characterized by a strong SSTA influence on anomalous W500 (Figure 3.32c). Thus, the weakening of the negative SW feedback can be attributed to the reduced sensitivity of vertical wind anomalies.

In the paper of *Hu et al.* (2013), the weakening of the interannual variability in the tropical Pacific Ocean is associated with the changes in the mean state. In their paper it is stated that the ENSO amplitude is increased, when the mean thermocline slope is increased, but too weak or too strong thermocline tilt hampers the SSTA oscillations.

In order to add further veracity to our hypothesis that too strong subsidence winds over the Niño3 region, linked to the intensification of the Walker Circulation and the consequent stronger tilt of the thermocline, damps the ENSO amplitude, we have followed the methodology of *Hu et al.* (2013). For the thermocline slope calculation we have adjusted the western and eastern boxes to the present model: 160°E - 170°W and 120°W - 90°W, respectively. The thermocline depth is computed as the depth of strongest vertical temperature gradient, and

the thermocline tilt by subtracting west and east thermocline depths. Then, the time evolution of the mean thermocline tilt, determined as a 30 year running mean, is compared with the ENSO amplitude.

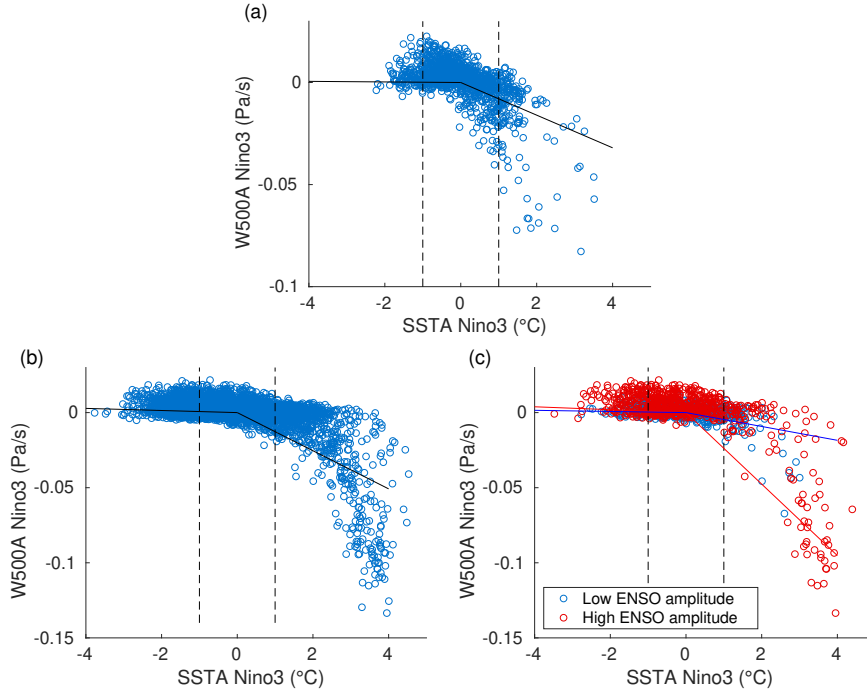


Figure 3.32: Non-linear relationship between the Niño3.4 sea surface temperature anomalies (SSTA) and the vertical wind anomalies at 500 hPa height (W500A) over Niño3. The solid lines represent the slope of the linear relation, when positive and negative SSTA are divided without their corresponding offsets. Each dot represents individual months. a) ERA-20C reanalysis product, b) same as a) but for the GFDL-ESM2M model, and c) same as b) but dividing the High and Low epochs in red and blue, respectively.

The result shown in Figure 3.33 clearly resembles the negative relationship between the analyzed variables: when the mean thermocline slope is increased the decadal ENSO amplitude is linearly decreased. According to the model experiment undertaken by *Hu et al.* (2013), a negative linear relationship between the ENSO amplitude and the thermocline slope occurs, when the thermocline tilt and the mean easterly winds are too strong. Therefore, our hypothesis that the too energetic Walker Circulation and subsidence winds over the Niño3 area hampers the ENSO amplitude, agrees with their findings.

Along the present chapter we have seen that the linear U10 feedback and the decadal ENSO amplitude evolution are tightly linked. Nevertheless, the Low epoch's U10 sensitivity to positive Niño3.4 SSTA is not as small as shown by the linear feedback analysis. In fact, the negative SW feedback, which represents the convective response to positive SSTAs, is maintained relatively high over the Niño4 area, and hence, it is logical to expect some U10 response to anomalous SST. Nevertheless, the negative SW feedback is considerably reduced over the Niño3 domain during the Low epoch, which we have attributed to the weak convective response to a positive

Niño3.4 SSTA increment and to the strong mean subsidence state, which restricts the variability of the SST. The result leads to blame, at least to some extent, the too energetic mean Walker Circulation for the weak decadal ENSO amplitude shown by the Low epoch.

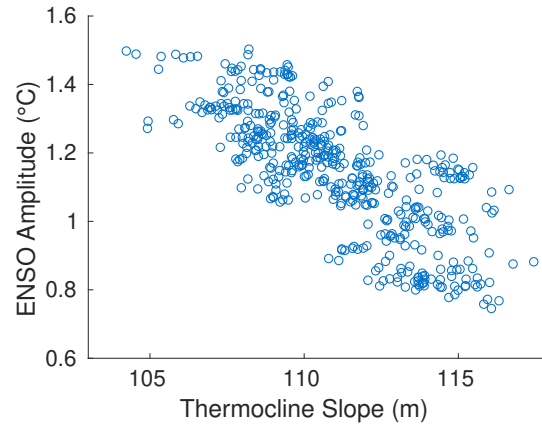


Figure 3.33: *Relation between the decadal ENSO amplitude, computed as a 30 year running sea surface temperature (SST) standard deviation, and the 30 year low-passed thermocline slope calculated as the thermocline depth difference between the eastern (120°W - 90°W, 5°N - 5°S) and western (160°E - 170°W, 5°N - 5°S) equatorial Pacific. The thermocline depth is detected as the depth of strongest vertical temperature gradient. Each dot represents a 30 year window value.*

Chapter 4

Summary, Discussion and Conclusion

In the present chapter we will proceed with the summary, discussion and conclusions lead from the analysis of the coupled GFDL-ESM2M climate model's pre-industrial control run.

4.1 Summary

A 500 year pre-industrial control run of the GFDL-ESM2M coupled climate model has been studied to analyze the decadal ENSO variability. In order to have a realistic reference and compare it with the model output, the data from the ERA-20C reanalysis product has been used, which consists of 110 years from 1900 to 2010.

Initially we have been focused on the capability of the model to represent the tropical Pacific mean state and the ENSO characteristics. The model has quite a realistic representation of relevant ENSO properties, even though it has common problems like many climate models. The model exhibits a cold mean equatorial SST bias over the tropical Pacific exceeding 1°C and a maximum bias reaching 2°C between 120°W and 90°W . A strong positive SST bias of over 3°C is also visible along the South American continent. The maximum cold bias over the eastern equatorial Pacific shifts the zonal SST gradient, leading to an anomalously strong mean easterly winds west of 150°W and restricting the eastward extension of the Pacific Warm Pool west of the date line (180°). The geographical location of the Walker Circulation is also displaced: the convection regime is shifted westward and the central-eastern equatorial Pacific region shows an anomalously strong subsidence state. Related to the strong downwards W500, the model simulates too little CLT, PR and too high NHFS.

Regarding the ENSO characteristics, the model is highly non-linear with an about three times larger positive Niño3.4 SSTA skewness than ERA-20C. The skewness map shows the large and too westward extended positive SSTA skewness with the negative values restricted to the very western equatorial region: the location of the Pacific Warm Pool. Other ENSO simulation biases include the westward extension of the SST variability, which is overestimated over the equatorial Pacific. The model has the highest Niño3.4 SST variability during the boreal winter with the consecutive variability reduction in spring, which on the first look seems to be a correct representation of the ENSO phase locking. Nevertheless, the highest Niño3.4 SST standard deviation peaks two months delayed and a second peak related to the semiannual

ITCZ and the seasonal reversal of the winds in the east is visible during the month of July, causing an unrealistic phase locking.

The ENSO phase locking is also directly related to the atmospheric feedbacks. The dominant SST variability peaking in boreal winter coincides with a major increase of the U10 feedback, while the decrease of the SST standard deviation is linked to the increase of the negative NHFS feedback and a reduction of the U10 feedback. Comparing the tropical Pacific feedback representation of the GFDL-ESM2M model to the one of ERA-20C, both show a relatively similar pattern for the U10 feedback, while the NHFS feedback is clearly reduced in the climate model.

Along the 500 year control run the model simulates large decadal ENSO amplitude fluctuations: through the whole time series different epochs of ENSO amplitude stability and variability are observed. Two main periods of high (High epoch) and low (Low epoch) ENSO amplitudes are detected, each approximately 60 years long. The variability of the decadal ENSO amplitude is higher when comparing it to the ERA-20C reanalysis product. The High epoch is characterized by relatively large EP-like El Niño events and the Low epoch by weaker CP-like events with an increment of frequency of occurrence. Although the GFDL-ESM2M model is not able to simulate realistic ENSO spatial patterns, the highest variability is shifted from the eastern region (EP-like events) to the central-western Pacific (CP-like events) from High to Low epoch as captured by the modified TNI index.

We have also detected that the mentioned amplitude fluctuations are excited, when the background mean equatorial SST gradient is increased or decreased. In fact, the High epoch background mean state is characterized by a weaker Walker Circulation intensity with weaker convective and subsidence regimes: the zonal equatorial SST gradient is decreased by a warmer (cooler) mean SST over the eastern (western) equatorial Pacific, reducing the U10 over the central Pacific and the thermocline tilt. In addition, CLT and PR are reduced (increased) over the convective (subsidence) region. For the Low epoch, the mean state is reversed and the Walker Circulation is intensified. Moreover, the geographical pattern of the maximum and minimum values are maintained along the whole control run for all the variables, and hence, the model doesn't represent any zonal shift of the Walker Circulation.

In relation to the climate variability, the SST and zonal wind standard deviations show the largest differences between both periods over the Niño3.4 region. The largest relative variability difference between the two epochs is attributed to the W500 and PR, both located over the Niño3 region.

ENSO statistics are greatly modified too. The High epoch Niño3.4 SSTA skewness is increased to 0.48, while the Low epoch's ENSO asymmetry with 0.28 is closer to ERA-20C. However, the geographical location of maximum skewness is unrealistically shifted to the central-south equatorial Pacific. Moreover, the positive and negative SSTA's location and strength shown by the ENSO composites varies from one epoch to another and between the cold and warm ENSO events. El Niño events have strong SSTAs centered at 120°W during the High epoch, representing the EP-like events shown by the modified TNI index, while La Niña's SSTA signal is located at the central equatorial Pacific. During the Low epoch the ENSO events' signal is extended west up to 150°E and reduced on the eastern equatorial region, linked to the higher frequency of occurrence of CP-like events. Similarly, the geographical pattern of La Niñas is shifted eastward, positioned at 120°W. The phase locking of ENSO is strongly degenerated

during the Low epoch, mostly due to a weaker seasonality of the U10 feedback.

Our last attempt has been focused on understanding the possible causes for the strong decadal ENSO amplitude changes shown by the GFDL-ESM2M model. The linear U10 feedback analysis shows a strong correlation of 0.95 with the decadal ENSO amplitude evolution. Nevertheless, we have shown that the Low epoch's Niño4 zonal wind anomalies remain sensitive to Niño3.4 SSTAs. In addition, the strong negative SW feedback located over the Niño4 region represents the ability of the model to shift into a convective state when the warm El Niño events occur over the Niño3.4 area. Hence, the western equatorial Pacific wind anomalies are still affected during the Low epoch to Niño3.4 SSTAs. Regarding the negative SSTAs, the atmospheric feedbacks are greatly reduced. The zonal wind and subsidence anomalies are in fact insensitive to La Niña events.

Yet, during the Low epoch the mentioned negative feedback is hampered east of 150°W for the El Niño composites, in an area in which the mean downward winds contain the largest values. Looking into the response of vertical wind anomalies to SSTA, we have found that during the Low epoch the shift into a convection is hardly achieved over the Niño3 area, when the SSTAs are turned positive. Therefore, it is concluded that the too strong mean subsidence state of the Low epoch restricts the convection process over the Niño3.4 region and therefore, the ENSO amplitude shows low values. In contrast, a less intense Walker Circulation and subsidence state during the High epoch allows the upward wind response over the Niño3.4 domain under positive SSTAs, kicking the strong non-linear U10 feedback and enhancing the SST variability. Our findings suggest that the mean state could enhance (restrict) the ENSO amplitude during the High (Low) epoch, when the non-linear feedbacks are considered.

Our hypothesis is in fact reinforced when studying the thermocline slope-ENSO amplitude relation. Due to the strong east equatorial Pacific cold SST bias, the thermocline remains too tilted, the easterlies are too strong over the western section, and the central-eastern region is in a strong subsidence state. Although a steeper thermocline tilt could enhance the ocean-atmospheric coupling and hence increase the ENSO amplitude, if the mean tilt is exaggerated, an increase of the slope acts to reduce the SST variability as demonstrated by *Hu et al.* (2013). The GFDL-ESM2M model shows the mentioned pattern exactly: while the mean thermocline slope is increased, the decadal ENSO amplitude is linearly reduced.

4.2 Discussion

Past ENSO events have already caused large ecological, societal and economical impacts worldwide: for instance, the 1997-1998 El Niño event, also called “the climate event of the century”, caused billions of dollars in damage and thousands of lost lives (*Kerr, 1999; Mcphaden, 1999*). Ever since, possible ENSO intensity and frequency changes have gained relevant attention. As stated in the studies that used proxy data, it is believed that ENSO variability has suffered large changes throughout the Holocene (*Tudhope et al., 2001; Koutavas et al., 2006; Cobb et al., 2013; McGregor et al., 2013*).

The GFDL-ESM2M coupled GCM has been evolved directly from the previously analyzed GFDL-CM2.1 model (*Delworth et al., 2006; Wittenberg et al., 2006*). Our findings that the 500 year pre-industrial control run exhibits large, unforced, multi-decadal ENSO variability agree with previous studies (*Wittenberg, 2009; Kug et al., 2010; Wittenberg, 2015*).

Although the ENSO spatial representation shows dissimilarities in comparison to realistic EP and CP El Niño events, having the SSTAs shifted westwards, the model is still able to represent epochs of higher EP-like or CP-like El Niño frequencies. The division of the ENSO flavors has been determined with the modified TNI index, which might be polemical: although some ENSO events are known to be located clearly on the eastern or western equatorial Pacific, the large diversity of ENSO includes events that might occur in between the two defined boxes (*Capotondi et al.*, 2015; *Timmermann et al.*, 2018). Nevertheless, we proceeded with the same analysis, defining different eastern and western regions for the TNI computation, and the result remains qualitatively insensitive. Furthermore, our findings also agree with past studies (*Kug et al.*, 2010).

Besides the bias on the spatial variability of ENSO, we have seen that the studied model presents other ENSO biases like an excessive amplitude, asymmetry and delayed phase locking, which have been confirmed by previous studies (*Wittenberg et al.*, 2006; *Takahashi and Dewitte*, 2016; *Atwood et al.*, 2017). The source of the ENSO bias is believed to be, at least to some extent, the unrealistic representation of the tropical mean state (*Ham et al.*, 2013; *Wengel et al.*, 2017; *Bayr et al.*, 2018). In our case we have observed a cold equatorial bias with a maximum in the eastern section, which causes an increase of the SST gradient and anomalous easterly winds over the western equatorial Pacific in comparison to the ERA-20C reanalysis product. The consequence is a La Niña-like state, and an anomalous Walker Circulation: the rising branch is located too far west and the anomalously strong subsidence extends up to 180° , with a maximum located east of 150°W . In addition, the anomalous location of the Walker Circulation is responsible for the unrealistic atmospheric feedbacks (*Bayr et al.*, 2018). The main positive and negative feedbacks, the U10 and NHFS feedbacks respectively, are believed to have a direct influence on the unrealistic ENSO dynamics (*Bayr et al.*, 2019). It might be that the excessive ENSO variance simulated by the present climate model is affected by the too weak NHFS feedback.

Nevertheless, comparing the GFDL-ESM2M with the rest of the CMIP5 ensemble, in which the mentioned biases are commonly known, the ENSO representation and dynamics are generally improved (*Kim and Jin*, 2011; *Bellenger et al.*, 2014; *Kim et al.*, 2014; *Capotondi et al.*, 2015). Furthermore, adapting our methodology to the model biases, we can still gain understanding of the complex ocean-atmosphere interactions, which is difficult to achieve with observations. For instance, *Stevenson et al.* (2010) argued that 240 years of observations are required to measure the ENSO variability with 90% of confidence. Since our observational data sets are far shorter (*Wittenberg*, 2009), one could question whether the large decadal ENSO amplitude fluctuations shown by the GFDL-ESM2M along the 500 years run could actually be real or not. Hence, although our results might be a good guess for the decadal variability of ENSO, a combination of improvements in state-of-the-art coupled climate model biases as well as the continuation of observational data records is indispensable.

Returning to the close relation that exists between the tropical Pacific mean state and the ENSO characteristics, the epochs of different ENSO amplitudes generate changes in the mean state as demonstrated by *Ogata et al.* (2013): the epoch of high ENSO amplitude warms the eastern equatorial Pacific and cools the western region. Agreeing with our findings, the intensity and geographical location variability of the SSTAs, when El Niño and La Niña events occur during the High and Low epoch, leaves a residual that could modify the tropical Pacific mean SST. For example, during the High epoch the strong EP-like El Niño events could warm the

eastern equatorial region, while the negative SSTAs related to La Niña events cool the western region. In contrast, during the Low epoch the western equatorial positive SSTA referred to as CP-like El Niño events could produce the warming of the western equatorial section, while the negative SSTA centered at 120°W cools the eastern side. However, the differences in ENSO asymmetry as well as in the ENSO frequency of occurrence within the both studied epochs could affect the hypothesized warming and cooling of the mean state equatorial regions.

In return, the ENSO sensitivity to background mean state changes has been widely explored in the past by using intermediate complexity models (*Zebiak and Cane, 1987; Battisti and Hirst, 1989; Dewitte, 2000; Wittenberg, 2002; Roberts et al., 2014*). The influence of the mean state on the ENSO amplitude has been observed in the past years as well. The ENSO amplitude and its geographical location changes have been related to the different background mean states during the time period of 1970-2011 (*Hu et al., 2013, 2017*). As observed by *Hu et al. (2013)*, the thermocline slope increase was accompanied by the intensification of the mean easterly winds and the stronger convection (subsidence) over the western (central-eastern) equatorial Pacific. Their sensitivity experiments proved that an either too large or too small thermocline tilt causes a reduction in the ENSO amplitude. Therefore, the weakening of the tropical Pacific interannual variability since the year 2000 was suggested to be caused by the intensification of the Walker Circulation and a too strong easterly winds in a background mean state that contained a too tilted thermocline.

In our case, because the relation between the decadal mean thermocline tilt and the decadal ENSO amplitude is strictly negative, we could argue that the thermocline slope is too large to produce larger ENSO amplitudes by an increase of the mean easterly winds. In fact, the coldest mean SST bias located at the eastern equatorial Pacific and a constant La Niña-like state suggest that the thermocline tilt must be anomalously large.

In the same line, *Xiang et al. (2013)* argued that strong subsidence over the central Pacific prevents the eastward propagation of SSTAs, increasing the occurrence of the weaker CP El Niño events. This coincides with the description of the Low epoch. From the analysis of the GFDL-ESM2M pre-industrial output we could speculate that the too strong subsidence state over the Niño3 area prevents the seasonal southward migration of the ITCZ during the Low epoch, reducing the SSTAs. This could explain the reduction of Niño3.4 SST variability during the boreal winter and the reduction of the convective response to positive SSTAs, decreasing the decadal ENSO amplitude. In addition, the strong mean subsidence suggests a saturation in the downward branch of the Walker Circulation, leading to very weak La Niña related atmospheric feedbacks (*Lloyd et al., 2012*). Nevertheless, we must be careful with the idealized W500 response to local SSTAs. In fact, the source for the reduction of the convective response could also be affected by remote extratropical SST changes as stated in *Lloyd et al. (2012)* and it requires further examination.

Still, the causes for the mean state and the ENSO amplitude changes remain controversial. *Ogata et al. (2013)* proved that the warming of the eastern equatorial Pacific caused by intense ENSO activity, as seen during the High epoch, sharpens the thermocline increasing the thermocline feedback and forming a positive feedback by supporting the growth of the ENSO activity. In contrast, *Atwood et al. (2017)* showed that the less energetic Walker Circulation hampers the ENSO amplitude by stabilizing the coupled system, resulting in a negative feedback between the ENSO amplitude and the mean state atmospheric circulation intensity. Nevertheless, in their stability analysis the non-linearities were totally excluded, which we find

to be very relevant in the highly non-linear GFDL-ESM2M model. For example, the linear feedback analysis shows that the Low epoch's U10 feedback is greatly reduced. Nevertheless, considering the non-linearities between the SSTA and the U10A we observe that the sensitivity to positive Niño3.4 SSTA is not as small as shown by the linear analysis. Thus further model experiments and sensitivity test are needed in order to clarify the influences of the mean state into the ENSO activity and variability.

To end the discussion, we would like to switch our attention to the ERA-20C reanalysis product. Although the mentioned data set assimilates the strictly filtered observations and reproduces realistic ENSO events, we have found a major error in one of the most relevant atmospheric feedbacks. In fact, the SW feedback, which according to *Bellenger et al. (2014)* has a positive sign for negative SSTAs and a negative sign for positive SSTAs, behaves as a negative feedback regardless of the positive or negative SSTAs. The SW feedback has been categorized as the main ENSO error source within the coupled climate models, speculating that the problem is formed in the atmospheric compartment (*Kim and Jin, 2011*). It might be that the SW feedback error of ERA-20C has a source in the atmospheric general circulation model incorporated on its forecast system (see the Data section for further information). However, the reasons for unrealistic SW feedback representation of the reanalysis product are out of the scope of the present study.

4.3 Conclusion

The pre-industrial control simulation of the fully coupled GFDL-ESM2M climate model exhibits overall realistic ENSO representation and dynamics when comparing to the CMIP5 ensemble. Nevertheless, commonly known model biases still persist: e.g. the equatorial mean state cold bias, which is accentuated on the eastern section and the unrealistic Walker Circulation. The rising branch is located far too west and the anomalously strong subsidence regime extends up to the date line, showing the maximum downward winds over the strongest cold SST bias. The ENSO biases express too large asymmetry, two months delayed phase locking with an anomalous second SST variability peak during boreal summer, and an unrealistic geographical pattern with a westward extension of El Niño and La Niña events.

The unforced simulation is capable of simulating strong decadal ENSO amplitude fluctuations that are linked to the background mean state. Two main periods of high and low ENSO amplitudes are detected. The High epoch represents a less intense Walker Circulation with the corresponding weakening of the subsidence regime over the Niño3 domain. The negative SW feedback during El Niño events in Niño3 suggests the strong convective response of the atmospheric regime, when the SSTA are turned positive. The SST variability is considerably increased during boreal winter, and the strong non-linearities in atmospheric feedbacks are kicked forming strong EP-like El Niño events. Therefore, the ENSO asymmetry is remarkably incremented. The Low epoch, on the other hand, shows an intensive Walker Circulation. The stronger subsidence regime over the Niño3 region coincides with the reduction of the negative SW feedback for the El Niño composite, which is due to the incapability of the model to turn into a convective state, when the SSTA are turned positive. In addition, the Niño3.4 SST variability and U10 feedback are greatly reduced during boreal winter. Therefore, evidence that the seasonal southward migration of the ITCZ might be restricted by a strong subsidence state is found, hampering the evolution of strong EP-like El Niño events. Nevertheless, the

convective response is maintained over the western equatorial region as shown by the strong negative SW feedback. Hence, the decrease of Niño3.4 SSTA is accompanied by the increase of CP-like El Niño events frequency, by the reduction of the non-linearities between both phases of ENSO and by the reduction of ENSO asymmetry.

List of Figures

1.1	Schematic representation of the tropical Pacific's oceanic and atmospheric mean states. Red and blue shading correspond to warm and cold SSTs, respectively. The Walker Circulation is represented by the black dashed line, the direction pointed out by the black arrows. The white arrows show the equatorial easterly winds, the blue arrow the upwelling system and the solid red line the depth of the thermocline. Source: <i>Collins et al.</i> (2010)	4
1.2	El Niño and La Niña conditions: during an El Niño (La Niña) event the thermocline is flattened (tilted), deepening (shoaling) in the east equatorial Pacific, warming (cooling) the central-eastern regions, displacing the upper branch of the Walker Circulation eastward (westward) and weakening (strengthening) the trade winds. Source: <i>National Oceanic and Atmospheric Administration</i> (2019)	5
1.3	Spatial pattern of the sea surface temperature anomalies (SSTA) for specific warm and cold events: a) East Pacific (EP) El Niño event during 1997-1998, b) East Pacific (EP) La Niña event during 2007-2008, c) Central Pacific (CP) El Niño event during 2004-2005 and d) Central Pacific (CP) La Niña event during 1988-1989. Source: <i>Capotondi et al.</i> (2015)	6
1.4	Niño index regions: Niño1+2 in red (90°W - 80°W, 0°- 10°S), Niño3 in blue (150°W - 90°W, 5°N - 5°S), Niño3.4 (170°W - 120°W, 5°N - 5°S) dotted and Niño4 (160°E - 150°W, 5°N - 5°S) in green. Source: <i>Trenberth</i> (2019)	6
3.1	The mean sea surface temperature (SST) relative to the area mean tropical Pacific SST for: a) ERA-20C, and b) GFDL-ESM2M.	19
3.2	Mean state model bias for a) the sea surface temperature (SST), and b) the surface zonal winds (U10), obtained by the difference between the GFDL-ESM2M model and the ERA-20C reanalysis product.	19
3.3	Equatorial Pacific mean state (5°N-5°S) of a) sea surface temperature (SST), b) surface zonal winds (U10), c) vertical wind at 500 hPa height (W500), d) net heat flux (NHFS), e) total cloud cover (CLT) and f) precipitation (PR). GFDL-ESM2M in red and ERA-20C in blue.	20
3.4	Probability density function of Niño3.4 sea surface temperature anomalies (SSTA). The skewness value, representing the ENSO asymmetry, is displayed in the upper left corner of the plots: a) ERA-20C, and b) GFDL-ESM2M. . . .	21

3.5	Skewness map of tropical Pacific sea surface temperature anomalies (SSTA) for a) ERA-20C, and b) GFDL-ESM2M.	21
3.6	Skewness map of tropical Pacific surface zonal wind anomalies (U10A) for a) ERA-20C, and b) GFDL-ESM2M.	22
3.7	Monthly standard deviation of the sea surface temperatures (SST) over: a) the Niño3.4 region, ERA-20C in blue and GFDL-ESM2M model in red, b) the Pacific equatorial (5°N-5°S) region for ERA-20C, and c) the same as b) but for GFDL-ESM2M.	23
3.8	Geographical location of ERA-20C reanalysis product tropical Pacific sea surface temperature anomalies (SSTA) from a) El Niño composite, b) La Niña composite, and c) their residual obtained by adding both composites. Similarly, d) e) and f) correspond to the GFDL-ESM2M model.	23
3.9	Linear wind (U10) feedback: anomalous surface zonal wind (U10A) sensitivity to Niño3.4 sea surface temperature anomalies (SSTA) for each tropical Pacific grid point for a) ERA-20C, and b) GFDL-ESM2M.	24
3.10	Linear net heat flux (NHFS) feedback: anomalous net heat flux (NHFS) sensitivity to Niño3.4 sea surface temperature anomalies (SSTA) for each tropical Pacific grid point for a) ERA-20C, and b) GFDL-ESM2M	25
3.11	Monthly wind (U10) feedback in red and net heat flux (NHFS) feedback in solid blue. The net heat flux feedback has been divided into latent heat flux (LHFS) shown as dashed blue and shortwave radiation (SW) as dash-dot blue. Niño3.4 sea surface temperature anomalies (SSTA) have been linearly related to Niño4 surface zonal wind anomalies, and with the combination of Niño3 and Niño4 for the net heat flux anomalies, as well as for its components.	25
3.12	Monthly climatology of Niño3.4 sea surface temperature (SST) in GFDL-ESM2M. The error bars show the 95% confidence interval of the 30 year running mean windows.	27
3.13	Comparison between a) 30 year running window of Niño3.4 sea surface temperatures (SST) and b) 30 year low-passed Niño3.4 sea surface temperature anomalies (SSTA) relative to a constant climatology. c) and d) are similar to a) and b), but in this case we compare the mean values of the eastern (130°W - 90°W, 5°N - 5°S) and western box (170°E - 140°W, 5°N - 5°S) to the modified and low-passed Trans-Niño Index (TNI) relative to a constant climatology.	28
3.14	The ENSO amplitude computed with a 30 year running standard deviation of Niño3.4 sea surface temperatures (SST) for a) ERA-20c, and b) GFLD-ESM2M.	29
3.15	Classification of the ENSO events into Central Pacific (CP) and East Pacific (EP) types within 30 year bins. a) El Niño events with a threshold of half a sea surface temperature anomaly (SSTA) standard deviation over the Niño3.4 region, b) La Niña events with a threshold of half a sea surface temperature anomaly (SSTA) standard deviation over the Niño3.4 region. c) and d) are similar to a) and b), but they only consider strong ENSO events exceeding a double standard deviation.	30

3.16	Hovmöller diagram of equatorial (5°N - 5°S) sea surface temperature anomaly (SSTA) composites, setting the zero value to December and negative and positive values to the previous or consequent months, respectively, for a) El Niño composite and b) La Niña composite.	31
3.17	Representation of the tropical Pacific mean state during the High and Low epochs as well as their difference: a) High epoch sea surface temperature (SST) relative to the tropical Pacific SST, b) same as a) but for the Low epoch, c) the difference of relative sea surface temperature (SST) between the High and the Low epoch. Following the same structure, d), e), f) correspond to subsurface temperatures (T), g), h), i) to surface zonal winds (U10), j), k), l) to vertical winds at 500 hPa (W500), m), n), o) to the net heat flux (NHFS), p), q), r) to the precipitation (PR) and s), t), u) to the total cloud cover (CLT).	34
3.18	Equatorial Pacific mean state (5°N - 5°S) for: a) sea surface temperatures (SST), b) surface zonal winds (U10), c) vertical wind at 500 hPa height (W500), d) net heat flux (NHFS), e) total cloud cover (CLT) and f) precipitation (PR). GFDL-ESM2M's High epoch in red and the Low epoch in blue. The black line represents ERA-20C output.	35
3.19	Representation of the tropical Pacific variability computed with the standard deviation during the High and Low ENSO amplitude periods as well as their difference: a) High epoch sea surface temperature (SST), b) same as a) but for the Low epoch, c) the variability ratio between the High and the Low epoch. Following the same structure, d), e), f) correspond to the subsurface temperatures (T) with the solid lines representing the thermocline depth variability in meters, g), h), i) to surface zonal winds (U10), j), k), l) to vertical winds at 500 hPa height (W500), m), n), o) to the net heat flux (NHFS), p), q), r) to the precipitation (PR) and s), t), u) to the total cloud cover (CLT).	37
3.20	Probability density function of Niño3.4 sea surface temperature anomalies. The skewness value, representing the ENSO asymmetry is displayed on the upper left corner of the plots for a) the High epoch, and b) the Low epoch	38
3.21	Skewness map of tropical Pacific sea surface temperature anomalies (SSTA) for a) the High epoch, and b) the Low epoch.	39
3.22	Skewness map of tropical Pacific surface zonal wind anomalies (U10A) for a) the High epoch, and b) the Low epoch.	39
3.23	Monthly standard deviation of the sea surface temperatures (SST) over: a) the Niño3.4 region, the High epoch in red and the Low epoch in blue, b) the Pacific equatorial (5°N - 5°S) region for the High epoch, and c) the same as b) but for the Low epoch.	40
3.24	Hovmöller diagram of equatorial (5°N - 5°S) sea surface temperature anomaly (SSTA) composites setting the zero value to December and negative and positive values to the previous or consequent months, respectively, for a) the El Niño composite during the High epoch, b) the El Niño composite during the Low epoch, c) the La Niña composite during the High epoch, d) the La Niña composite during the Low epoch.	41

- 3.25 Geographical location of the tropical Pacific sea surface temperature anomalies (SSTA) for the High epoch, the Low epoch, as well as their difference: a) the El Niño composite during the High epoch, b) the La Niña composite during the High epoch, and c) their residual obtained by adding both composites. Similarly, d), e), and f) correspond to the Low epoch and g), h), and i) to the difference between the two epochs. 42
- 3.26 Monthly atmospheric feedbacks for the High epoch in red and the Low epoch in blue. The Niño 3.4 sea surface temperature anomalies (SSTA) have been linearly related to a) the net heat flux anomalies (NHFSa) over the Niño3 and Niño4 regions, b) latent heat flux anomalies (LHFSA) over the Niño3 and Niño4 regions, c) shortwave radiation anomalies (SWA) over the Niño3 and Niño4 regions, and d) surface zonal wind anomalies (U10A) over the Niño4 region. 43
- 3.27 Linear correlation between the low-passed wind (U10) feedback and the ENSO amplitude for a) ERA-20C, and b) GFDL-ESM2M. The correlation coefficients are displayed on the upper left corner of the figures. 44
- 3.28 Linear correlation between the wind (U10) feedback and a) the low-passed mean Niño3 sea surface temperature (SST) relative to the tropical Pacific, and b) the low-passed mean Niño4 sea surface temperature (SST) relative to the tropical Pacific. The correlation coefficients are displayed on the upper left corner of the figures. 45
- 3.29 Non-linear relationship between the Niño3.4 sea surface temperature anomalies (SSTA) and the surface zonal wind anomalies (U10A) over Niño4. The solid lines represent the slope of the linear relation when positive and negative SSTA are divided without their corresponding offsets. Each dot represents individual months. a) ERA-20C reanalysis product, b) same as a) but for the GFDL-ESM2M model, and c) same as b) but dividing the High and Low epochs in red and blue, respectively. 46
- 3.30 Tropical Pacific representation of the shortwave radiation (SW) feedback computed as the linear regression between the Niño3.4 sea surface temperature anomalies (SSTA) and the shortwave radiation anomalies (SWA) for each spatial grid point for a) the El Niño composite for the whole time series, b) the La Niña composite for the whole time series, c) same as a) but for the High epoch, d) same as b) but for the High epoch, e) same as a) but for the Low epoch, and f) same as b) but for the Low epoch. 47
- 3.31 Non-linear relationship between the Niño3.4 sea surface temperature anomalies (SSTA) and the shortwave radiation anomalies (SWA). The solid lines represent the slope of the linear relation, when positive and negative SSTA are divided without their corresponding offsets. Each dot represents individual months. a) ERA-20C reanalysis product using the Niño3 box for SWA, b) same as a) but for the GFDL-ESM2M model using the box set to 180°- 120°W, 5°N - 5 °S for SWA, and c) same as b) but dividing the High and Low epochs in red and blue, respectively. 48

- 3.32 Non-linear relationship between the Niño3.4 sea surface temperature anomalies (SSTA) and the vertical wind anomalies at 500 hPa height (W500A) over Niño3. The solid lines represent the slope of the linear relation, when positive and negative SSTA are divided without their corresponding offsets. Each dot represents individual months. a) ERA-20C reanalysis product, b) same as a) but for the GFDL-ESM2M model, and c) same as b) but dividing the High and Low epochs in red and blue, respectively. 49
- 3.33 Relation between the decadal ENSO amplitude, computed as a 30 year running sea surface temperature (SST) standard deviation, and the 30 year low-passed thermocline slope calculated as the thermocline depth difference between the eastern (120°W - 90°W, 5°N - 5 °S) and western (160°E - 170°W, 5°N - 5 °S) equatorial Pacific. The thermocline depth is detected as the depth of strongest vertical temperature gradient. Each dot represents a 30 year window value. . . . 50

Bibliography

- Alexander, M. A., I. Bladé, M. Newman, J. R. Lanzante, N. C. Lau, and J. D. Scott (2002), The atmospheric bridge: The influence of ENSO teleconnections on air-sea interaction over the global oceans, *Journal of Climate*, *15*(16), 2205–2231, doi:10.1175/1520-0442(2002)015<2205:TABTIO>2.0.CO;2.
- An, S. I., and B. Wang (2000), Interdecadal change of the structure of the ENSO mode and its impact on the ENSO frequency, *Journal of Climate*, *13*(12), 2044–2055, doi:10.1175/1520-0442(2000)013<2044:ICOTSO>2.0.CO;2.
- Ashok, K., S. K. Behera, S. A. Rao, H. Weng, and T. Yamagata (2007), El Niño Modoki and its possible teleconnection, *Journal of Geophysical Research: Oceans*, *112*(11), doi:10.1029/2006JC003798.
- Atwood, A. R., D. S. Battisti, A. T. Wittenberg, W. H. Roberts, and D. J. Vimont (2017), Characterizing unforced multi-decadal variability of ENSO: a case study with the GFDL CM2.1 coupled GCM, *Climate Dynamics*, *49*(7-8), 2845–2862, doi:10.1007/s00382-016-3477-9.
- Bamston, A. G., M. Chelliah, and S. B. Goldenberg (1997), Documentation of a highly ENSO-related SST region in the equatorial Pacific: Research note, *Atmosphere - Ocean*, *35*(3), 367–383, doi:10.1080/07055900.1997.9649597.
- Battisti, D. S., and A. C. Hirst (1989), Interannual variability in a tropical atmosphere-ocean model: influence of the basic state, ocean geometry and non-linearity, *Journal of the Atmospheric Sciences*, *46*(12), 1687–1712, doi:10.1175/1520-0469(1989)046<1687:IVIATA>2.0.CO;2.
- Bayr, T., and D. Dommenges (2013), The tropospheric Land-Sea warming contrast as the driver of tropical sea level pressure changes, doi:10.1175/JCLI-D-14-00592.1.
- Bayr, T., M. Latif, D. Dommenges, C. Wengel, J. Harlaß, and W. Park (2018), Mean-state dependence of ENSO atmospheric feedbacks in climate models, *Climate Dynamics*, *50*(9-10), 3171–3194, doi:10.1007/s00382-017-3799-2.
- Bayr, T., C. Wengel, M. Latif, D. Dommenges, J. Lübbecke, and W. Park (2019), Error compensation of ENSO atmospheric feedbacks in climate models and its influence on simulated ENSO dynamics, *Climate Dynamics*, *53*(1-2), 155–172, doi:10.1007/s00382-018-4575-7.
- Bellenger, H., E. Guilyardi, J. Leloup, M. Lengaigne, and J. Vialard (2014), ENSO representation in climate models: From CMIP3 to CMIP5, *Climate Dynamics*, *42*(7-8), 1999–2018, doi:10.1007/s00382-013-1783-z.

- Bjerknes, J. (1966), A possible response of the atmospheric Hadley circulation to equatorial anomalies of ocean temperature, *Tellus*, 18(4), 820–829, doi:10.3402/tellusa.v18i4.9712.
- Bjerknes, J. (1969), Atmospheric teleconnections from the equatorial Pacific, *Monthly Weather Review*, 97(3), 163–172, doi:10.1175/1520-0493(1969)097<0163:atftpe>2.3.co;2.
- Burgers, G., and D. B. Stephenson (1999), The "normality" of El Niño, *Geophysical Research Letters*, 26(8), 1027–1030, doi:10.1029/1999GL900161.
- Byrne, M. P., A. G. Pendergrass, A. D. Rapp, and K. R. Wodzicki (2018), Response of the intertropical convergence zone to climate change: location, width, and strength, doi:10.1007/s40641-018-0110-5.
- Capotondi, A., et al. (2015), Understanding ENSO diversity, *Bulletin of the American Meteorological Society*, 96(6), 921–938, doi:10.1175/BAMS-D-13-00117.1.
- Chen, C., M. A. Cane, A. T. Wittenberg, and D. Chen (2017), ENSO in the CMIP5 simulations: life cycles, diversity, and responses to climate change, *Journal of Climate*, 30(2), 775–801, doi:10.1175/jcli-d-15-0901.1.
- Cobb, K. M., N. Westphal, H. R. Sayani, J. T. Watson, E. Di Lorenzo, H. Cheng, R. L. Edwards, and C. D. Charles (2013), Highly variable El Niño–Southern Oscillation throughout the Holocene, *Science*, 339(6115), 67–70, doi:10.1126/science.1228246.
- Cole, J. (2001), A slow dance for El Niño, doi:10.1126/science.1059111.
- Collins, M., et al. (2010), The impact of global warming on the tropical Pacific Ocean and El Niño.
- Davey, M., et al. (2002), STOIC: A study of coupled model climatology and variability in tropical ocean regions, *Climate Dynamics*, 18(5), 403–420, doi:10.1007/s00382-001-0188-6.
- Delworth, T. L., et al. (2006), GFDL’s CM2 global coupled climate models. Part I: Formulation and simulation characteristics, *Journal of Climate*, 19(5), 643–674, doi:10.1175/JCLI3629.1.
- Dewitte, B. (2000), Sensitivity of an intermediate ocean-atmosphere coupled model of the tropical Pacific to its oceanic vertical structure, *Journal of Climate*, 13(13), 2363–2388, doi:10.1175/1520-0442(2000)013<2363:SOAIOA>2.0.CO;2.
- Diaz, H. F., and V. Markgraf (2000), El Niño and the Southern Oscillation. Multiscale Variability and Global and Regional Impacts, *Cambridge University Press*, p. 556, doi:10.1177/088506668700200407.
- Dommenget, D., and Y. Yu (2016), The seasonally changing cloud feedbacks contribution to the ENSO seasonal phase-locking, *Climate Dynamics*, 47(12), 3661–3672, doi:10.1007/s00382-016-3034-6.
- Dommenget, D., S. Haase, T. Bayr, and C. Frauen (2014), Analysis of the Slab Ocean El Niño atmospheric feedbacks in observed and simulated ENSO dynamics, *Climate Dynamics*, 42(11–12), 3187–3205, doi:10.1007/s00382-014-2057-0.

- Dunne, J. P., et al. (2012), GFDL’s ESM2 global coupled climate-carbon earth system models. Part I: Physical formulation and baseline simulation characteristics, *Journal of Climate*, 25(19), 6646–6665, doi:10.1175/JCLI-D-11-00560.1.
- Dunne, J. P., et al. (2013), GFDL’s ESM2 Global Coupled Climate–Carbon Earth System Models. Part II: Carbon System Formulation and Baseline Simulation Characteristics*, *Journal of Climate*, 26(7), 2247–2267, doi:10.1175/JCLI.
- European Network for Earth System Modelling, E. (2019), Experiments, ensembles, variable names, and other properties.
- Fedorov, A. V., and S. G. Philander (2000), Is El Niño changing?, doi:10.1126/science.288.5473.1997.
- Ham, Y. G., J. S. Kug, D. Kim, Y. H. Kim, and D. H. Kim (2013), What controls phase-locking of ENSO to boreal winter in coupled GCMs?, *Climate Dynamics*, 40(5-6), 1551–1568, doi:10.1007/s00382-012-1420-2.
- Handmer, J. W., S. Dovers, and T. E. Downing (1999), Societal vulnerability to climate change and variability, *Mitigation and Adaptation Strategies for Global Change*, 4(3-4), 267–281.
- Hanley, D. E., M. A. Bourassa, J. J. O’Brien, S. R. Smith, and E. R. Spade (2003), A quantitative evaluation of ENSO indices, *Journal of Climate*, 16(8), 1249–1258, doi:10.1175/1520-0442(2003)16<1249:AQEOEI>2.0.CO;2.
- Harrison, D. E., and G. A. Vecchi (1999), On the termination of El Niño, *Geophysical Research Letters*, 26(11), 1593–1596, doi:10.1029/1999GL900316.
- Heavens, N. G., and N. M. Mahowald (2013), Studying and Projecting Climate Change with Earth System Models, *Nature Education Knowledge*, 4(5), 4.
- Hersbach, H., C. Peubey, A. Simmons, and P. Poli (2013), ERA-20CM: a twentieth century atmospheric model ensemble, *Tech. rep.*
- Hsu, H. H., and A. D. Moura (2001), Workshop on the impacts of the 1997-99 ENSO, in *Bulletin of the American Meteorological Society*, vol. 82, pp. 305–312, American Meteorological Society.
- Hu, Z. Z., A. Kumar, H. L. Ren, H. Wang, M. L’heureux, and F. F. Jin (2013), Weakened interannual variability in the tropical pacific ocean since 2000, *Journal of Climate*, 26(8), 2601–2613, doi:10.1175/JCLI-D-12-00265.1.
- Hu, Z. Z., A. Kumar, B. Huang, J. Zhu, and H. L. Ren (2017), Interdecadal variations of ENSO around 1999/2000, *Journal of Meteorological Research*, 31(1), 73–81, doi:10.1007/s13351-017-6074-x.
- Jin, F. F. (1996), Tropical ocean-atmosphere interaction, the pacific cold tongue, and the El Niño-Southern Oscillation, *Science*, 274(5284), 76–78, doi:10.1126/science.274.5284.76.
- Jin, F. F., S. T. Kim, and L. Bejarano (2006), A coupled-stability index for ENSO, *Geophysical Research Letters*, 33(23), doi:10.1029/2006GL027221.

- Kerr, R. A. (1999), Big El Niños ride the back of slower climate change, doi:10.1126/science.283.5405.1108.
- Kessler, W. S., L. M. Rothstein, and D. Chen (1998), The annual cycle of SST in the eastern tropical Pacific, diagnosed in an ocean GCM, *Journal of Climate*, 11(5), 777–799, doi:10.1175/1520-0442(1998)011<0777:TACOSI>2.0.CO;2.
- Kim, S. T., and F. F. Jin (2011), An ENSO stability analysis. Part II: Results from the twentieth and twenty-first century simulations of the CMIP3 models, *Climate Dynamics*, 36(7), 1609–1627, doi:10.1007/s00382-010-0872-5.
- Kim, S. T., and J. Y. Yu (2012), The two types of ENSO in CMIP5 models, *Geophysical Research Letters*, 39(11), doi:10.1029/2012GL052006.
- Kim, S. T., W. Cai, F. F. Jin, and J. Y. Yu (2014), ENSO stability in coupled climate models and its association with mean state, *Climate Dynamics*, 42(11-12), 3313–3321, doi:10.1007/s00382-013-1833-6.
- Knutson, T. R., S. Manabe, and D. Gu (1997), Simulated ENSO in a global coupled ocean-atmosphere model: Multidecadal amplitude modulation and CO₂ sensitivity, *Journal of Climate*, 10(1), 138–161, doi:10.1175/1520-0442(1997)010<0138:SEIAGC>2.0.CO;2.
- Koutavas, A., P. B. DeMenocal, G. C. Olive, and J. Lynch-Stieglitz (2006), Mid-Holocene El Niño-Southern Oscillation (ENSO) attenuation revealed by individual foraminifera in eastern tropical Pacific sediments, *Geology*, 34(12), 993–996, doi:10.1130/G22810A.1.
- Kug, J. S., J. Choi, S. I. An, F. F. Jin, and A. T. Wittenberg (2010), Warm pool and cold tongue El Niño events as simulated by the GFDL 2.1 coupled GCM, *Journal of Climate*, 23(5), 1226–1239, doi:10.1175/2009JCLI3293.1.
- Larkin, N. K., and D. E. Harrison (2005), Global seasonal temperature and precipitation anomalies during El Niño autumn and winter, *Geophysical Research Letters*, 32(16), 1–4, doi:10.1029/2005GL022860.
- Latif, M., A. Sterl, E. Maier-Reimer, and M. M. Junge (1993), Climate variability in a coupled GCM. Part I: the tropical Pacific, *Journal of Climate*, 6(1), 5–21, doi:10.1175/1520-0442(1993)006<0005:cviacg>2.0.co;2.
- Lau K.; Yang S. (2002), Walker circulation, in *Encyclopedia of Atmospheric Sciences*, pp. 1–6, doi:10.1006/rwas.2002.0450.
- Li, G., B. H. Ren, C. Y. Yang, and J. Q. Zheng (2010), Indices of El Niño and El Niño Modoki: An improved El Niño Modoki index, *Advances in Atmospheric Sciences*, 27(5), 1210–1220, doi:10.1007/s00376-010-9173-5.
- Lin, J. L. (2007), The double-ITCZ problem in IPCC AR4 coupled GCMs: Ocean-atmosphere feedback analysis, *Journal of Climate*, 20(18), 4497–4525, doi:10.1175/JCLI4272.1.
- Lloyd, J., E. Guilyardi, H. Weller, and J. Slingo (2009), The role of atmosphere feedbacks during ENSO in the CMIP3 models, *Atmospheric Science Letters*, 10(3), 170–176, doi:10.1002/asl.227.

- Lloyd, J., E. Guilyardi, and H. Weller (2012), The role of atmosphere feedbacks during ENSO in the CMIP3 models. Part III: The shortwave flux feedback, *Journal of Climate*, *25*(12), 4275–4293, doi:10.1175/JCLI-D-11-00178.1.
- Masters, W. A., and M. S. McMillan (2001), Climate and scale in economic growth, *Journal of Economic Growth*, *6*(3), 167–186, doi:10.1023/A:1011398431524.
- McGregor, H. V., M. J. Fischer, M. K. Gagan, D. Fink, S. J. Phipps, H. Wong, and C. D. Woodroffe (2013), A weak El Niño/Southern Oscillation with delayed seasonal growth around 4,300 years ago, *Nature Geoscience*, *6*(11), 949–953, doi:10.1038/ngeo1936.
- McPhaden, M. J. (1999), The Child Prodigy of 1997-98, *Nature*, *398*(6728), 559.
- McPhaden, M. J., S. E. Zebiak, and M. H. Glantz (2006), ENSO as an integrating concept in earth science, doi:10.1126/science.1132588.
- McPhaden, M. J., T. Lee, and D. McClurg (2011), El Niño and its relationship to changing background conditions in the tropical Pacific Ocean, *Geophysical Research Letters*, *38*(15), doi:10.1029/2011GL048275.
- National Oceanic and Atmospheric Administration, N. (2018), What are the trade winds?, *National Ocean Service website*.
- National Oceanic and Atmospheric Administration, N. (2019), Explaining El Niño.
- Ogata, T., S. P. Xie, A. Wittenberg, and D. Z. Sun (2013), Interdecadal amplitude modulation of El Niño-southern oscillation and its impact on tropical Pacific decadal variability, *Journal of Climate*, *26*(18), 7280–7297, doi:10.1175/JCLI-D-12-00415.1.
- Philander, S. G., D. Gu, D. Halpern, G. Lambert, N. C. Lau, T. Li, and R. C. Pacanowski (1996), Why the ITCZ is mostly north of the equator, *Journal of Climate*, *9*(12), 2958–2972, doi:10.1175/1520-0442(1996)009<2958:WTIIMN>2.0.CO;2.
- Philander, S. G. H. (1981), The response of equatorial oceans to a relaxation of the trade winds., *J. PHYS. OCEANOGR.*, *11*(2 , Feb. 1981), 176–189.
- Philander, S. G. H. (1983), El Niño Southern Oscillation phenomena, *Nature*, *302*(5906), 295.
- Philander, S. G. H. (1985), El Niño and La Niña, *Journal of Atmospheric Sciences*, *42*(23), 2652.
- Poli, P., et al. (2016), ERA-20C: An atmospheric reanalysis of the twentieth century, *Journal of Climate*, *29*(11), 4083–4097, doi:10.1175/JCLI-D-15-0556.1.
- Quan, X.-W., H. F. Diaz, and M. P. Hoerling (2004), Change in the Tropical Hadley Cell Since 1950, in *The Hadley circulation: present, past and future*, chap. 3, pp. 85–120, Springer, Dordrecht, doi:10.1007/978-1-4020-2944-8-4.
- Rasmusson, E. M., and T. H. Carpenter (1982), Variations in tropical sea surface temperature and surface wind fields associated with the Southern Oscillation/El Niño (Pacific) ., *Monthly Weather Review*, *110*(5), 354–384, doi:10.1175/1520-0493(1982)110<0354:VITSST>2.0.CO;2.

- Reuveny, R. (2007), Climate change-induced migration and violent conflict, *Political Geography*, *26*(6), 656–673, doi:10.1016/j.polgeo.2007.05.001.
- Roberts, W. H., D. S. Battisti, and A. W. Tudhope (2014), ENSO in the mid-holocene according to CSM and hadCM3, *Journal of Climate*, *27*(3), 1223–1242, doi:10.1175/JCLI-D-13-00251.1.
- Rodgers, K. B., P. Friederichs, and M. Latif (2004), Tropical Pacific decadal variability and its relation to decadal modulations of ENSO, *Journal of Climate*, *17*(19), 3761–3774, doi:10.1175/1520-0442(2004)017<3761:TPDVAI>2.0.CO;2.
- Russon, T., A. W. Tudhope, G. C. Hegerl, A. Schurer, and M. Collins (2014), Assessing the significance of changes in ENSO amplitude using variance metrics, *Journal of Climate*, *27*(13), 4911–4922, doi:10.1175/JCLI-D-13-00077.1.
- Santoso, A., M. J. Mcphaden, and W. Cai (2017), The defining characteristics of ENSO extremes and the strong 2015/2016 El Niño, doi:10.1002/2017RG000560.
- Stevenson, S., B. Fox-Kemper, M. Jochum, B. Rajagopalan, and S. G. Yeager (2010), ENSO model validation using wavelet probability analysis, *Journal of Climate*, *23*(20), 5540–5547, doi:10.1175/2010JCLI3609.1.
- Sun, F., and J. Y. Yu (2009), A 10-15-Yr modulation cycle of ENSO intensity, *Journal of Climate*, *22*(7), 1718–1735, doi:10.1175/2008JCLI2285.1.
- Takahashi, K., and B. Dewitte (2016), Strong and moderate nonlinear El Niño regimes, *Climate Dynamics*, *46*(5-6), 1627–1645, doi:10.1007/s00382-015-2665-3.
- Timmermann, A., et al. (2018), El Niño–Southern Oscillation complexity, doi:10.1038/s41586-018-0252-6.
- Trenberth, K. (2019), The Climate Data Guide: Nino SST Indices (Nino 1+2, 3, 3.4, 4; ONI and TNI).
- Trenberth, K. E., and D. P. Stepaniak (2001), Indices of El Niño evolution, *Journal of Climate*, *14*(8), 1697–1701.
- Trenberth, K. E., G. W. Branstator, D. Karoly, A. Kumar, N.-C. Lau, and C. Ropelewski (1998), Progress during TOGA in understanding and modeling global teleconnections associated with tropical sea surface temperatures, *Journal of Geophysical Research: Oceans*, *103*(C7), 14,291–14,324, doi:10.1029/97JC01444.
- Tudhope, A. W., C. P. Chilcott, M. T. McCulloch, E. R. Cook, J. Chappell, R. M. El-lam, D. W. Lea, J. M. Lough, and G. B. Shimmield (2001), Variability in the El Niño–Southern Oscillation through a glacial-interglacial cycle, *Science*, *291*(5508), 1511–1517, doi:10.1126/science.1057969.
- Wengel, C., M. Latif, W. Park, J. Harlaß, and T. Bayr (2017), Seasonal ENSO phase locking in the Kiel Climate Model: The importance of the equatorial cold sea surface temperature bias, *Climate Dynamics*, *50*(3-4), 901–919, doi:10.1007/s00382-017-3648-3.
- Wittenberg, A. T. (2002), ENSO response to altered climates, *Ph.D. Thesis, Princeton University*, (June), 475, doi:10.13140/RG.2.1.1777.8403.

- Wittenberg, A. T. (2009), Are historical records sufficient to constrain ENSO simulations?, *Geophysical Research Letters*, *36*(12), doi:10.1029/2009GL038710.
- Wittenberg, A. T. (2015), Low-frequency variations of ENSO, *US Clivar Variations*, *13*(1), 26–31.
- Wittenberg, A. T., A. Rosati, N. C. Lau, and J. J. Ploshay (2006), GFDL’s CM2 global coupled climate models. Part III: Tropical Pacific climate and ENSO, *Journal of Climate*, *19*(5), 698–722, doi:10.1175/JCLI3631.1.
- Wyrtki, K. (1974), Equatorial currents in the Pacific 1950 to 1970 and their relations to the trade winds, *Journal of Physical Oceanography*, *4*(3), 372–380, doi:10.1175/1520-0485(1974)004<0372:ecitpt>2.0.co;2.
- Xiang, B., B. Wang, and T. Li (2013), A new paradigm for the predominance of standing Central Pacific Warming after the late 1990s, *Climate Dynamics*, *41*(2), 327–340, doi:10.1007/s00382-012-1427-8.
- Xie, S.-P. (2004), The Shape of Continents, Air-Sea Interaction, and the Rising Branch of the Hadley Circulation, in *Advances in Global Change Research*, edited by Diaz Henry F., , and R. S. Bradley, pp. 121–152, Springer Netherlands, Dordrecht, doi:10.1007/978-1-4020-2944-8-5.
- Yang, H., and F. Wang (2009), Revisiting the thermocline depth in the equatorial Pacific, *Journal of Climate*, *22*(13), 3856–3863, doi:10.1175/2009JCLI2836.1.
- Yeh, S. W., and B. P. Kirtman (2005), Pacific decadal variability and decadal ENSO amplitude modulation, *Geophysical Research Letters*, *32*(5), 1–5, doi:10.1029/2004GL021731.
- Yu, H., and M. Zhang (2018), Explaining the year-to-year variability of the eastern Pacific intertropical convergence zone in the boreal spring, *Journal of Geophysical Research: Atmospheres*, *123*(8), 3847–3856, doi:10.1002/2017JD028156.
- Zebiak, S. E., and M. A. Cane (1987), A Model El Niño–Southern Oscillation, *Monthly Weather Review*, *115*(10), 2262–2278, doi:10.1175/1520-0493(1987)115<2262:ameno>2.0.co;2.

Acknowledgement

I would like to express my most sincere appreciation to my Master Thesis supervisors, Prof. Dr. Mojib Latif and Dr. Tobias Bayr, for their guidance and support, always encouraging me to develop my own ideas and making possible the accomplishment of the present research.

I want to thank my colleagues of the Climate Physics Master degree for the excellent study and working environment generated during the last two years. Specially to Zerlina Hofmann, Michael Gloyer and Thómas Zoëga, from whom I have received a personal and academical support to achieve the Master degree.

Finally, my deepest and most sincere acknowledgment to my family for their unconditional support throughout the whole study process.

Declaration of candidate

I, Goratz Beobide Arsuaga, declare that the present thesis entitled *Decadal variability of El Niño / Southern Oscillation in the GFDL-ESM2M pre-industrial control simulation* contains no material that has been submitted in any other form somewhere else. The content presented is my own work, except where otherwise indicated. The document stored in the electronic device is the same as the one printed.

Goratz Beobide Arsuaga
Kiel, October 2019